Nuclear Modification at 17.3 GeV Nucleon-Nucleon Collision Energy, Measured by the Experiment CERN-NA49

Ph.D. dissertation

András LÁSZLÓ
KFKI Research Institute for Particle and Nuclear Physics, Budapest
laszloa@rmki.kfki.hu

November 2007

Doctorate School of Physics (Head: Dr. Zalán Horváth),
Particle Physics and Astronomy Program (Head: Dr. Ferenc Csikor),
Eötvös University, Budapest

Supervisor: Dr. György Vesztergombi

Abstract

Nucleon-nucleon interactions have been studied intensely in the last decades. With the advent of high energy measurements, boosted especially by the RHIC collider at Brookhaven, even those high transverse momentum particles became accessible, which can carry information on the quark-level of the interactions. At RHIC, in central Au+Au interactions at 200 GeV center-of-mass energy, high transverse momentum particle production proved to be reduced relative to the more elementary p+p, or d+Au, and even peripheral Au+Au interactions. It was argued that this phenomenon is a QCD-induced parton energy loss in the interacting matter. The energy dependence of this suppression is a crucial issue in understanding whether the interacting matter, probed by the parton, undergoes phase transition or exhibit sharp change as a function of the available energy. The aim of the present study is to answer this question by analyzing the 17.3 GeV nucleon-nucleon collision energy Pb+Pb data, recorded by the experiment CERN-NA49.

The main results are the transverse momentum spectra (up to 4.5 GeV/c) around midrapidity of $\pi^{\pm}$, $p, \bar{p}$, $K^{\pm}$ particles in Pb+Pb (at various centralities), p+Pb, and p+p reactions. The details of the measurement and analysis methods are discussed. An other important outcome of the work is an unfolding method for signal processing, which was developed during the π^0 spectrum analysis surveys.

The analysis shows that the amount of particle suppression does not exhibit a sudden vanishing when going down to 17.3 GeV nucleon-nucleon collision energy, however the amount of suppression is reduced.

Contents

1 Introduction **7**

1.1 QCD and its Consequences 7

1.2 Proton-Proton, Proton-Nucleus and Nucleus-Nucleus Collisions 11

1.3 High Transverse Momentum Particle Suppression 14

1.4 Experimental Possibilities at CERN-NA49 18

1.5 Thesis Objectives 19

2 Experimental Setup **23**

2.1 Overview 23

2.2 The Trigger System 25

2.3 Event Centrality Determination 26

2.4 Charged Particle Tracking 28

2.5 Other Components 32

2.6 Event Reconstruction 32

3 Used Events and Event Selection **37**

3.1 Pb+Pb Events 38

3.1.1 Main-Vertex Longitudinal Position Cut 38

3.1.2 Centrality Selection 38

3.2 p+Pb and p+p Events 50

3.2.1 Main-Vertex Longitudinal Position Cut 50

3.2.2 Centrality Selection 52

4 Track Selection **55**

4.1 Tracks without Selection 55

4.2 Rejection of Discontinuous Tracks + Momentum Space Cut 59

5 Particle Identification **67**

5.1 Particle Identification by Specific Energy Loss 67

6 Corrections **75**

6.1 Correction for Non-Target Contamination and Loss by the Main-Vertex Cut 75

6.2 Trigger Bias Correction 77
6.3 Corrections from Monte Carlo 78
6.3.1 Feed-Down Correction 80
6.3.2 Tracking Inefficiency Correction 83
6.4 Acceptance Correction 83

7 Results and Discussion **89**
7.1 Identified Charged Hadron Spectra in Pb+Pb, p+Pb and p+p Reactions 89
7.2 A New Method for π^0 Spectrum Measurement 92
7.3 Anti-particle/Particle Asymmetry 93
7.4 Strange Meson Production 96
7.5 Baryon/Meson Ratios 100
7.6 Nuclear Modification Factors 102

Acknowledgments **113**

A Kinematic Variables and Particle Distributions **115**

B π^0 Spectra and a Robust Unfolding Method **119**

C Data Tables **125**

D Glossary of Notations and Terms **131**

List of Figures **133**

List of Tables **135**

Bibliography **137**

Summary **143**

Összefoglaló (Summary in Hungarian) **145**

1 Introduction

This thesis is an experimental study on the evolution of the single particle production spectra, when going from proton-proton through proton-nucleon to nucleon-nucleon collisions, at different collision energies, and at different collision centralities. For achieving such a comprehensive picture, an analysis of the data of the experiment CERN-NA49 was necessary, and the results of this analysis were compared to the higher energy results of the experiments at the RHIC accelerator. A remarkable part of the thesis concerns the details of the analysis procedures applied on the NA49 data. Most of these methods are the contributions of the *author*.

The existing cumulative experimental data, necessary for such a comprehensive study on proton-proton, proton-nucleus and nucleus-nucleus collisions, do not cover the energy region below $62.4\,\mathrm{GeV}$ at high transverse momentum (above $2\,\mathrm{GeV/c}$), therefore the filling of this energy gap in inclusive particle production data is of importance. The primary intention of this thesis is to provide *precision data* (systematic errors smaller than $\approx 5\%$) on the particle production spectra at $17.3\,\mathrm{GeV}$ nucleon-nucleon collision energy proton-proton, proton-nucleus and nucleus-nucleus reactions, on the *inclusive* level. A next iteration could be a *sub-inclusive* level study. Such studies are in progress in the NA49 experiment, and there is a wide range of such results by the RHIC experiments, however the sub-inclusive level is out of the scope of this thesis.

Throughout this study, the possible interpretations of the features of the measured data is tried to be kept as *model independent* as possible, or at least, the *amount of model dependence* is emphasized.

1.1 QCD and its Consequences

Quantum Chromodynamics (QCD) is part of the Standard Model of elementary interactions, which describes the interactions of the elementary particles with a high accuracy, to our present knowledge. QCD is responsible for the realization of the 'strong interaction' among the Standard Model particles, from which the hadronic interactions originate.

The QCD is a gauge theory (Yang-Mills theory) with $SU(3)$ as the gauge group, acting on the 'color' degrees of freedom of the fermionic matter fields. The 8 independent gauge fields are called gluons, and the matter fields are called quarks in the QCD

theory. The Lagrangian density of the QCD may be written as

$$L_{\mathrm{QCD}} = -\frac{1}{2}\mathrm{Tr}\, F_{\mu\nu}F^{\mu\nu} + \sum_{j=0}^{n_f} \bar{q}_j \left(\gamma^\mu \mathrm{i} D_\mu - m_j\right) q_j,$$

where D_μ is the covariant derivation defined by the gauge fields (may be expressed as $D_\mu = \nabla_\mu - \mathrm{i}gA_\mu$, ∇_μ being the spacetime derivative, A_μ being the $SU(3)$ Lie algebra representation valued gauge potential, and g being the coupling factor), $F_{\mu\nu} = \nabla_\mu A_\nu - \nabla_\nu A_\mu - \mathrm{i}g\left[A_\mu, A_\nu\right]$ is the curvature of D_μ, and q_j are the fermionic matter fields, on which the gauge group acts by the fundamental representation. There are n_f independent generations of the matter fields, the 'flavors'.

There are different known techniques in QCD to solve for the measurable quantities (cross-sections, decay rates etc.) of various processes. The most traditional approach is the perturbative QCD: perturbative calculations may be applied in any quantum field theory. Such calculations are based on the idea of getting the propagators of the particles by means of a power series expansion in the coupling factor g. These calculations, however, lead to divergent results. This phenomenon is treated by the renormalization methods, which subtract the divergences to obtain physically meaningful results. After the renormalization procedure, the coupling factor g is replaced by an effective coupling factor $\bar{g}$, depending on the momentum scale μ, which can be thought of as a typical momentum transfer in a given process. The first order perturbative calculation shows that the μ dependence of the strong coupling factor $\alpha_s := \frac{\bar{g}^2}{4\pi}$ is

$$\alpha_s(\mu) = \frac{4\pi}{(11 - \frac{2}{3}n_f)\ln(\mu^2/\Lambda^2_{\mathrm{QCD}})},$$

where Λ_{QCD} is the momentum scale of the strong interactions. By comparing first order perturbative QCD results to experiments, Λ_{QCD} was determined to be about $200\,\mathrm{MeV}$.

The μ dependence of the α_s uncovers an important property of the QCD theory: the asymptotic freedom. This means that the strong coupling factor α_s tends to zero as the momentum scale μ tends to infinity. This implies that in the high momentum transfer limit ('hard' processes), the perturbative QCD becomes applicable. However, in the low momentum transfer limit ('soft' processes), the non-perturbative effects become pronounced, as the strong coupling factor α_s diverges as μ tends to Λ_{QCD}.

There is no clearly drawn boundary, from where the purely perturbative calculations may be successfully applied in practice. For soft processes, phenomenological models were set up, which try to grab the most important momentum and charge

transfer mechanisms of a given reaction. Some examples of such models which received widespread attention are the VENUS [65], based on the Gribov-Regge theory of hadronic interactions; the UrQMD [24], which is mainly based on string excitation and fragmentation model combined with transport models; the HIJING/B$\bar{\text{B}}$ [62, 47], based on nucleon-nucleon interactions in terms of classical strings, and includes the junction mechanism, which can account for the high baryon stopping in nucleus-nucleus collisions as opposed to a naive partonic picture; the ALCOR [30], which is non-dynamical model designed for the description of nucleus-nucleus collisions, based on redistribution of quarks into hadrons, and is basically examining the formation of chemical equilibrium; the Nova [37], based on nucleon resonance excitation and decays, primarily designed to describe proton-proton collisions, based on the Hagedorn picture. These models, however, are not fundamental in the sense that they cannot be directly inferred from pure QCD. Due to the recent great increase of the calculation power of computer machines, purely QCD-based fundamental non-perturbative approaches also evolved: the lattice QCD. This approach is based on the idea of calculating the QCD Feynman integrals on discretized spacetime, and getting a continuum limit by refining the spacetime mesh. These numerical calculations suggest that the QCD possesses different thermodynamical phases, and a phase transition may occur at temperatures in the order of about $200\,\text{MeV}$. Such result is shown in Figure 1, which depicts the phase diagram of the QCD on the temperature (T) and baryochemical potential (μ_B) plane (calculation from [36]). The figure shows that there is a first order phase transition line between the (confined) hadronic and a deconfined phase (called the quark-gluon plasma phase), with a critical endpoint (second order phase transition), after which the transition becomes cross-over type. Many experiments in high energy heavy-ion physics were driven by this finding: experimental verification of such a phase transition phenomenon was of great challenge.

The calculations predict experimentally verifiable signatures of the quark-gluon plasma formation (see e.g. [25]). The most important such potentially observable effects are considered below.

1. **Strangeness enhancement.** In the deconfined quark-gluon plasma, the chiral symmetry is restored, therefore the quark masses are largely reduced in the medium, which results in enhanced strange hadron yields.

2. **Suppression of J/ψ yield.** In the deconfined quark-gluon plasma phase, the formation of charm – anti-charm quark bound state (J/ψ meson) is less probable,

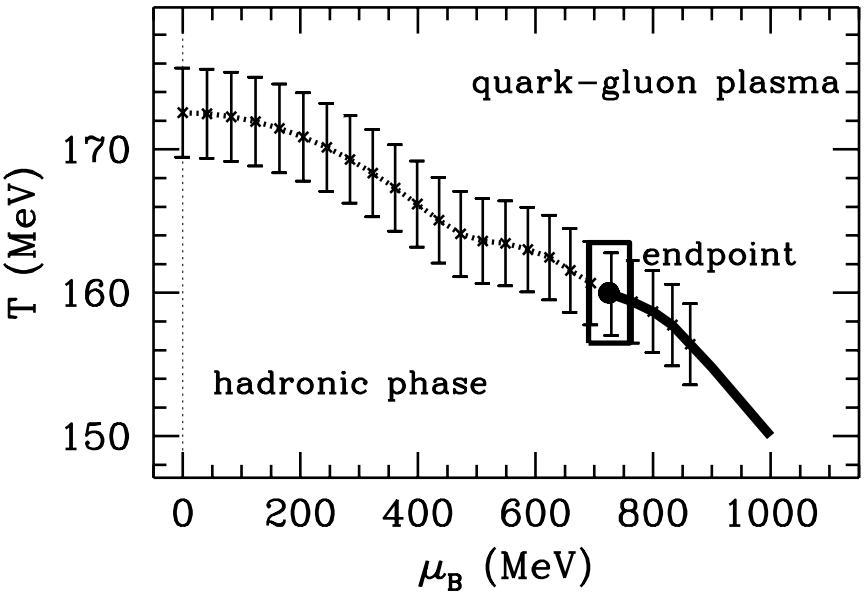

Figure 1: The phase diagram of the QCD from lattice calculations (figure from [36]).

as the color charges are being shadowed, resulting in a reduced amount of J/ψ production.

3. **Increased apparent source size.** Due to the expected long lifetime of the formed system, the apparent source size is expected to be increased. The source structure can be surveyed by Bose-Einstein correlation studies.

4. **Suppression of high transverse momentum particles.** In a deconfined quark-gluon plasma phase, the high transverse momentum particles originate from the fragmentation of high transverse momentum partons. If the system size is large enough (e.g. in a nucleus-nucleus collision as opposed to a proton-proton collision), the partons are expected to suffer radiative energy loss in the medium, leading to a reduction of high transverse momentum particle yields relative to that of scaled elementary (e.g. scaled proton-proton) reactions.

5. **Direct photon spectra.** The direct photons, produced in bremsstrahlung processes, quark anti-quark annihilations, quark-gluon Compton scatterings, can traverse the deconfined matter without modification, as they are unaffected by the strong interactions, thus they carry information on the temperature of the early stage of the collision.

6. **Fluctuations in hadronic observables.** If the thermodynamical evolution

of a hadronic or nuclear collision passes near the critical point, long wavelength fluctuations are expected to appear, which could be observed in the final hadronic state as increased amount of fluctuations in the hadronic observables, such as multiplicity and transverse momentum fluctuations.

This thesis mainly focusses on the effect of the suppression of high transverse momentum particles. The main question is whether this effect, discovered in 130 and 200 GeV nucleon-nucleon collision energy Au+Au reactions at RHIC, also exists at lower energies? This question is intended to be answered by using the 17.3 GeV nucleon-nucleon collision energy data of the experiment CERN-NA49 at the SPS accelerator.

1.2 Proton-Proton, Proton-Nucleus and Nucleus-Nucleus Collisions

When considering proton-proton, proton-nucleus and nucleus-nucleus reactions, important conditions of these collisions are largely different, which effect the particle production spectra. Such primary effect is the difference between the collision geometry. The proton-proton collisions are considered as elementary reactions, because the collision centrality cannot be resolved experimentally, as opposed to proton-nucleus and nucleus-nucleus collisions, in which case the event centrality may be determined in semi-direct ways. The simple geometrical picture of proton-nucleus and nucleus-nucleus collisions is shown in Figure 2. Microscopically, centrality can be characterized by the impact parameter b, which is the transverse distance of the colliding nuclei before impact. As depicted in Figure 2, the amount of nuclear material, participating in the collision, is uniquely determined by the collision centrality. The nucleons, not participating in the reaction are called *spectators*. It is seen, that the amount of participating nuclear matter is the largest for central nucleus-nucleus collisions, while in the proton-nucleus case, the proton probes the structure of the nucleus as it were a single participating nucleon from a nucleus-nucleus collision. Although, the impact parameter b cannot directly be measured, it is possible to resolve the collision geometry by experimental methods: e.g. by measuring the spectator energy in the nucleus-nucleus case[1], or by measuring the number of slow nucleons, produced by the break-up of the nucleus in a proton-nucleus collision[2]. The centrality of such events can be constrained by upper threshold for spectator energy or lower threshold for slow nucleon number, and the cross-section

[1] The lower the beam energy fraction of the spectator matter is, the more central is the collision.
[2] The higher the number of slow nucleons is, the more central is the collision.

fraction, selected by the imposed event cut, can be measured experimentally. The event centrality is then characterized by this fraction of total (inelastic) cross-section, which is independent from the way of the centrality determination, provided that the quantity, which is experimentally used for centrality measurement (spectator energy, number of slow nucleons etc.) is strongly correlated to the impact parameter, i.e. is a "good" measure of the collision centrality.

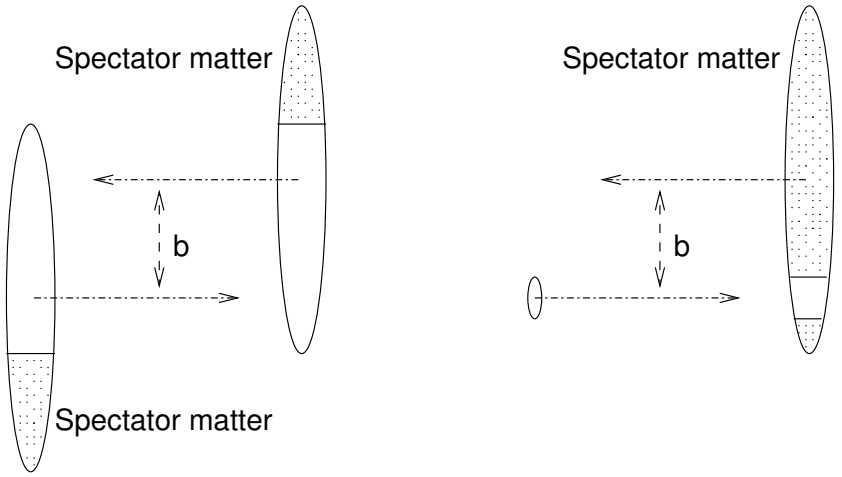

Figure 2: Spectator matter in nucleus-nucleus (left), and proton-nucleus (right) collisions.

It is also important to note, that the basic structure of collision kinematics does not only change with collision geometry, but also with collision energy. The longitudinal structure of collisions can be characterized by the distribution of the longitudinal kinematic variables of produced particles, such as the longitudinal rapidity y (for an overview on conventions of kinematic variables, see Appendix A). As shown in Figure 3, the produced system in a low energy nucleus-nucleus collision tends to form rather a spherically symmetric system, emitting particles isotropically ('Landau picture'), while with increased collision energy, the formed system is rather elongated in the longitudinal direction, and is emitting particles cylindrically ('Bjørken picture'). In particular, the produced particles (e.g. mesons) have a tendency of being emitted in the central regions, while the net-baryons (baryon content, inherited from the initial system) is rather emitted at the two longitudinal ends of the system. This phenomenon is commonly referred to as the decrease of 'baryon stopping' at higher collision energies. Therefore, in a thermodynamical picture it is plausible to state that at higher energies (at SPS and at RHIC), the 'source' of the produced particles is an expanding cylindrical structure rather than an expanding spheroid.

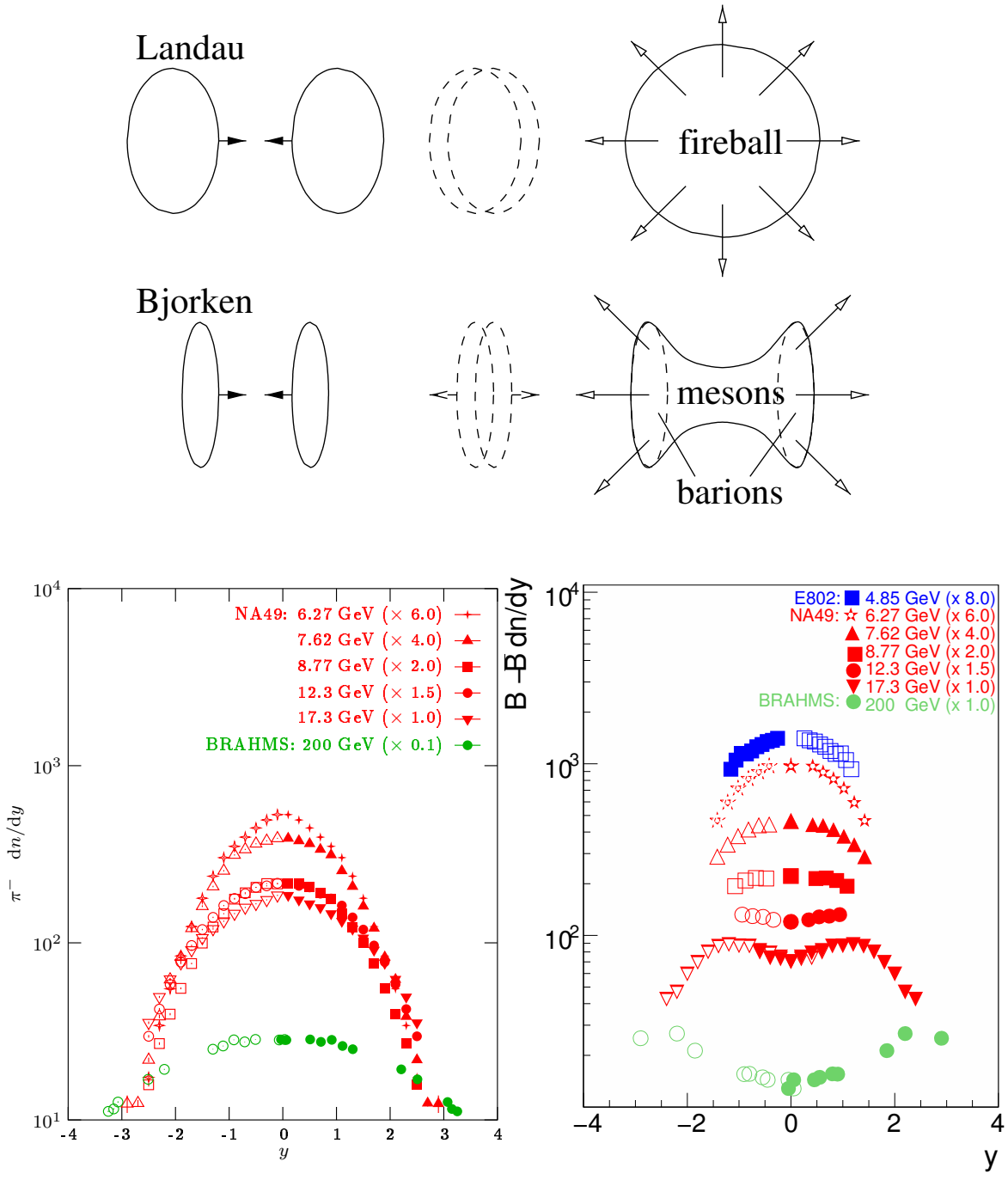

Figure 3: Top panel: qualitative overview of Landau and Bjørken picture of particle production in nucleus-nucleus collisions. Bottom left panel: a compilation on the variation of the rapidity distribution of π^- particles in nucleus-nucleus collisions, with increasing collision energy per colliding nucleon pair (data from NA49 and BRAHMS, [26]). Bottom right panel: a compilation on the variation of the rapidity distribution of net-baryons in nucleus-nucleus collisions, with increasing collision energy per colliding nucleon pair (figure from [31]).

The *blast-wave* parameterization description [50] was designed to factorize out the kinematic effect of such a source structure: in the framework of this model, the low transverse momentum particle spectra are explained by a common thermal spectrum, blue-shifted by the boost of such an expanding source of cylindric geometry, as suggested by the Bjørken picture. This parameterization is indeed successful in describing the low transverse momentum data both at RHIC and at top ion-SPS energies (see [13]).

A further major difference occurs between the proton-nucleus and the proton-proton, nucleus-nucleus reactions: the asymmetry. In the case of proton-nucleus reactions, the maximum of the particle production rapidity distribution is shifted toward the hemisphere of the outgoing spectator matter, both for meson and for baryon production. When comparing proton-nucleus particle production spectra to the spectra of proton-proton or nucleus-nucleus collisions, care has to be taken that such elementary kinematic effects do not mislead our conclusions.

1.3 High Transverse Momentum Particle Suppression

One of the most striking physical results of the RHIC experiments was the discovery of the suppression of high transverse momentum particles in high energy central nucleus-nucleus collisions, relative to that of scaled proton-proton reactions. This phenomenon was first discovered in the Au+Au RHIC data at 130 GeV collision energy per colliding nucleon pair ($\sqrt{s_{NN}} = 130\,\mathrm{GeV}$). The suppression effect was then found to be absent in d+Au collisions. The result was therefore often interpreted as an experimental evidence for the parton energy loss in the formed quark-gluon plasma.

The particle spectrum modification effect on a particle type t in a nucleus-nucleus collision A+B, relative to a reaction C+D, is measured by the *nuclear modification factor*, defined as

$$R_{A+B/C+D}(t) := \frac{N_{C+D}}{N_{A+B}} \cdot \frac{\text{Invariant yield}(A+B \to t+X)}{\text{Invariant yield}(C+D \to t+X)},$$

i.e. it is the scaled ratio of the invariant yields of particle type t in the given reactions (see Appendix A for the definition of invariant yield). The scaling factors, denoted by N_{A+B} and N_{C+D} in the formula, take care of the particle production scaling from the C+D reaction to the A+B, i.e. they strongly depend on the assumed particle production scenario. If the particle production scheme is assumed to be perturbative QCD-like, then the scaling factor should be the average number of binary parton-parton

scatterings, as in this picture, the particles are produced in the binary parton-parton interactions. This number is proportional to the number of nucleon-nucleon collisions, which is calculable by geometric Monte Carlo simulations (Glauber models). The nuclear modification factors are often taken relative to p+p reactions. An in-medium energy loss of the particles would be revealed by a nuclear modification factor below unity.

Figure 4 shows the nuclear modification of central Au+Au and d+Au reaction relative to p+p with binary collision scaling, at $\sqrt{s_{NN}} = 200\,\mathrm{GeV}$, as a function of the transverse momentum p_T, for unidentified particles (figure from [3]). It is seen that the particle yield relative to that of scaled p+p is suppressed in central Au+Au (the curve is below unity), while in the d+Au case, the particle yield is enhanced (the curve is above unity).[3] The arising difficulty concerning interpretation of the nuclear modification factors is that the scaling factor is largely model dependent. Of course, a possible extreme case could be a fully hard process dominated particle production scenario, which would impose binary collision scaling. A fully hard (partonic) scenario is expected to take over at large momentum transfer, therefore the yields of high transverse momentum particles are expected to be primarily effected by such a production scenario. However, there is no clearly known boundary, from where hard processes become dominant, therefore other production models are also necessary to consider. An extreme case of alternative particle production would result in particle yields proportional to the number of nucleons, participated in the reaction (wounded nucleon scaling). Such model was proposed in [27], and can describe the multiplicity distributions well, and also turned out to be successful in describing the RHIC d+Au rapidity spectra, as shown in [28]. A wounded nucleon scaling could arise from a resonance decay scheme for particle production: the nucleons are excited in the first collision, and then they go through subsequent decay.

The amount of model dependence was tried to be reduced by the RHIC experiments (PHENIX), by determining the ratio of the unknown scaling factors N_{C+D}/N_{A+B} experimentally. Their idea was to measure the nuclear modification factors of the direct photon spectra, which should scale with the number of binary collisions in a hard particle production scheme, and do not suffer modification in the possibly formed

[3]Such enhancement phenomenon in proton(deuteron)-nucleus collisions are often referred to as the 'Cronin effect'. Such effect was first outlined in the experimental results of [20], which is believed to be a consequence of multiple scattering of initial partons or hadrons, depending on the production picture. An initial multiple scattering would pump energy from the longitudinal degrees of freedom to the transverse degrees of freedom, resulting in the observed higher yield.

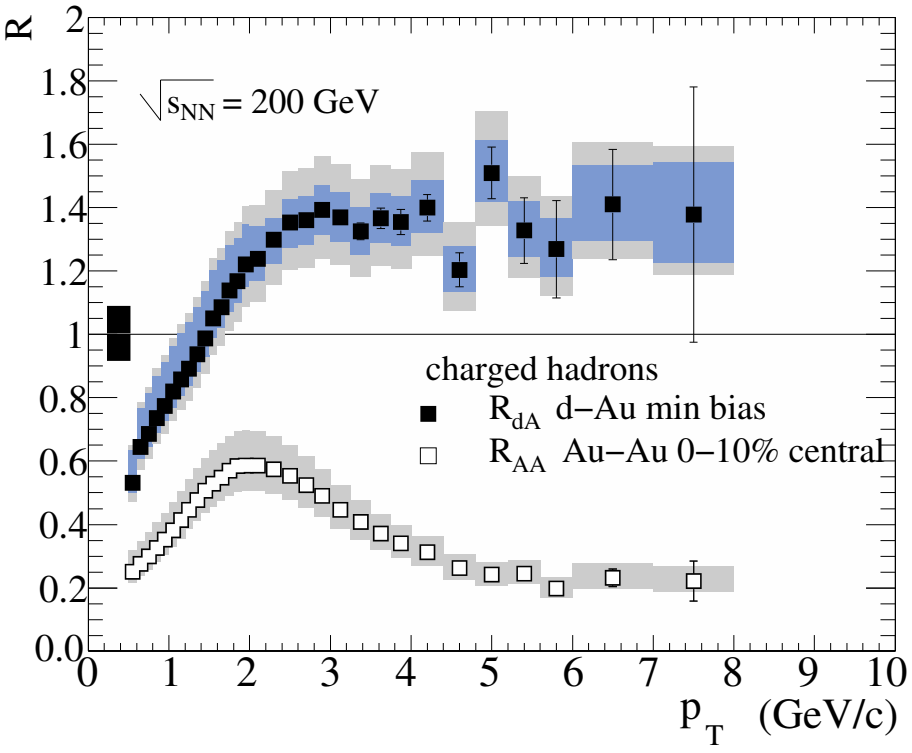

Figure 4: The central nucleon-nucleon and minimum-bias deuteron-nucleon nuclear modification factors (with binary collision scaling assumption), measured by the PHENIX experiment at $\sqrt{s_{NN}} = 200\,\mathrm{GeV}$ (figure from [3]).

quark-gluon plasma, as they do not interact strongly. Results, confirming binary collision scaling, has been published in [5], however it is far from convincing from the experimental point of view.[4] A dedicated measurement would be needed to answer this question.

The model dependence can, however, be reduced, if the disappearance of particles is shown in a sub-inclusive level. The momentum correlations in an event is often measured by the two particle azimuthal correlation function. Such correlation functions are defined by the two particle differential yields, normalized by the single particle production. The two particle azimuthal correlation functions can be measured by selecting a so called trigger particle in an event (being of a chosen type, and residing in a prescribed momentum space region), and recording the azimuthal distribution of the so called associated particles relative to this (associated particles are all the other

[4]Only integrated modification factor is shown, and the reference p+p spectrum is model calculation, which is tuned to data. If one tries to calculate the central to peripheral modification factor (which shall be introduced later), the errors (whenever known) are much too large, and allow a wide range of scaling assumptions.

particles, being of chosen type, and residing in a prescribed momentum space region). Typically, the accepted transverse momentum and rapidity of the trigger and associated particles are restricted to some interval, and the correlation is studied differentially also in these quantities. To remove artificial correlations form the measured raw azimuthal distribution, caused e.g. by non-complete acceptance, event mixing techniques are used: trigger and associated particles are taken from different events, providing microscopically uncorrelated samples. The azimuthal correlation functions are useful to visualize the (average) jet-structure of the events. To remove contributions of collective motion (elliptic flow) as a background, the jet-profile correlation functions are defined by discarding the Fourier components less or equal to 2 from the correlation functions. The jet-profile correlation functions of charged particles in $\sqrt{s_{NN}} = 200\,\mathrm{GeV}$ central Au+Au and p+p reactions are shown in Figure 5 (figure from [1]). Both the trigger and the associated particles are restricted to $3\,\mathrm{GeV/c} \leq p_T \leq 4\,\mathrm{GeV/c}$, and to a y interval around midrapidity. It is seen that the away-side jet is suppressed with respect to p+p. The jet-suppression picture, however is not such clear in all momentum bins: the jet-profile correlation function develops odd structures, which are likely to be projections of conic configurations, the origin of which is not completely clear, yet. For a differential study on the transverse momentum evolution of jet profile of charged particles around midrapidity at $\sqrt{s_{NN}} = 200\,\mathrm{GeV}$ central Au+Au and p+p collisions, we refer to [1].[5]

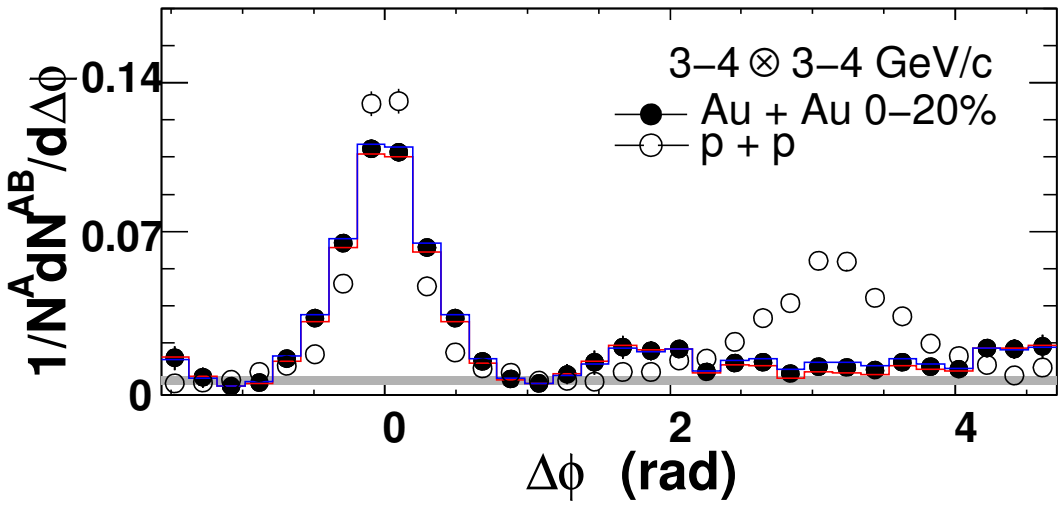

Figure 5: The away-side jet suppression in central nucleus-nucleus collisions, measured by PHENIX at $\sqrt{s_{NN}} = 200\,\mathrm{GeV}$ (figure from [1]).

[5] Similar studies are ongoing also in the experiment NA49.

The primary aim of this thesis is to calculate the nuclear modification factors as a function of p_T around midrapidity for identified particles, in $\sqrt{s_{NN}} = 17.3\,\mathrm{GeV}$ Pb+Pb and p+Pb reactions, thus providing an energy dependence picture of the on the nuclear modification phenomena. In order to avoid bias through the model dependence of the normalization factors, both extreme scaling scenarios (binary collision and wounded nucleon scaling) are considered. The results of sub-inclusive level studies are not yet finalized in our experiment, therefore this thesis shall only focus on the information, which can be extracted from the identified single particle spectra. The particle identification is crucial when comparing quantities derived from the single particle spectra at SPS and at RHIC energies, as the composition of the outcoming particles is completely different at these energies. This difference was depicted for the longitudinal degrees of freedom in Figure 3, from which we learn that the majority of the outcoming particles around midrapidity at RHIC are pions, whereas the particle yield at SPS is largely dominated by the net-baryons.

1.4 Experimental Possibilities at CERN-NA49

The CERN-NA49 experiment [8] is a fixed-target large acceptance hadron spectrometer. It has an advantage of being able to differentiate events and particles by means of a large variety of observables, some of which are summarized below.

- **Wide range of reaction types.** The SPS accelerator is capable of producing a large variety of particle beams, either directly, or by conversion on a production target. Possible beams are pion, proton, muon, electron beams, or heavy-ion beams such as lead-ion beams. The maximal beam energy of the accelerator in heavy-ion production is $158\,\mathrm{GeV/nucleon}$. The target material of the experiment can practically be chosen arbitrarily.

- **Centrality control.** Due to the fixed-target setup, all the spectator energy of a projectile nucleus can be measured by a downstream calorimeter, providing a precise control on centrality of nucleus-nucleus collisions. (In a collider experiment, such task his hard to realize, as an uncontrolled amount of the charged spectator fragments are swept out by the magnetic field of the collider.) For proton-nucleus collisions, the centrality can be controlled by measuring the number of the slow nucleons, emitted by the fragmented target nucleus.

- **Large momentum space coverage.** The NA49 experiment was designed to

have almost complete angular coverage for midrapidity or forward going charged particle tracks with low transverse momentum ($p_T \leq 2\,\mathrm{GeV/c}$). Although, the angular coverage is reduced for higher transverse momentum tracks, it is still far sufficient for the detection of high transverse momentum particles, with a good statistics.

- **Particle identification.** The key part of the experiment, the Time Projection Chambers, are able to provide a very good quality particle identification information via specific ionization. The experiment is also equipped with Time of Flight detectors, to cover those momentum space regions, where the charge, the momentum and the specific ionization is not enough information to disentangle particle types from each-other.

- **High statistics.** Although it is not easy to compete with the event statistics of the modern RHIC experiments, NA49 has one of the highest statistics, covering many reaction types (such as p+p, p+Pb, Pb+Pb) at the energy range of the SPS accelerator.

Besides the advantages, there are also some disadvantages of such an experimental setup, which mainly follow from the nature of fixed-target experiments.

- **High track density at midrapidity.** Due to the fixed target setup, the midrapidity tracks (which are of interest) reside in a high occupancy detector volume, as argued in Appendix A. Due to this kinematic effect, one has to deal with a much higher background of crossing tracks etc., compared to collider experiments, where the detector occupancy is minimal at midrapidity. The main analysis issue of this thesis is to reduce the contribution of this background without losing tracking efficiency.

1.5 Thesis Objectives

The study, presented in this thesis, concentrates on the experimental methods necessary for the measurement of the inclusive spectrum of π^+, π^-, p, $\bar{p}$, K^+, K^- particle production up to high transverse momenta in p+p, p+Pb and Pb+Pb collisions. Our analysis opens the analyzable transverse momentum region of NA49 data from $0\,\mathrm{GeV/c} \leq p_T \leq 1.5-2\,\mathrm{GeV/c}$ to a much larger coverage of $0\,\mathrm{GeV/c} \leq p_T \leq 5\,\mathrm{GeV/c}$, around midrapidity. The extracted particle spectra are used to determine the energy

dependence of certain properties of identified single particle spectra, such as nuclear modification. The aims of this thesis can be summarized as follows.

- **Provide high p_T particle spectra.** In the world data, there exists no comprehensive study on identified particle production at high transverse momenta in p+p, p+Pb, Pb+Pb collisions at the same energy, in the SPS energy range.
- **Energy dependence of nuclear modification.** By comparing our data to the higher energy RHIC results, an energy dependence picture of the nuclear modification effects is obtained. The presence of the high transverse momentum particle suppression at lower energy collisions is investigated.
- **Comparison to perturbative QCD calculations.** The resulting high p_T experimental data are compared to predictions of perturbative QCD-based in-medium energy loss models. Such comparisons may help in evaluating the 'hardness' of the elementary processes involved.

As the desired systematic errors to be reached were below $\approx 5\%$, considerable effort was invested in finetuning data extraction, calibration, simulation, and in correction methods for known systematic distortions.

The rest of the thesis is organized as follows.

Chapter 2 provides a brief description of the NA49 experiment. The basic principles of the detector operation and data reduction is also discussed.

Chapter 3 gives an overview of issues concerning the event cuts. Also centrality measurement is discussed here.

Chapter 4 deals with the problem of the large fake track background at high transverse momentum. This is a key part of our analysis.

Chapter 5 discusses the methods concerning particle identification by specific ionization.

Chapter 6 provides a detailed overview on correction methods, applied for reducing the effects of known systematic distortions.

Chapter 7 summarizes the main results of the thesis. Also the related publications of the author are listed there and discussed.

Appendix A gives an overview on the used kinematic variables and coordinate conventions.

Appendix B discusses an important result on an unfolding method in signal processing, developed by the author during the analysis.

Appendix C lists the measured experimental data in the form of summary tables.

Appendix D provides a list of notations and terms with their explanations, possibly not all known for a reader, who is not specialized in the field of experimental high energy heavy-ion physics.

2 Experimental Setup

The experiment CERN-NA49 is a fixed-target experiment, located at the H2 beam output line of the CERN-SPS accelerator at the so called North Area of CERN. The SPS accelerator is capable of producing proton and heavy-ion beams (Pb, In, S, C etc.), furthermore by using a fragmenter target, it is also capable of producing hadron, muon, and electron beams at reduced energy, as secondary beams. In case of secondary beams, the desired particle type is selected by tagging the produced particles using the CEDAR Ring Čerenkov counter [32], which tags the beam particles according to their velocity (and thus, according to their mass, due to the fixed beam momentum). The top beam energy for heavy-ion acceleration is $158\,\mathrm{GeV/nucleon}$. The data analyzed in this thesis were recorded by using this top ion-SPS beam energy Pb and p beams. When directing such a beam on a fixed target material, the resulting nucleon-nucleon collision energy inside the colliding nuclei is $\sqrt{s_{NN}} = 17.3\,\mathrm{GeV}$. The used target materials were either Pb (thin lead foil) or p (liquid hydrogen container) during the data taking. The data, analyzed in this thesis are therefore $\sqrt{s_{NN}} = 17.3\,\mathrm{GeV}$ Pb+Pb, p+Pb and p+p reactions.

2.1 Overview

The NA49 detector [8] is a wide acceptance hadron spectrometer for the study of hadron production in collisions of hadrons or heavy-ions at the CERN-SPS. The main components are four large-volume Time Projection Chambers (TPCs), as outlined in Figure 6.

The momentum space coverage is about 80% of some 1500 charged particles created in a central Pb+Pb collision at $158\,\mathrm{GeV/nucleon}$ beam energy. Two chambers, the Vertex TPCs (VTPC-1 and VTPC-2), are located in the magnetic field of two super-conducting dipole magnets (VTX-1, VTX-2; $1.5\,\mathrm{T}$ and $1.1\,\mathrm{T}$, respectively), while the two others (MTPC-L and MTPC-R) are positioned downstream of the magnets symmetrically to the beam line. The setup is supplemented by Time of Flight (ToF) detector arrays, which are not used in the present analysis, and a set of calorimeters (RCAL, LCG and VCAL – only VCAL is used in the present analysis). The NA49 TPCs allow precise measurement of particle momenta p with a resolution of $\Delta(p)/p^2 \approx (0.3 - 7) \cdot 10^{-4}\,(\mathrm{GeV/c})^{-1}$.

Thin Pb foils are used as target for Pb+Pb and p+Pb collisions (target arrangements a) and b) in Figure 6), and a liquid hydrogen cylinder of $20\,\mathrm{cm}$ length is used for

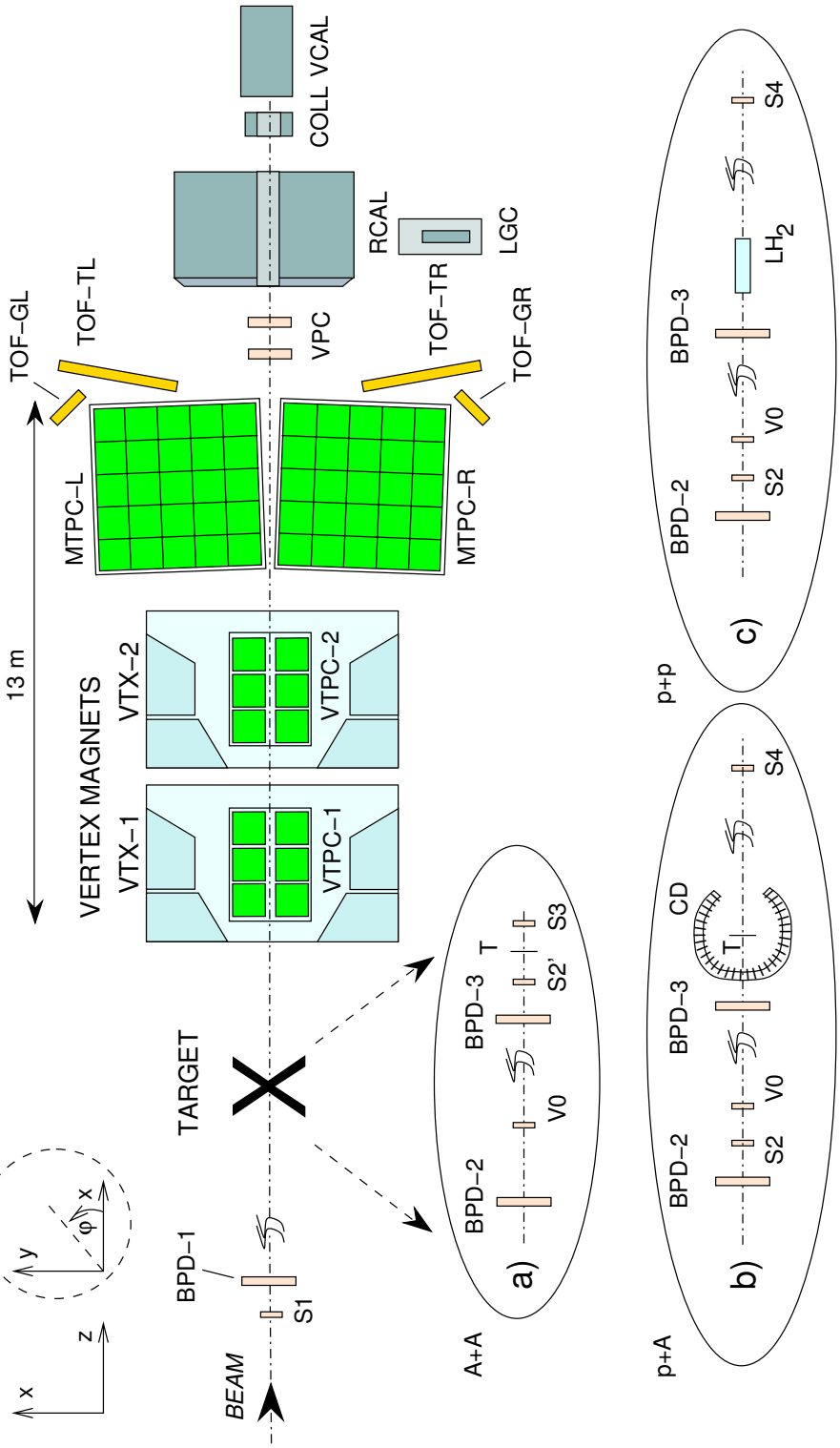

Figure 6: The architecture of the experiment CERN-NA49 (different beam definitions and target arrangements are also shown).

p+p interactions (target arrangement c) in Figure 6). The target is positioned about 80 cm upstream of VTPC-1. The target thickness is adjusted in such a way that the interaction probability of an incoming beam particle always kept to be $\approx 1\%$, thus the amount of multiple collisions in target is practically zero. In the case of the liquid hydrogen target, special care was taken to minimize the non-target material in the beamline: the container has $50\,\mu$m thin Mylar windows. There is also an additional window of $100\,\mu$m Mylar, which has to be traversed by the beam particle: the liquid hydrogen container is situated in a vacuum container for heat insulation.

2.2 The Trigger System

The trigger systems for different reactions are outlined in Figure 6 a), b), c).

If the beam is secondary (p beams in our case), the appropriate particle type is selected by the CEDAR Čerenkov detector far upstream of the experiment (not shown in Figure 6): its signal tags the particle if it is of the desired particle type. For primary beams (Pb beam in our case), such tagging is not needed, as the beam is not a mixture of different particle types.

The incident beam particle first traverses the S1 scintillator, which is 34 m upstream of the target. This counter sets the timing of the experiment. For p beams 5 mm thick scintillator is applied with 4 readout photomultipliers to improve time resolution. For Pb beams the scintillator is replaced by a $200\,\mu$m quartz wafer (light production by Čerenkov effect) to reduce the amount of material in the beamline.

The particle then traverses S2, which is 10 m upstream of the target. For p beam this is a 2 mm thick scintillator. For Pb beams, this is replaced by the S2', which is a Helium Gas-Čerenkov counter, and is adjusted to select such pulse height, which corresponds to the Pb^{82+}-ion's charge magnitude: by this selection the beam particle is validated as Pb^{82+}-ion, thus possible background, caused by upstream collisions on the beamline, is discarded.

To reduce the contamination by reactions upstream of the target, a veto scintillator V0 is applied between S1 and S2. This is a scintillator counter, with a hole in the middle of it for the beam, for vetoing deflected particles (possibly originating from upstream interactions on the beamline).

For a valid beam particle, the $S1 \cdot S2 \cdot \overline{V0}$ has to be true, furthermore if secondary beam is applied (p beam), then this has to be in coincidence with the CEDAR to select the appropriate beam particle type.

To select the interactions in the target, a so called interaction trigger is used. For p-induced reactions, the interactions in the target are selected by anti-coincidence of the incoming beam particle with a small scintillation counter (S4) placed on the beam line between the two vertex magnets VTX-1 and VTX-2, 4 m downstream of the target. For p+p interactions, this counter selects a trigger cross section of 28.5 mb out of the 31.6 mb total inelastic cross section. This event loss is due to the so called trigger bias: if an event contains particle touching the S4 counter, then the event is lost. The trigger bias effect is small, and the data can be corrected for it. For Pb-ion beams, the interaction trigger is provided by anti-coincidence with a Helium Gas-Čerenkov counter (S3) directly downstream of the target. The S3 counter (see also Figure 7) is used to select minimum-bias collisions by requiring a reduction of the Čerenkov signal. Since the Čerenkov signal is proportional to Z^2, this requirement ensures that the Pb projectile has interacted with a minimal constraint on the type of interaction. This setup limits the triggers on non-target interactions to rare beam-gas collisions, the fraction of which proved to be small, and the data can be corrected for it. The resulting minimum-bias trigger cross section for Pb+Pb is about 80% of the 7.15 b total inelastic cross section.

The beam alignment is precisely controlled by the beam-position detectors (BPD-1,2,3 in Figure 6). These are planar proportional chambers, with cathode strip readout. They are able to measure the beam particle hit position coordinates in the transverse plane with $\approx 170\,\mu$m and $\approx 40\,\mu$m precision for p and Pb beams, respectively. For p beams, these are also used for further reduction of background, caused by upstream interactions: the BPD-3 coordinates of the beam particle has to be consistent with the extrapolation of the BPD-1,2 hit coordinates, and with the nominal beam position. This way, the amount of deflected beam particles (possibly suffered upstream collisions) can be largely reduced.

2.3 Event Centrality Determination

For Pb+Pb reactions, the centrality of a collision is selected (on-line for central Pb+Pb, off-line for minimum-bias Pb+Pb interactions) by a trigger using information from a downstream calorimeter (marked VCAL on Figure 6), which measures the energy of the projectile spectator nuclear matter (see [48]). The architecture of the detector is shown in Figure 8.

The spectator part of the nuclei travel along the beamline and leave a fraction of

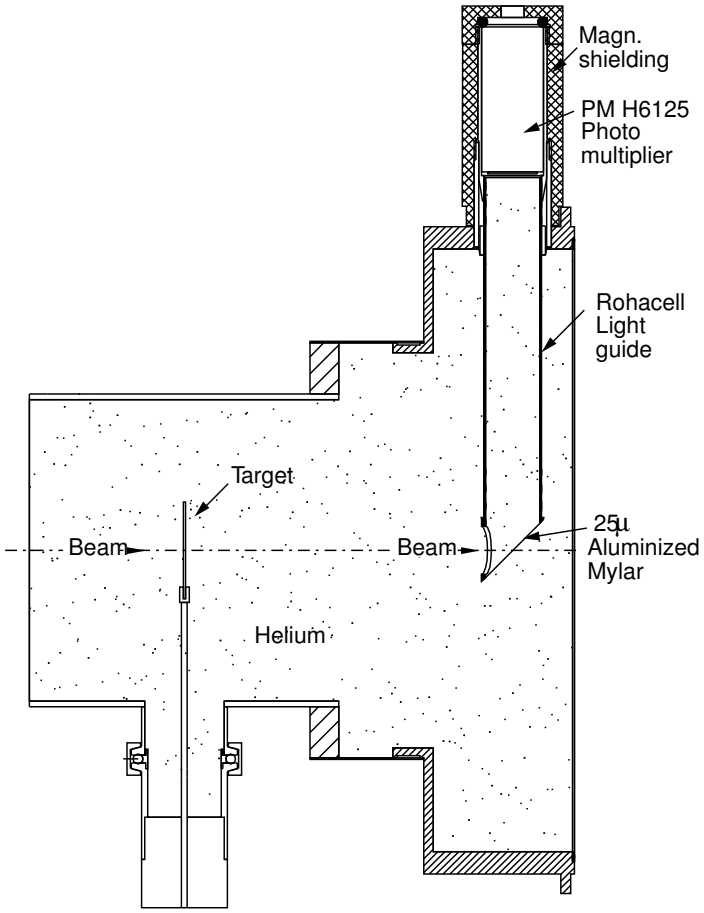

Figure 7: The schematic of the S3 Gas-Čerenkov interaction trigger for Pb beams.

the beam energy there (the spectator energy), which is proportional to the the volume of the spectator matter (or equivalently: the number of spectator nucleons), thus the centrality of the events can be determined (see also left panel of Figure 2). To reduce the background, caused by the produced particles at very forward angles, potentially hitting the surface of the VCAL detector, an iron collimator (marked COLL in Figure 6) is applied directly upstream of the VCAL, to absorb these particles. The precise setting of the collimator opening was carefully investigated in [21].

For p+Pb collisions, the centrality determination is not such direct as for Pb+Pb reactions. It is determined via the Centrality Detector (CD on Figure 6), which is an absorber foil around the target, surrounded by a cylindrical ensemble of proportional chambers, which measure the number of emitted slow particles (so called grey protons) via absorption (an extensive description can be found in [55]). This method uses the knowledge that the centrality of a proton-nucleus event is correlated to the number of

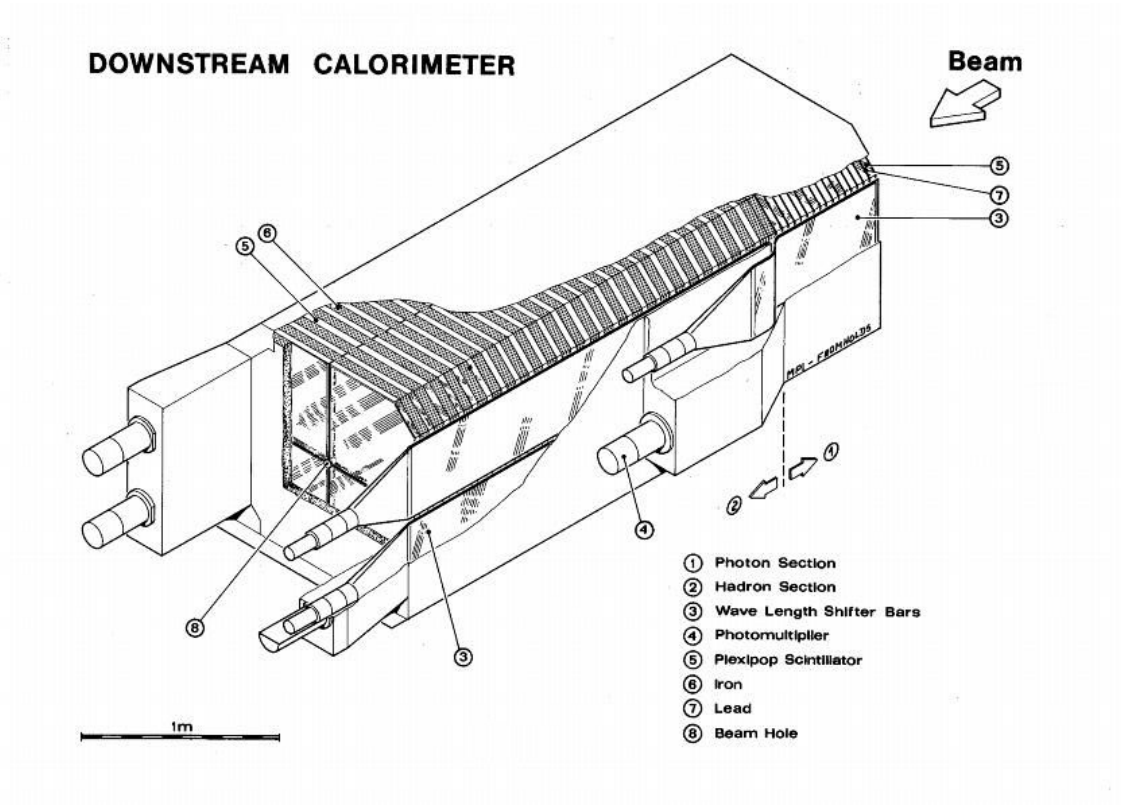

Figure 8: The schematic of the VCAL, used for centrality determination in nucleus-nucleus collisions.

emitted slow nucleons, evaporating from the surface of the hitted target nucleus (also discussed in [56]). An outline of the CD detector is shown in Figure 9. The proportional tubes have segmented cathode readout, thus the clusters of particles can be detected. The very slow particles (so called black protons) are cut off by the $200\,\mu$m copper absorber foil at $\approx 0.15\,\mathrm{GeV/c}$ momentum, while the high energy particles are cut off by setting an electronical threshold to limit the momentum range from above by $\approx 0.8\,\mathrm{GeV/c}$ momentum. The number of clusters (particle hits) are counted electronically, and can also be used for on-line triggering on centrality for proton-nucleus reactions, besides for off-line triggering.

2.4 Charged Particle Tracking

The tracker devices are the most important components of the detector setup. These consist of four large TPC (Time Projection Chamber) volumes. Two of these (VTPC-1, VTPC-2 on Figure 6) are situated inside the field of two large superconducting dipole magnets (VTX-1, VTX-2 on Figure 6), the standard setting of which are $1.5\,\mathrm{T}$ and

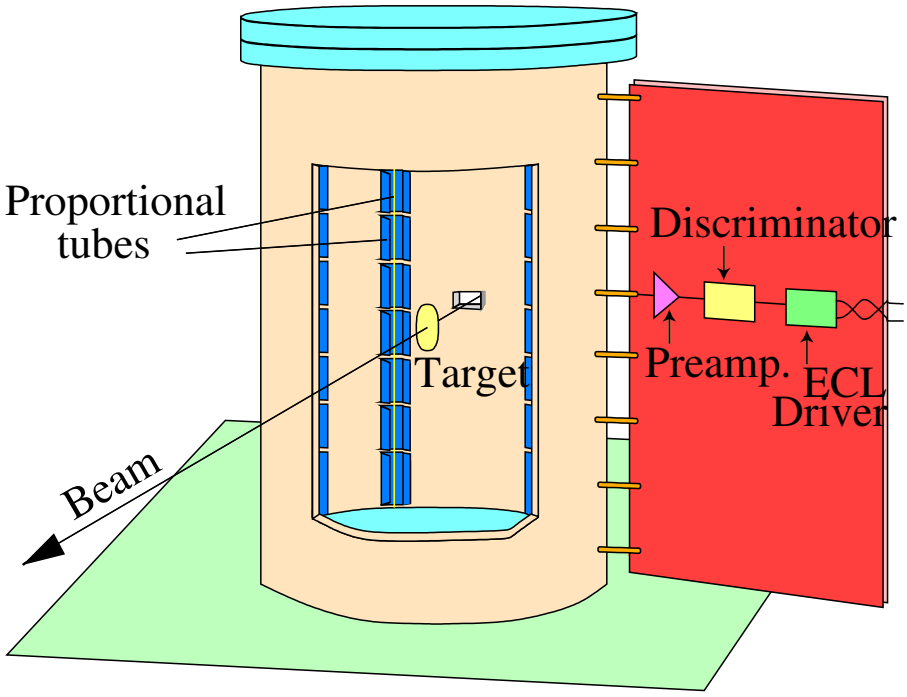

Figure 9: The schematic of the CD, used for centrality determination in proton-nucleus collisions. (Copper absorber foil between the target and the proportional tubes is not shown.)

1.1 T (maximum 5000 A), respectively, with 100 cm vertical gaps between the poles, where the VTPC-1 and VTPC-2 reside. These two TPC chambers are responsible for momentum measurement. The combined total bending power is 9 Tm over about 7 m, which is needed for the precise momentum measurement. The magnetic field is vertical: the nominal bending plane is the he $z - x$ plane, where the z axis is defined to be the beam axis, and x is perpendicular to z, both residing in the horizontal plane (thus the magnetic field is approximately parallel to the y axis). The magnetic field is controlled by Hall probes, and the inhomogeneities, mostly occurring at the side of the field and away from the nominal bending plane, are precisely logged, and are taken into account in the particle tracking software, as the particle tracking is very sensitive to the local variations of the magnetic field. The remaining two TPC volumes (MTPC-L and MTPC-R) are residing outside of the magnetic field, however, they play a very important role in the experiment: they extend the tracking volume, and perform a very significant task, namely due to their large coverage, they allow a precise measurement of the specific ionization (commonly denoted as $\frac{\mathrm{d}E}{\mathrm{d}x}$) of the particles, which is used for particle identification.

The operation principle of a TPC is outlined in Figure 10. A TPC detector is a

3 dimensional particle track detector: in 2 dimensions, it is basically operated as a multiwire proportional chamber, while in the 3-rd dimension, the drift time is used to get the position information, knowing the drift velocity with high precision.

A highly uniform large electric field (typically $\approx 200\,\mathrm{V/m}$) is applied to the gas volume of a TPC chamber, which is controlled by the HV Plate (at large negative electric potential), the Cathode Grid (at ground potential; also called Frisch Grid), and the Field Cage, which avoids the non-uniformity at the field borders (the strips of the Field Cage admit uniformly decreasing electric potential magnitude towards the Cathode Grid). The gas volume is filled with atmospheric noble gas mixture, in which the particles leave an ionization channel along their tracks. The produced electrons drift towards the Cathode Grid with a typical velocity of $1.5-2.4\,\mathrm{cm}/\mu\mathrm{s}$. The electrons first traverse the Gating Grid, which may be set to a negative potential, preventing electrons from arriving at the readout region: this facility is used to make the detector blind, when desired. The electrons then traverse the Cathode Grid (at ground potential). In the Sense/Field Wire plane, every second wire is set to a positive potential (Sense Wire) to attract electrons, the others are at ground potential (Field Wire) to shape the electric field. In the close neighborhood of the thin Sense Wires (typically of $20\,\mu\mathrm{m}$ diameter) the field strength is high enough that the drifting electrons initiate further ionizations, thus the charge signal is amplified by the working gas. In order to limit the amplification (i.e. to avoid discharges through sparks), a quenching gas is also added to the gas mixture (this is typically CO_2). A very commonly used working gas is the 70%-30% Ar-CO_2 mixture. The ionization avalanche, released near the Sense Wire induces a signal on the Pad Plane via capacitive coupling, thus finally the charge signal can be read out on the Readout Pads.

The parameters of the NA49 TPCs were primarily designed and optimized for large acceptance (total tracking volume is about $45\,\mathrm{m}^3$) and for good two-track resolution (optimized gas mixture: 90%-10% Ne-CO_2 in the VTPCs, and 90%-5%-5% Ar-CH_4-CO_2 in the MTPCs). For particles with transverse momentum below $2\,\mathrm{GeV/c}$ in the forward hemisphere, the coverage is almost 2π. With increasing transverse momentum, this decreases to a narrower azimuth interval. In 2001, the forward coverage was extended by a small supplementary TPC volume, the GTPC (not shown in Figure 6), between the VTX-1 and VTX-2 magnets (see an extensive study in [58]). This was only used for non-ion beams, due to the large ionization signal of the heavy-ions (the Gating Grid can be used in this case to make the chamber blind). In order to increase two-track resolution, the Readout Pads were chosen to be about $4-6\,\mathrm{mm}$ wide and

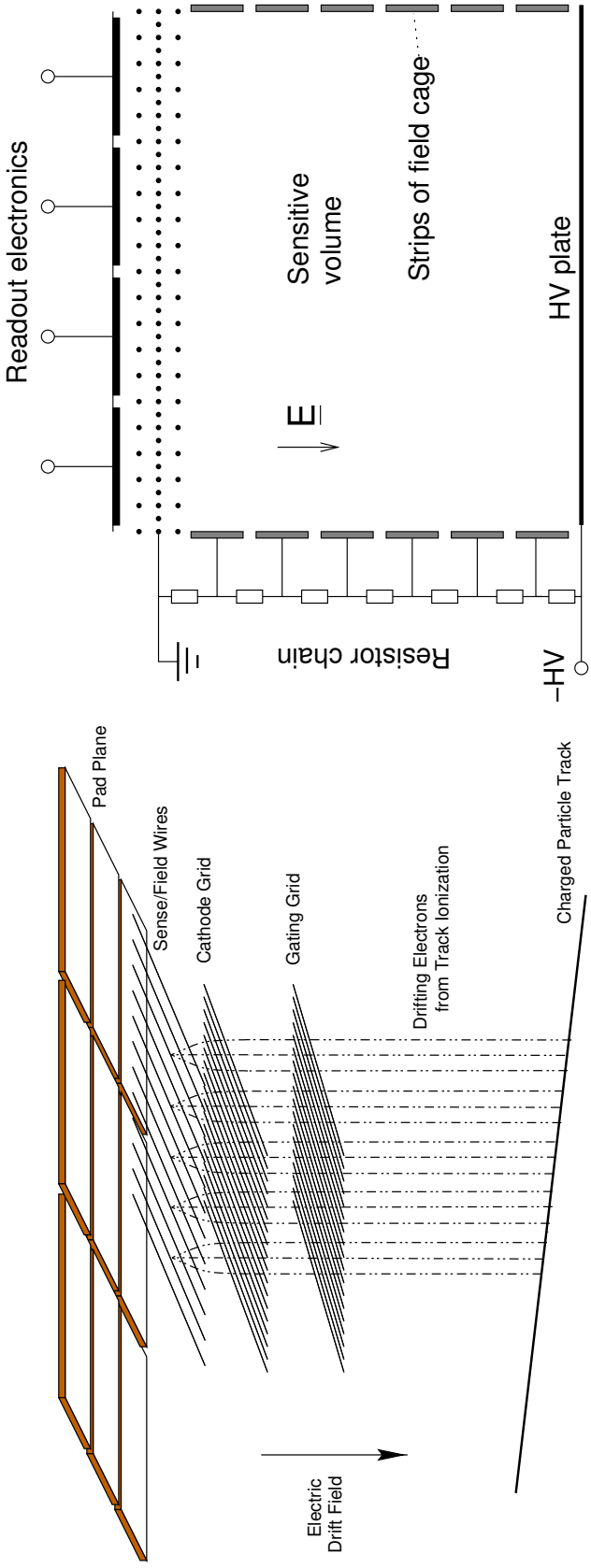

Figure 10: The principle of TPC operation. The lines indicate the direction of the electric field, which is followed by the drifting electrons.

$1.5-4\,\mathrm{cm}$ long, approximately being perpendicular to the beamline. The setup provides about $100\,\mu\mathrm{m}$ spatial resolution. The VTPCs contain 72 pad rows, while the MTPCs contain 96 of them. Thus the maximum number of pads crossed by a full-length track can be 168.

The main technical issues concerning TPC operation are mostly in connection with the control of the drift velocity. As the drift velocity is very sensitive to the pressure and temperature, the NA49 TPCs are located in an air-conditioned hut with temperature variations less then $\pm 0.1\,^{\circ}C$, furthermore the atmospheric pressure is constantly monitored, for the precise calculation of drift velocity. An other very important task is to get rid of electro-negative gas contaminations, which if present, simply kill the signal due to electron absorption. Such a typical electro-negative gas contamination is O_2 from the air. A dedicated gas filtering and circulating system ensures the quality of the working gas: the O_2 content is kept below $2-4\,\mathrm{ppm}$. An other prevention of O_2 contamination is an N_2 gas envelope around the TPC chambers, which is shown for the VTPCs as an example in Figure 11.

The precise geometrical alignment of the detector volumes are performed via optical alignment to a $0.2\,\mathrm{mm}$ precision. Further finetuning is possible by detecting the SPS muons, travelling parallel to the beam axis, when the magnetic field is switched off.

2.5 Other Components

Further devices are the ToF (Time of Flight) walls, the VPCs (Veto Proportional Chambers), the RCAL (Ring Calorimeter), and the LGC (Leadglass Gamma Calorimeter), which are not used in the analysis to be presented. The ToF walls were built for particle identification by flight time measurement (which tells the particle mass, knowing the flight path length and the particle momentum from the track reconstruction), the VPCs are built for tagging charged particles reaching the surface of RCAL, and RCAL is typically used for neutron detection in proton-proton and proton-nucleus reactions, together with the VPCs. The LGC is a new component of the detector, which was installed to be able to trigger on high transverse momentum π^0 particles (see [38]).

2.6 Event Reconstruction

As in most particle physics experiments, the issue of data reduction is a crucial problem at NA49. A typical raw event can reach the size of $100\,\mathrm{Mbyte}$ before any reduction. The major part of a raw event consists of the data from the tracking devices. These are

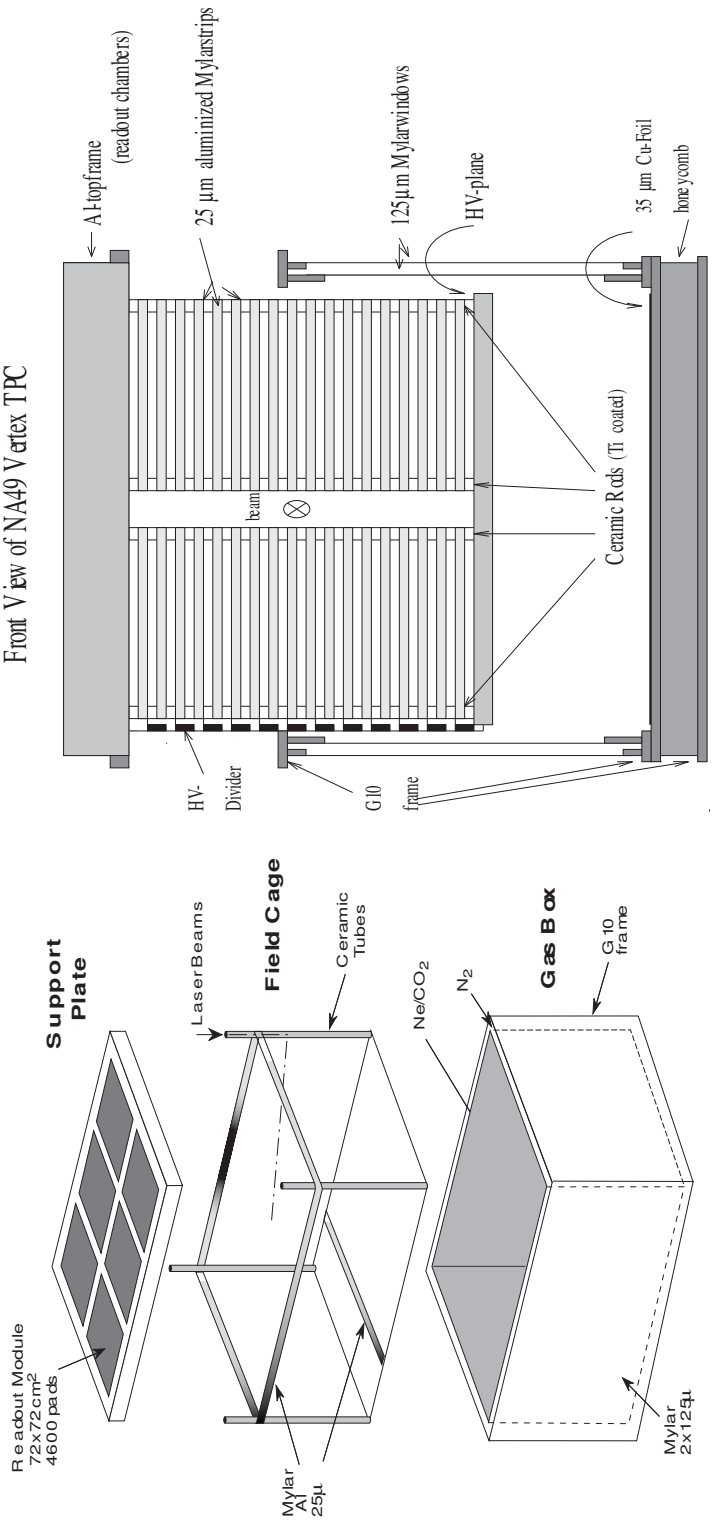

Figure 11: The schematic of the setup of the VTPCs. Note the N_2 gas envelope around the chamber.

the ADC counts of the charges, measured on the TPC pads. The charges are picked up from the Readout Pads by the Front End cards, the signals are amplified, shaped, and digitized. The total $50\,\mu$s drift time is subdivided into a time series of 512 time buckets of deposited charges for each pad. This makes it possible to reconstruct the vertical (y) track coordinates from the time delay (drift time) of the signal, knowing the drift velocity. The digitized charges are then moved to the Control and Transfer boards, which are responsible for the transfer of the data from the readout chambers to the Control Room. The transfer is realized by a serial optical fiber link. In the Control Room the VME based receiver board process the data: it performs noise and zero suppression to reduce the data to about $1.5 - 8\,$Mbyte/event. This reduced data is then transfered to the central Data Acquisition system, and are recorded on Raw Data Tapes. The apparatus is capable of storing about $20 - 30\,$events/spill in each SPS spill, where a typical beam spill is of $2 - 4\,$s duration, repeated in about $14 - 16\,$s long cycles.

For permanent storing and processing, the data need further reduction. The events, stored on the Raw Data Tapes, are processed off-line by an event reconstruction software. The key part of the software is the charged particle track reconstruction from the TPC hits. This is performed according to the following philosophy.

1. **Cluster finding.** The close-by TPC pads with high ADC values are collected and merged to form a space point.

2. **The $\vec{E} \times \vec{B}$ correction.** The point coordinates are corrected for the so called $\vec{E} \times \vec{B}$ effect ($\vec{E}$ being the electric and $\vec{B}$ being the magnetic field strength vector), which is caused by the Lorentz force on the drifting electrons, proportional to the previous quantity. This effect distracts the drifting electrons from the $\vec{E}$ field lines, and can be up to a few cm-s.

3. **Local tracking.** The individual space points are collected into local track pieces.

4. **Global tracking.** The local track pieces are matched to form global tracks.

5. **Main-vertex finding.** The most likely position of the reaction point is determined by using the global tracks.

6. **Secondary-vertex finding.** Secondary vertices, potentially belonging to neutral weakly decaying particles, are determined by those tracks, which do not start from the main-vertex.

7. **Momentum fitting.** The momentum of each track at its mother vertex point (at the main-vertex, or at a secondary vertex) is fitted.

The reconstructed events are finally stored on Data Summary Tapes, after which the events are ready for statistical analyses.

3 Used Events and Event Selection

The present analysis is performed on the full available Pb+Pb, p+Pb and p+p data at 158 GeV/nucleon beam energy, which which corresponds to 17.3 GeV nucleon-nucleon collision energy in the nucleon-nucleon center of mass system. The used event datasets are listed in Table 1. The events inside a dataset are grouped into runs, which are approximately 10 k successively collected events, and are labeled by a unique run number. The data are collected with the full strength standard magnetic field setup, however, for some datasets the direction of the magnetic field was swapped for different studies (std+ corresponds to normal field direction and std− corresponds to the opposite direction).

Tag	Reaction	$E_{\mathrm{Beam}}/A_{\mathrm{Beam}}$	Centrality	Magn.field	Year	Events
00B	Pb+Pb	158 GeV	Central	std+	1996	400 k
00M	Pb+Pb	158 GeV	Min-bias	std+	1996	256 k
00N	Pb+Pb	158 GeV	Min-bias	std−	1996	150 k
00O	Pb+Pb	158 GeV	Central	std−	1996	530 k
01I	Pb+Pb	158 GeV	Central	std+	2000	3 M
01J	Pb+Pb	158 GeV	Min-bias	std+	2000	340 k
00E	p+Pb	158 GeV	Min-bias	std+	1999	1.3 M
02D	p+Pb	158 GeV	Central	std+	2001	1.6 M
00D	p+p	158 GeV	Min-bias	std+	1999	1.2 M
00R	p+p	158 GeV	Min-bias	std+	2000	2.7 M
02G	p+p	158 GeV	Min-bias	std+	2002	2.9 M

Table 1: The used datasets.

As a minimum requirement, a filtering was done for duplicate events, i.e. events having identical (run_number, event_number) identifier were analyzed only once. The duplicate events most probably originate from accidental multiple reconstruction of some events. Duplicate events make only a negligible contribution: the fraction of duplicate events is well under 1%, therefore this filtering does not make a remarkable change.

Events and tracks only with good `iflag` were analyzed. This flag determines whether the event reconstruction and momentum fitting was successful.

3.1 Pb+Pb Events

3.1.1 Main-Vertex Longitudinal Position Cut

As can be seen from the experimental setup, the beam particles have to travel a short path in the air before they reach the Pb target foil, used in Pb+Pb events. Therefore, among the real Pb+Pb 'target' events, there is a certain amount of Pb+gas 'gas' event contamination, which are mostly Pb+N or Pb+O reactions in the air. To investigate the possible non-target contamination in our event samples, the distribution of the reconstructed longitudinal main-vertex[6] position V_z was measured for different total multiplicities[7]. This is shown in Figure 12. The largest amplitude peak corresponds to the target-peak, the smaller amplitude peak corresponds to the mylar foil closing the vacuum beam pipe, and the flat background corresponds to interactions in the air.

As can be seen from the figure, the lowest multiplicity events have the largest width V_z peak, as the main-vertex is less constrained when the number of tracks is smaller. If a cut is imposed on the V_z to select the target-peak, the cut window should be at least $\pm 3\cdot$ standard deviation of the V_z peak of the lowest multiplicity events, i.e. should be $\pm 3 \cdot 0.75\,\mathrm{cm}$. Otherwise, a certain amount of low multiplicity events will be lost due to the too narrow V_z window. We shall refer to the $\pm 3 \cdot 0.75\,\mathrm{cm}$ as the 'wide V_z-cut'. In the case of the wide V_z cut, the target event loss is negligible. Then residual non-target event contamination can be estimated by the flat beam+gas background situated in front of the target-peak. The V_z window covering this flat region, selecting purely the beam+gas contribution, shall be called the 'gas V_z-cut'. Later, in the particle yield studies we shall use the $\pm 1 \cdot 0.75\,\mathrm{cm}$ cut ($\pm 1\cdot$ standard deviations in the case for lowest multiplicity events), which we will refer to as the 'narrow V_z-cut'. In this case, the target event loss in the case of low multiplicity events, caused by the narrow V_z window, also has to be considered. If not otherwise stated, the wide V_z-cut shall be applied.

3.1.2 Centrality Selection

In our experiment, the centrality of the Pb+Pb events are controlled by the fraction of the beam energy deposited in the VCAL (spectator energy).

Before using the VCAL response as a measure of centrality, it has to be corrected for some effects. First of all, it turned out that the amplification and the offset of VCAL

[6] The reconstructed collision point is called the main-vertex.

[7] The total number of charged tracks in an event is called the total multiplicity.

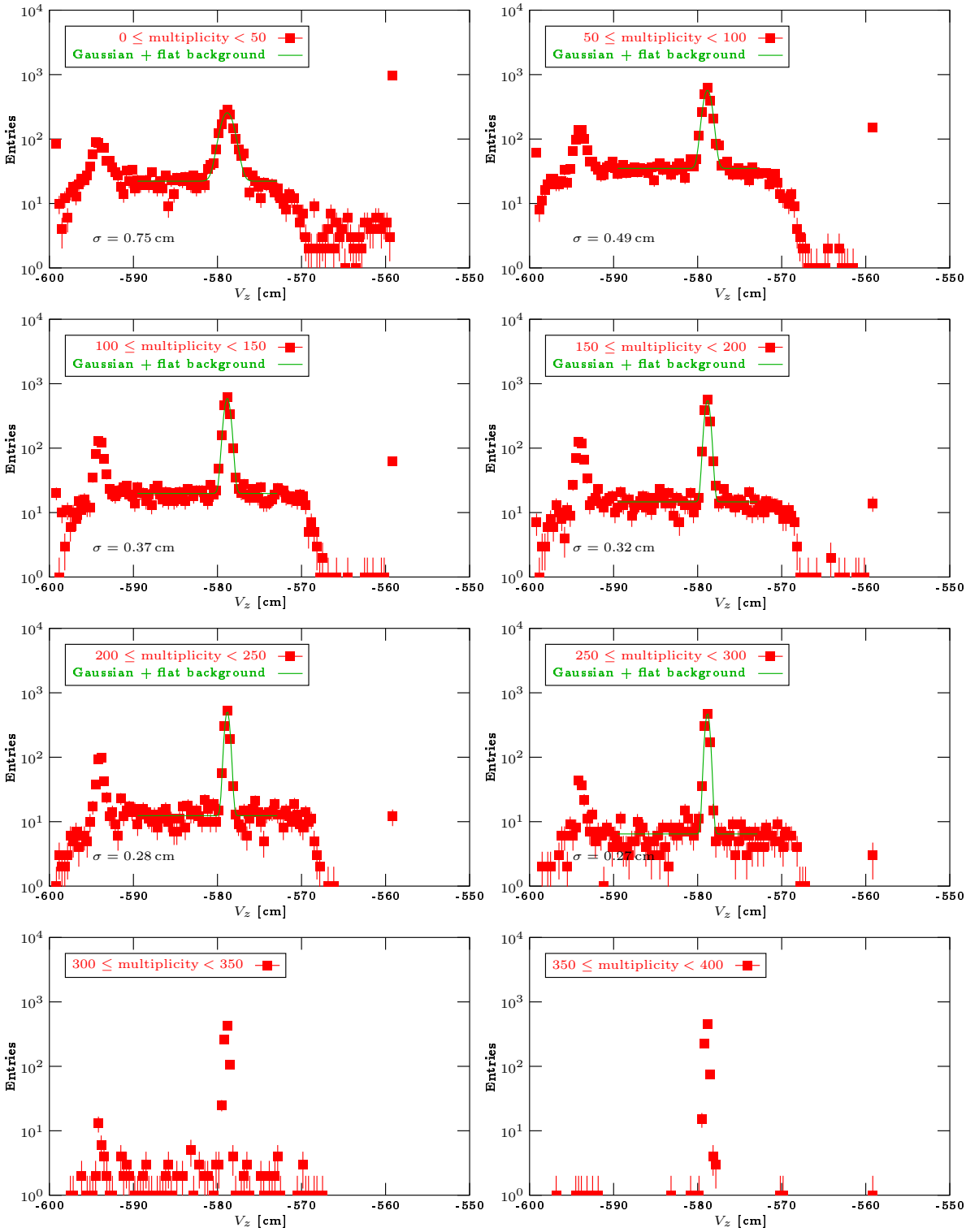

Figure 12: Distribution of main-vertex longitudinal position in low multiplicity Pb+Pb events.

was slowly varying in time, i.e. the energy response scale of the VCAL was slightly different on a run-by-run basis on a large time scale. Therefore, a time-dependent offset and amplification correction was applied on the VCAL response on a run-by-run basis (see [39]).

The time-dependence calibration is based on the idea of making the correlation of the VCAL energy to multiplicity to be time-independent. For simplicity of implementation, the procedure exploits the fact that the correlation of the VCAL energy to total multiplicity may be approximately parameterized by a straight line, as it is shown in Figure 13.

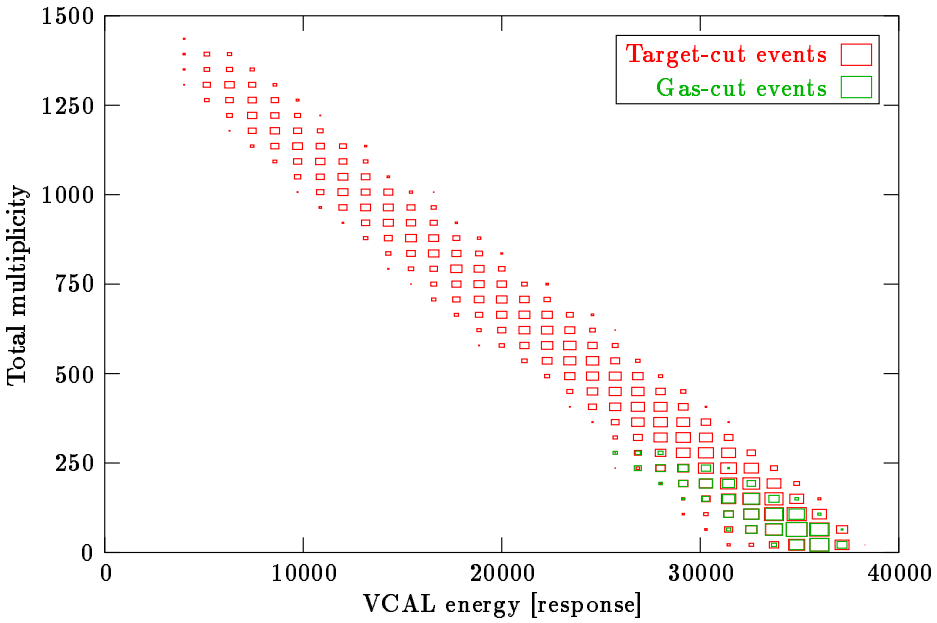

Figure 13: Correlation of VCAL energy and total multiplicity.

As the track density in a heavy-ion collisions can be pretty large, the fraction of fake tracks in an event can be rather high. To be safe from miscounting the total multiplicity because of the high number of the fake tracks, a stable set of tracks was selected for counting the multiplicity for time-dependence calibration purposes. The cuts, selecting the stable track set, were the following:

`iflag`$==0$,
only right-side tracks,
potpoints in VTPC1+VTPC2 > 20, and in MTPC > 20,
points/potpoints in VTPC1+VTPC2 > 0.5, and in MTPC > 0.5,
fit impact parameter x-coordinate $< 4\,\mathrm{cm}$, and y-coordinate $< 4\,\mathrm{cm}$,
transverse momentum $< 2\,\mathrm{GeV/c}$.
As this section is not dedicated for the details of the tracking analysis, the discussion of these notions will come later in Chapter 4.

The time-dependence calibration procedure went as follows: the scatter plot of the VCAL energy and the multiplicity of this stable track set was recorded for each run. A straight line of the form

$$E_{\mathrm{VCAL}}(\mathrm{run}) \mapsto a_{\mathrm{run}} \cdot E_{\mathrm{VCAL}}(\mathrm{run}) + b_{\mathrm{run}}$$

was fitted to the $E_{\mathrm{VCAL}}(\mathrm{run}) \mapsto$ Multiplicity correspondence of each run in the non-peripheral region. This is shown in Figure 14. The peripheral region was avoided by a cut in the E_{VCAL} scale: only the lower half of the E_{VCAL} scale was used for the fit to rule out the effects of the peripheral region (e.g. beam+gas contamination).

After this run dependent parameterization of the $E_{\mathrm{VCAL}}(\mathrm{run}) \mapsto$ Multiplicity correspondence, the time-dependence calibrated E_{VCAL} was obtained by the formula

$$E_{\mathrm{VCAL,corr}}(\mathrm{run}) = \left(E_{\mathrm{VCAL}}(\mathrm{run}) - \frac{b_{\mathrm{ref}} - b_{\mathrm{run}}}{a_{\mathrm{run}}} \right) \cdot \frac{a_{\mathrm{run}}}{a_{\mathrm{ref}}},$$

to make the $E_{\mathrm{VCAL,corr}}(\mathrm{run}) \mapsto$ Multiplicity correspondence run independent (offset and amplification correction). This recalibration ensures, that the E_{VCAL} scale of each run is identical to the scale of the arbitrarily chosen reference run 'ref'. (In our analysis this run was 1468, a Pb+Pb minimum-bias run, which had the most permissive trigger condition.) The recalibration coefficients are shown in Figure 15.

The scatter plot and straight line fit for each run was checked by eye to ensure that the rapid changes in calibration parameters are not due to bad fit quality or corrupted runs.

To obtain the event centrality from the VCAL energy, further investigations are needed. The 'centrality' of an event with E_{VCAL} energy deposited in VCAL is defined

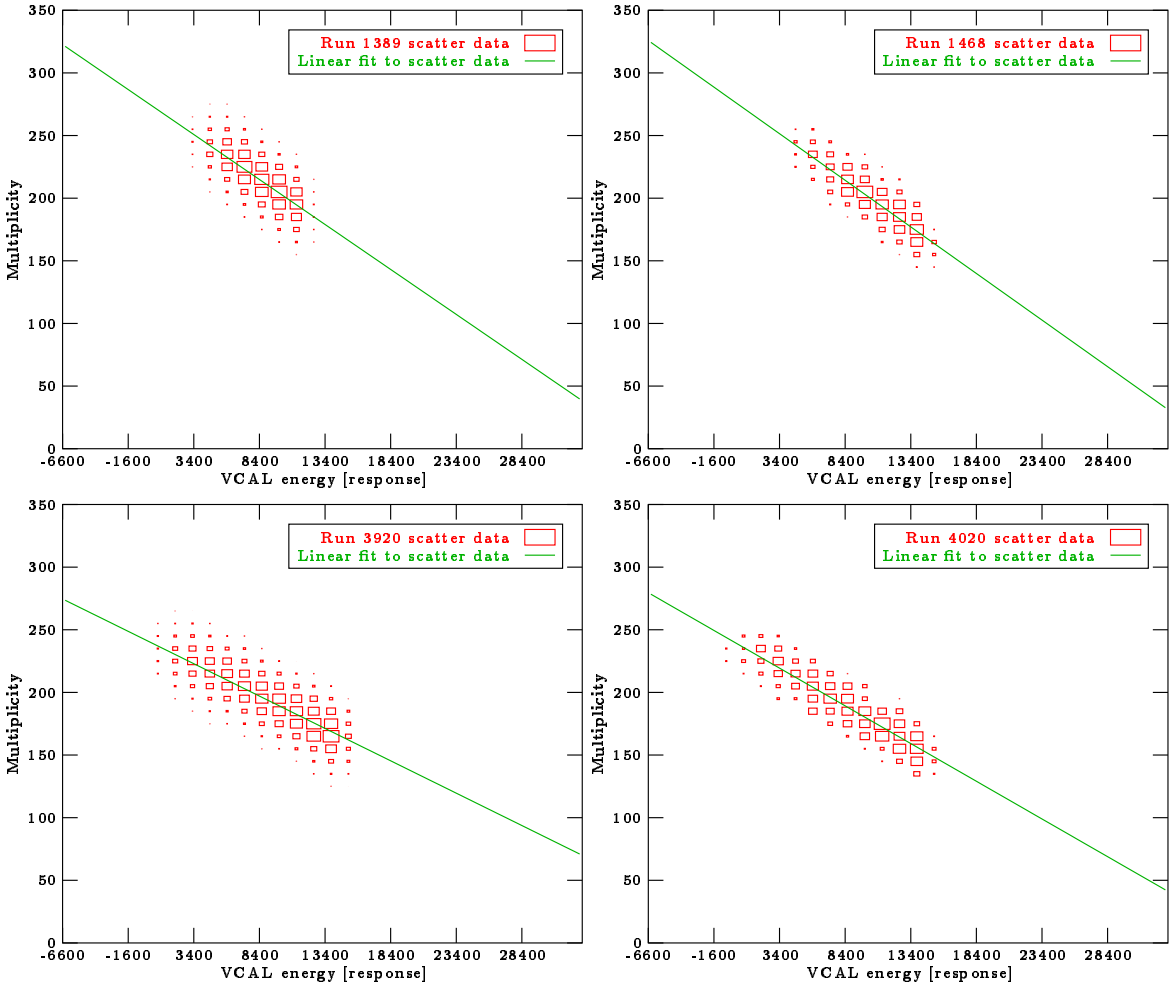

Figure 14: Time-dependence calibration of VCAL energy scale.

by the running integral

$$\int_0^{E_{\mathrm{VCAL}}} \frac{1}{\sigma_{\mathrm{Inel}}} \frac{\mathrm{d}\sigma(E'_{\mathrm{VCAL}})}{\mathrm{d}E'_{\mathrm{VCAL}}} \mathrm{d}E'_{\mathrm{VCAL}},$$

where σ_{Inel} is the total inelastic cross-section of the Pb+Pb events, and $E_{\mathrm{VCAL}} \mapsto \frac{\mathrm{d}\sigma(E_{\mathrm{VCAL}})}{\mathrm{d}E_{\mathrm{VCAL}}}$ is the differential cross-section as a function of the VCAL energy. In other words: centrality is defined to be the fraction of total inelastic cross section below the VCAL energy value E_{VCAL}. The total inelastic cross-section of Pb+Pb events was measured previously (see [35]) with an extrapolation of a series of trigger cross-section measurements: the measured value is $\sigma_{\mathrm{Inel}} = 7.15\,\mathrm{b}$. The differential cross section as a function of E_{VCAL} is defined by the probability density function of E_{VCAL} multiplied by

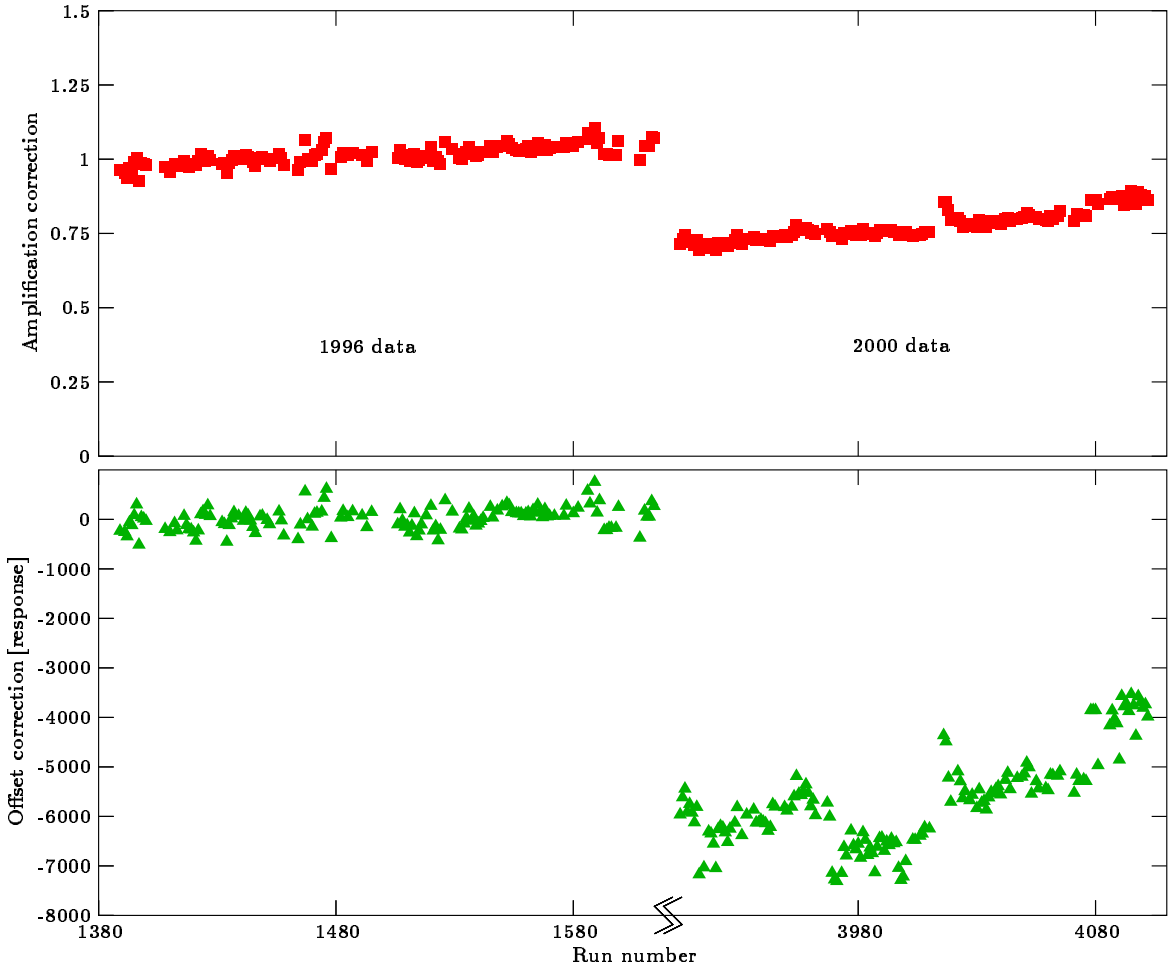

Figure 15: Time-dependence correction parameters of VCAL energy scale.

the trigger cross-section, thus can be measured experimentally. This is also discussed in [43].

The probability density function of E_{VCAL} can simply be obtained by histograming E_{VCAL}, and by normalizing the area of the histogram to 1. To avoid contamination by beam+gas events, the beam+gas contribution to the E_{VCAL} histogram was also collected by applying the gas V_z-cut, then it was subtracted from the E_{VCAL} histogram, obtained by the wide V_z-cut around the target peak. Before the subtraction, the gas contribution was scaled by the ratio of the V_z window sizes of the wide V_z-cut and the gas V_z-cut, as the width of the two windows are not equal. This non-target subtraction procedure is shown in Figure 16. Thus, the probability density function of E_{VCAL} can be obtained.

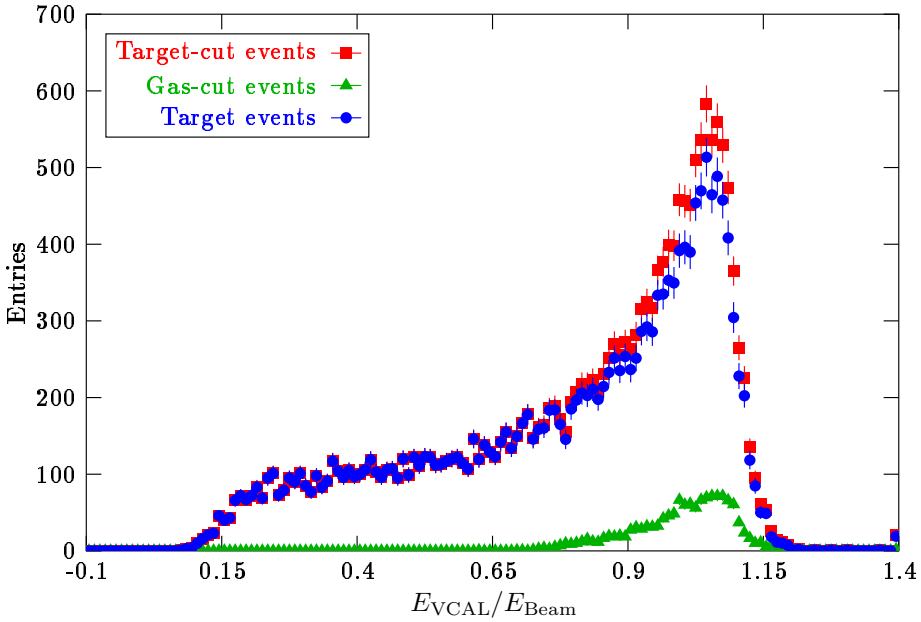

Figure 16: Subtraction of non-target contamination from the VCAL energy spectrum.

To measure the trigger cross-section, the following procedure was used. The trigger cross-section can be determined by $\sigma_{\mathrm{Trig}} = p_{\mathrm{Trig}} \cdot \frac{M}{N_{\mathrm{A}} \cdot \rho d}$, where M is the molar mass of the target material, N_{A} is the Avogadro number, ρ is the density of the target material, and d is the thickness of the target foil, furthermore p_{Trig} is the trigger probability (probability of having a recorded reaction induced by the beam particles). As M, ρ and d is known, only the trigger probability has to be measured to determine the trigger cross-section. The trigger probability can be measured by the distribution of the number of non-trigger gated events $\Delta N_{\mathrm{Gated}}$ passed between subsequent triggered events ($\Delta N_{\mathrm{Gated}}$: the number of beam particles which did not trigger recorded reactions between two subsequent recorded reactions). $\Delta N_{\mathrm{Gated}}$ can take any non-negative integer value. This quantity is also measured by our DAQ system. If the probability density function $\Delta N_{\mathrm{Gated}} \mapsto P(\Delta N_{\mathrm{Gated}})$ of $\Delta N_{\mathrm{Gated}}$ is known, then the trigger probability p_{Trig} can be determined as $p_{\mathrm{Trig}} = P(0)$, i.e. the probability of having immediately a trigger event following a trigger event. For the probability density function P physically one expects that $P(\Delta N_{\mathrm{Gated}} + 1) = P(\Delta N_{\mathrm{Gated}}) \cdot (1 - p)$ for some constant parameter p, i.e. the occurrence of one more non-trigger beam particle is always $(1 - p)$ times less likely. There is only one probability density function solution satisfying this recursion, which is the geometric distribution with parameter p: $P(\Delta N_{\mathrm{Gated}}) = p \cdot (1 - p)^{\Delta N_{\mathrm{Gated}}}$. As for this probability density function $P(0) = p$ holds, the we infer that $p_{\mathrm{Trig}} = p$.

The parameter p can be determined from the data by fitting an exponential function to the measured distribution of $\Delta N_{\mathrm{Gated}}$. This is done separately for the wide V_z-cut and for the gas V_z-cut as is shown in Figure 17, and then the latter trigger probability was subtracted from the former one after a scaling by the ratio of the V_z window size of the wide V_z-cut and the gas V_z-cut. Thus, the trigger probability is also corrected for the non-target contamination. The resulting trigger cross-section is $\sigma_{\mathrm{Trig}} = 5.643\,\mathrm{b}$.

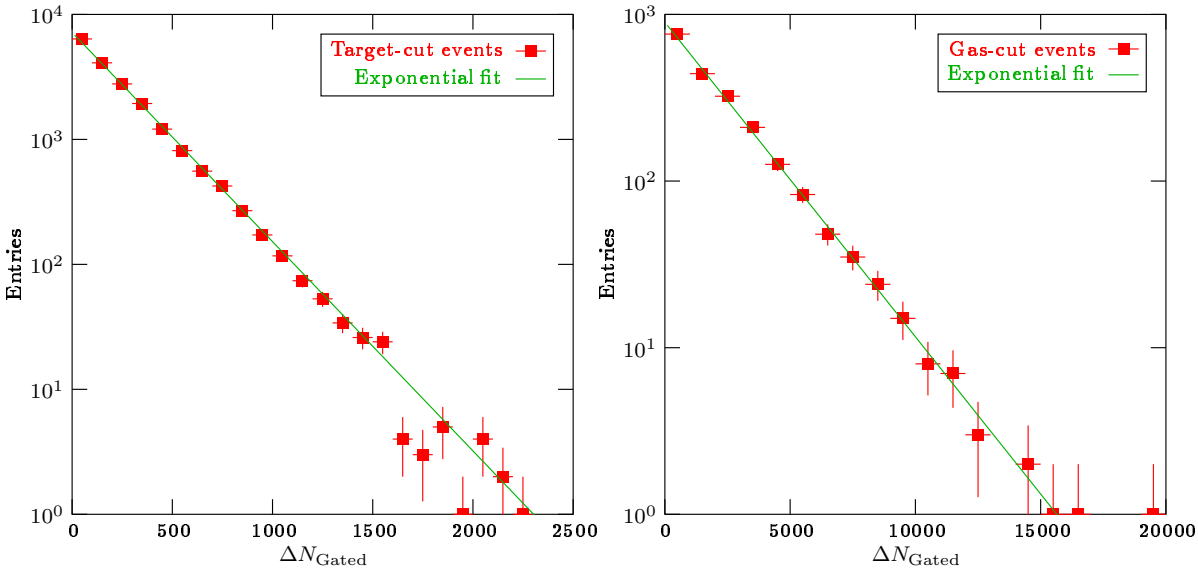

Figure 17: Measurement of trigger probability.

After the discussed procedures, the correspondence

$$E_{\mathrm{VCAL}} \mapsto \int_0^{E_{\mathrm{VCAL}}} \frac{1}{\sigma_{\mathrm{Inel}}} \frac{\mathrm{d}\sigma(E'_{\mathrm{VCAL}})}{\mathrm{d}E'_{\mathrm{VCAL}}}\,\mathrm{d}E'_{\mathrm{VCAL}}$$

of the VCAL energy (understood in the scale of the reference run) and the event centrality can be calculated, thus the desired event centrality regions may be selected via VCAL energy windows. The conversion between the VCAL energy (understood in the scale of the reference run 1468) and event centrality is listed in Table 2 for some centrality values.

For drawing physical conclusions, the average value of certain collision parameters are also needed in the used centrality windows, which may be determined by geometric Monte Carlo models (see [43]). The collision parameters of interest are the number of

$\sigma/\sigma_{\mathrm{Inel}}$	$E_{\mathrm{VCAL}}/E_{\mathrm{Beam}}$	
0%	0.000	
5%	0.280	($\uparrow$ central)
12.5%	0.452	
23.5%	0.659	
33.5%	0.799	($\downarrow$ peripheral)
43.5%	0.901	
78.5%	1.150	($\leftarrow$ the trigger centrality)

Table 2: Conversion between VCAL energy (run 1468) and event centrality.

participant nucleons[8] N_P, the number of wounded nucleons[9] N_W, the number of binary collisions[10] N_{BC}, and the impact parameter[11] b. The utilized geometric Monte Carlo model was VENUS-4.12 (see [65]).

In order to imitate the experimental situation precisely in the Monte Carlo simulation, we introduced an accurate model of the VCAL: the model takes into account all known physical effects, except for the nucleus fragmentation, as very little is known about this. Namely, the VCAL model was set up from the following ingredients.

1. Spectator nucleons were defined by those VENUS nucleons, which had smaller momentum than $0.270\,\mathrm{GeV/c}$ in the rest frame of its mother nucleus.

2. Momentum of the spectator nucleons were smeared by the Fermi motion, as VENUS does not take Fermi motion into account.

3. All nucleons were tracked down in the magnetic field to the collimator of the VCAL, located $25\,\mathrm{m}$ downstream of the target foil. The same collimator window opening was assumed as in the measurement: $-5\,\mathrm{cm} \leq x \leq 38\,\mathrm{cm}$, $-5\,\mathrm{cm} \leq y \leq 5\,\mathrm{cm}$.

4. Nucleons accepted by the collimator were assumed to generate a response of the form:

$$(\text{non-uniformity function}) \cdot (\text{energy of the particle}),$$

[8]Participant nucleon: nucleon which went through at least one scattering.
[9]Wounded nucleon: nucleon which went through at least one inelastic scattering.
[10]Binary collision: an inelastic nucleon-nucleon collision.
[11]Impact parameter: distance of the centers of the nuclei in the transverse plane.

where the parameterization of the non-uniformity function is

$$\frac{E_{\mathrm{VCAL}}(x,y)}{E_{\mathrm{Input}}} = 2.305 - \frac{1.385}{1+\exp\left(\left(\sqrt{x^2+y^2}-21.66\,\mathrm{cm}\right)/7.52\,\mathrm{cm}\right)},$$

see [52].

5. These values for the accepted nucleons were summed up for the event.

6. The summed detector signal was smeared by the detector resolution

$$\sigma(E)/E = 0.03 + 2.0/\sqrt{E/1\,\mathrm{GeV}},$$

see [48, 52, 53].

The centrality selection of the VENUS events was performed similarly to the experimental data, by using the simulated VCAL energy signal. However, an important difference is that the VENUS total cross-section σ_{VENUS} was used for the trigger cross-section σ_{Trig}, furthermore also σ_{VENUS} was used for the total inelastic cross-section σ_{Inel} in the centrality determination formula. In this case, the VENUS total cross section cancels in the centrality determination formula. Using the obtained conversion function between VCAL energy and centrality, the mean values of the collision parameters were calculated in the 6 standard centrality bin of NA49, by using $100\,\mathrm{k}$ VENUS events. Statistical errors are negligible (0.1%). The systematic errors, caused by the details of the VCAL simulation was studied by switching on/off the various ingredients of the detector model (Fermi motion, non-uniformity, energy resolution). The systematic errors caused by these effects turned to be of the order of the statistical errors (0.1%), therefore they are negligible. The systematic errors originating from the weak knowledge of the total inelastic cross-section was also investigated by using the $\sigma_{\mathrm{Inel}} = 7.15\,\mathrm{b}$ experimental value instead of $\sigma_{\mathrm{Inel}} = \sigma_{\mathrm{VENUS}}$. This systematic error, caused by the cross-section change turned out to be a larger effect (up to 6%).

For the investigation of systematic errors caused by the weak knowledge on the total inelastic cross-section, the VENUS total cross-section had to be also determined from the VENUS data. This is done by the following probability theory argument. Let $(b,r) \mapsto \rho(b,r)$ be a probability density function over the set $[0,b_{\mathrm{max}}] \times \{0,1\}$, where b_{max} is a positive real number. A value $b \in [0,b_{\mathrm{max}}]$ represents an impact parameter value between 0 and a maximal impact parameter b_{max}, while r is a Boolean variable $r \in \{0,1\}$ determining that whether a reaction happened or not, thus a pair $(b,r) \in$

$[0, b_{\max}] \times \{0, 1\}$ represents an impact parameter value together with a flag determining the occurrence of a reaction. We shall interpret $(b, r) \mapsto \rho(b, r)$ as the probability density function of reaction occurrence/not occurrence in collision with given impact parameter. By construction, we have $\sum_{r=0}^{1} \int_0^{b_{\max}} \rho(b, r)\, \mathrm{d}b = 1$. The probability density function $b \mapsto \rho_{\mathrm{Beam}}(b)$ over $[0, b_{\max}]$ defined by $\rho_{\mathrm{Beam}}(b) := \rho(b, 0) + \rho(b, 1)$ corresponds to the beam impact parameter distribution (i.e. beam profile in the impact parameter variable), as it is not sensitive to the occurrence of a reaction. Naturally, VENUS assumes homogeneous beam profile. A homogeneous cylindrical beam profile, viewed in polar coordinates (i.e. in impact parameter variable) corresponds to the probability density function $b \mapsto \frac{2 \cdot b}{b_{\max}^2} \cdot \chi_{[0, b_{\max}]}(b)$, due to simple integral substitution (as the Jacobi determinant of changing variables from Descartes coordinates to polar coordinates is proportional to the radius). The total cross-section, defined as the useful beam cross-section in the limit of infinite beam size, can be calculated via the formula $\sigma_{\mathrm{VENUS}} = \lim_{b_{\max} \to \infty} \pi b_{\max}^2 \cdot \int_0^{b_{\max}} \rho(b, 1)\, \mathrm{d}b$. However, by simply histograming the impact parameter b from the VENUS events, one only can determine the conditional probability density function $\rho(b|1) = \rho(b, 1) \Big/ \int_0^{b_{\max}} \rho(b', 1)\, \mathrm{d}b'$, as the events when reactions do not happen are not stored by VENUS. Therefore, we are lacking a proper normalization. This normalization, however, can be obtained by using the knowledge that a reaction always happens at low impact parameter values, i.e. $\rho(b, 1) \approx \rho_{\mathrm{Beam}}(b)$ when $b \approx 0$. In other words: the nuclear profile function $b \mapsto \rho(1|b) = \rho(b, 1) / \rho_{\mathrm{Beam}}(b)$ starts from 1 in the $b = 0$ limit (or at the small b limit). Therefore, by scaling our b histogram to the $b \mapsto \frac{2 \cdot b}{b_{\max}^2} \cdot \chi_{[0, b_{\max}]}(b)$ beam profile probability density function at small impact parameter values via fitting, one can obtain the desired probability density function $b \mapsto \rho(b, 1)$, needed for the cross-section calculation. The fitting procedure is shown in Figure 18. The resulting cross-section is $\sigma_{\mathrm{VENUS}} = 7.347\,\mathrm{b}$.

In the non peripheral region (0-33.5% centrality interval), the mean values of the collision parameters can simply be calculated by statistical averaging, and the mentioned systematic studies can be performed. However, in the peripheral regions (33.5-80% centrality interval) an other effect also sets on: the S3 trigger does not behave like a sharp cut in the VCAL energy, neither in the impact parameter. As the S3 trigger can not be modelled accurately on the microscopic level, a semi-empiric approach was developed for the peripheral region. The method is based on the idea of taking the correspondence of the VCAL energy and the collision parameters from the VENUS simulation, and the VCAL probability density function, needed for the averaging, should be taken from measurement to avoid the need for a precise model for the S3 trigger.

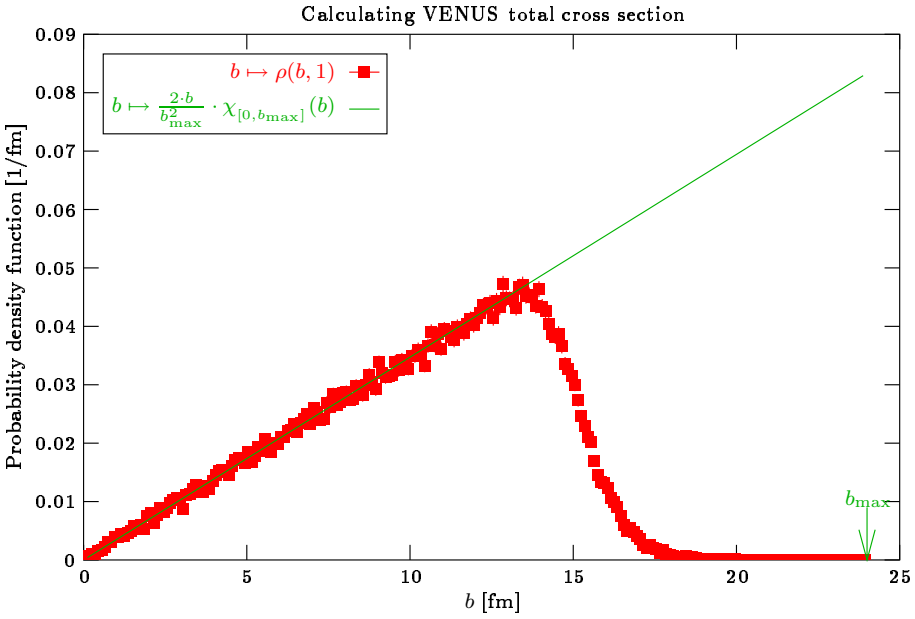

Figure 18: Measurement of VENUS total cross section.

As the VCAL energy scale is lacking an accurate absolute calibration, the empiric and VENUS VCAL energy scales can not be directly matched. The empiric scale has to be cross calibrated with the VENUS VCAL scale. This is done by recording the empiric VCAL energy differential cross-section, by recording the VENUS VCAL energy differential cross section, by assuming an unknown offset and amplification correction parameter in the empiric VCAL scale, and by fitting the linearly interpolated empiric curve to the VENUS curve in the non-peripheral region with the constraint of area conservation (thus, the trigger cross-section is not distorted by the calibration). The result of this fitting method is shown in Figure 19.

The resulting mean values and standard deviations of collision parameters are listed in Table 7 in Appendix C. The values after the $\pm$ signs are the systematic errors caused by the error of the total inelastic cross-section. All the other errors are negligible. For the centralities below 33.5%, simple statistical averaging was used, while for the regions above this threshold (i.e. in the peripheral region), the semi-empiric averaging method was used, as discussed, to take the trigger distortions into account.

A summary plot on centrality selection for Pb+Pb events is shown in Figure 20. The calculated average collision parameters are also shown on the figure. A summary table on the available event statistics after cuts in the used centrality bins is listed in Table 3.

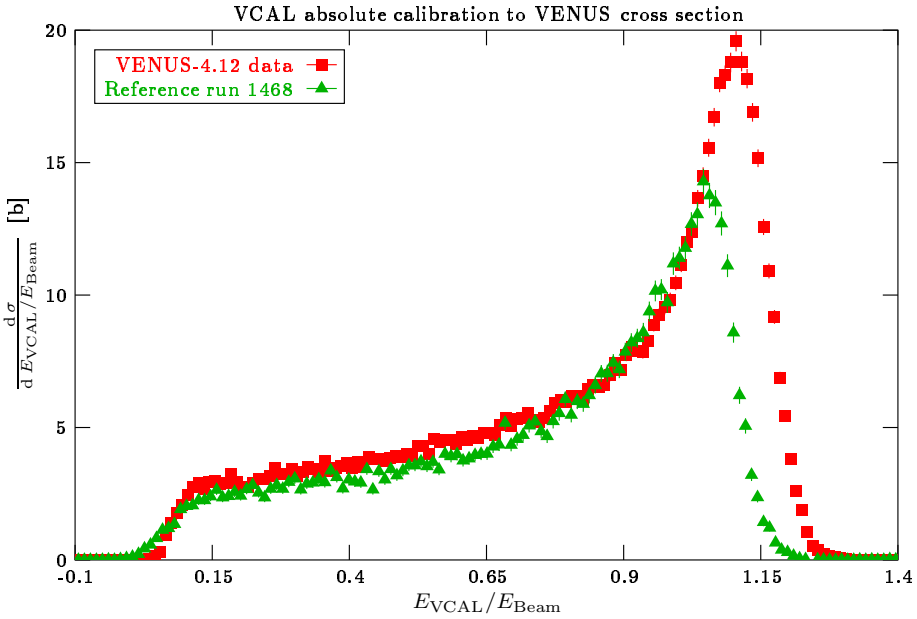

Figure 19: Cross calibration of empiric and VENUS VCAL energy scale.

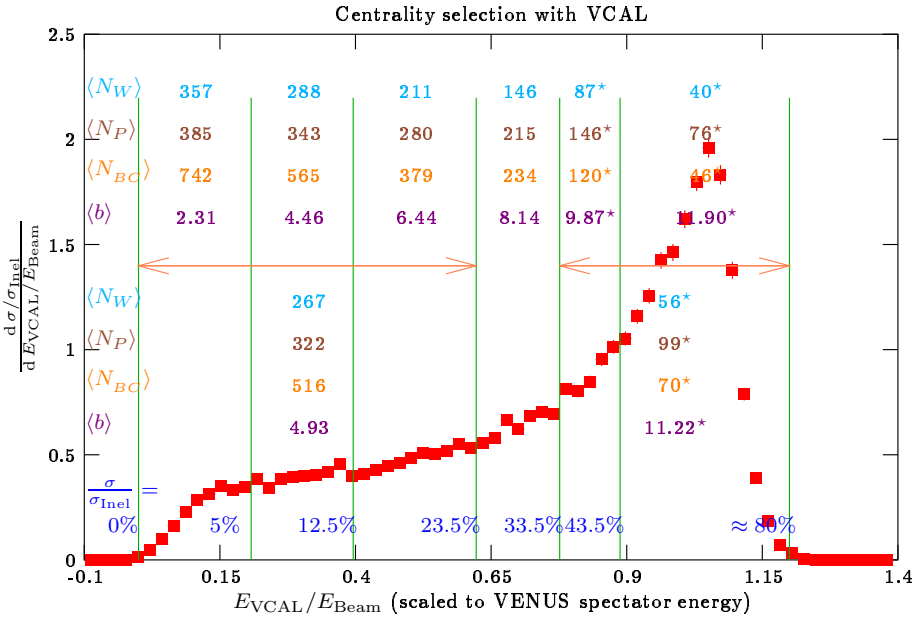

Figure 20: Centrality selection by VCAL energy together with the mean values of collision parameters. *: These values are semi-empiric averages, calculated on the full minimum-bias dataset.

3.2 p+Pb and p+p Events

3.2.1 Main-Vertex Longitudinal Position Cut

The p+Pb and p+p events are largely different from the Pb+Pb events, as their total multiplicity is much smaller. Therefore the V_z resolution is worse than for Pb+Pb

Centrality	Events
0-5%	830 k
12.5-23.5%	1.4 M
33.5-80%	200 k

Table 3: Available Pb+Pb statistics in the used centrality bins.

events. The target setups are also more sophisticated: in the p+Pb case, the target foil is contained within the CD, while in the p+p case, the target is a 20 cm long liquid hydrogen cylinder.

The non-target events, just as in the Pb+Pb case, are suppressed by V_z cuts. For the estimation of non-target contamination, also 'empty-target' events were recorded, which delivers the yield of the extra events, not being beam+target collisions. These were recorded with unchanged setup, only the target material was removed from the beamline (target containers etc. were left untouched).

The V_z distribution for p+Pb events, together with the empty-target contribution and the applied V_z-cut is shown in Figure 21. The same plot for p+p is shown in Figure 22. A detailed study of p+p events can be found in [11], while for a situation like the p+Pb reaction is worked out in [12].

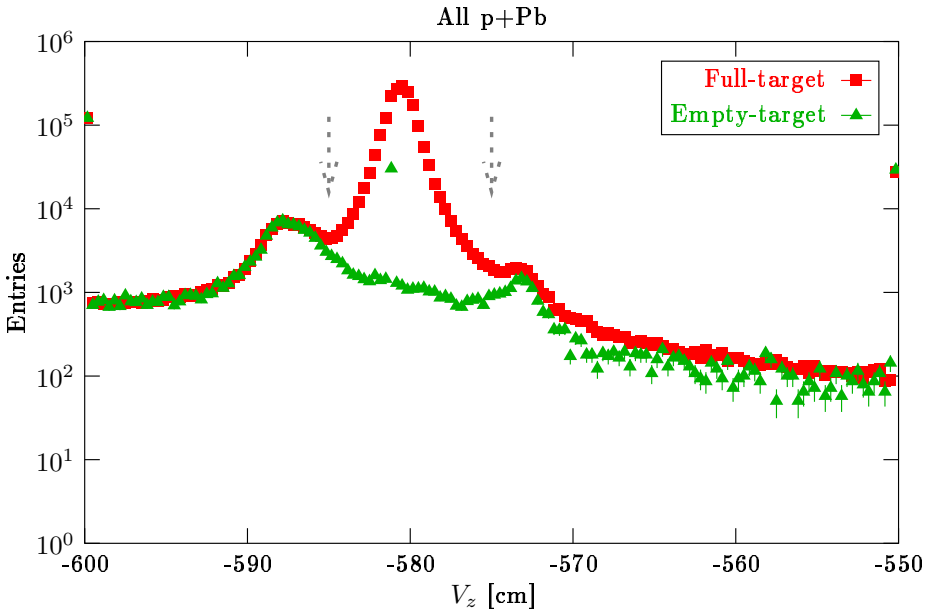

Figure 21: Distribution of main-vertex longitudinal position in p+Pb events.

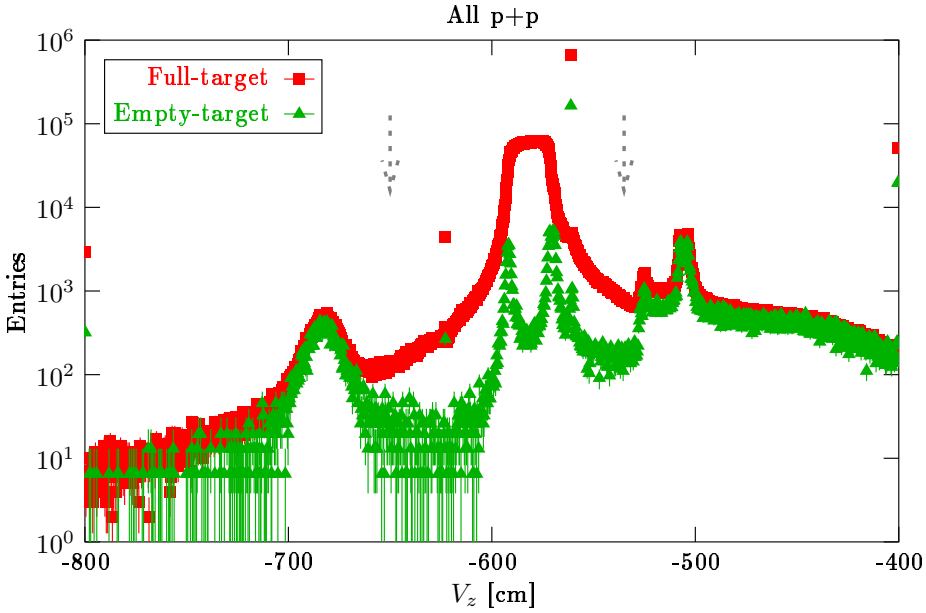

Figure 22: Distribution of main-vertex longitudinal position in p+p events.

3.2.2 Centrality Selection

In p+p reactions, no centrality differentiation is done. In p+Pb reactions, the number of slow particles (grey protons), measured by the CD detector, is used to classify events with respect to centrality. For a detailed study on CD, we refer to [55]. The CD response distribution is shown in Figure 23 for p+Pb minimum-bias events.

The CD response can be used to differentiate events by centrality just like the VCAL for Pb+Pb events. However, due to the limited statistics of our p+Pb events, we use the full event sample, which is a mixture of events, recorded by CD $\geq$ 1, 3, 7 trigger criteria. For drawing physical conclusions, the calculation of the average collision parameters via geometric Monte-Carlo models, just like in the Pb+Pb case, is essential. As our event sample was recorded with varied trigger CD threshold, the average values were calculated by a similar semi-empiric approach as in the case of the Pb+Pb(Peripheral) events: the probability density function of the CD response was taken from measurement, while the mapping from the CD response to various collision parameters was taken from the VENUS-based simulation, for the averaging. This also helps to take the trigger bias into account without microscopic simulation, just as in the Pb+Pb(Peripheral) case. The necessary mapping is also presented in [22]. The resulting average values are listed in Table 8 in Appendix C. A summary table on the

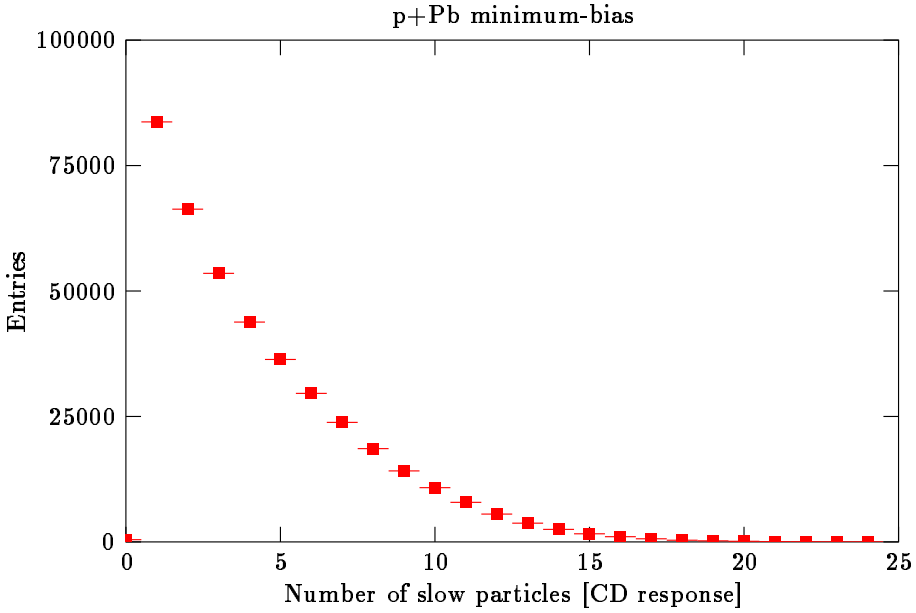

Figure 23: Distribution of the CD response for p+Pb minimum-bias events.

available p+Pb and p+p event statistics after cuts is listed in Table 4.

Reaction	Events
p+Pb	1.8 M
p+p	4.8 M

Table 4: Available p+Pb and p+p statistics.

4 Track Selection

The experiment NA49 originally was designed and optimized for the tracking of particles in the transverse momentum domain below $2\,\mathrm{GeV/c}$. However, due to the interesting experimental results on the particle suppression at high transverse momenta around midrapidity[12] – discovered at the PHENIX, STAR, PHOBOS and BRAHMS collider experiments at the RHIC accelerator at $200\,\mathrm{GeV}$ nucleon-nucleon collision energy –, the transverse momentum region above $2\,\mathrm{GeV/c}$ became also interesting for our experiment. The physical question naturally arises: does the particle suppression at high transverse momentum show a strong energy dependence, when varying the nucleon-nucleon collision energy from $200\,\mathrm{GeV}$ to $17.3\,\mathrm{GeV}$?

We shall parameterize the particle momentum space in a form of cylindric coordinates in the nucleon-nucleon center of mass system, where the cylinder axis is chosen to be the collision axis. The longitudinal coordinates may be the longitudinal momentum $p_{_L}$, the Feynman-x variable $x_{_F}$, the polar angle θ between the longitudinal axis and the particle momentum direction in the longitudinal plane, the longitudinal rapidity (or simply: rapidity) y, or the longitudinal pseudorapidity (or simply: pseudorapidity) η. Mostly, we shall use the y variable. The transverse coordinates may be the transverse momentum $p_{_T}$, or the transverse energy (synonym: transverse mass) $E_{_T}$. Mostly, we shall use the $p_{_T}$ variable. The remaining degrees of freedom is the azimuthal coordinate φ, which is irrelevant for the single-particle spectra: the particle production is axially symmetric. For overview on the used conventions on these kinematic variables, see Appendix A.

4.1 Tracks without Selection

The main problem of midrapidity high transverse momentum tracking in NA49 is that the experiment is a fixed target experiment, not a collider experimental setup. In a collider experiment, the midrapidity high transverse momentum tracking would not need much further fine tuning: due to simple kinematic reasons (see Appendix A), the track density in a collider experiment is minimal around midrapidity, whereas in a fixed-target experiment, the track density stays high at midrapidity, and the tracks tend to cross each-other, which makes the tracking procedure more difficult.

In our experiment, above about $p_{_T} \geq 2\,\mathrm{GeV/c}$, the majority of tracks turn out to

[12] In the nucleon-nucleon center of mass system the purely transversal particle momenta are called midrapidity (particle momenta with zero longitudinal rapidity).

be fake. This is demonstrated by Figure 24. It is seen that the distribution has a large, power-law like tail at large values. However, it is known that at SPS energies the distribution of transverse momentum follows a rapid, approximately exponential, fall-off property. Therefore, it can be said that the track yield at large transverse momentum is dominated by fake tracks. One reason is, that the tracks of secondary particles and the split tracks tend to fake high transverse momentum tracks, when the track collection erroneously matches a straight MTPC track piece to some residual points in VTPC1 or VTPC2. A further reason is the high track density of the heavy-ion events (a central Pb+Pb event contains about 1500 reconstructed tracks), which makes the situation worse for the Pb+Pb events. Therefore, efforts were made in the past to develop such track selection methods, which reduces this high fake rate at high transverse momentum in our experiment (see e.g. [61]), however, these efforts proved not to be satisfactory. The aim of this section is to investigate the precise origin of these tracks, and to show a track selection criterion, which cleans the track sample. (Detailed discussion can also be found in [44].)

A self-suggesting idea would be to look at the ratio of the measured spacepoints (called points) and predicted spacepoints (called potential points – or simply: potpoints) of these tracks (the prediction is done by extrapolating a track with the fitted momentum from the target). The point/potpoint ratio should be close to 1 for an ideally reconstructed track. An other idea could be to look at the fit impact parameter coordinates B_x, B_y.[13] B_x and B_y should be close to 0 for an ideally reconstructed track. The distribution of the measured point per potential point quotient is shown in Figure 25, whereas the B_x, B_y distributions are shown in Figure 26, 27 – for high transverse momentum particles.

The point/potpoint spectrum suggests a threshold: a track can be considered to be badly fitted, if this quotient is under e.g. 0.6. A possible choice would be to reject these tracks directly. However, this cut would result in an uncontrolled tracking acceptance[14] and reconstruction efficiency, which may depend on many unknown event or track parameters (e.g. event multiplicity etc.). To avoid this situation, cuts are not applied on the track quality quantities directly. Instead, the strategy was investigated if there exists a momentum space region, where the fraction of badly fitted tracks (i.e. tracks having point/potpoint ratio worse than 0.6) is low. Then, by an explicit

[13]The differences between the main-vertex x, y coordinates and the x, y coordinates of the track intersection point with the target plane are called the fit impact parameter x, y coordinates of the track.

[14]The momentum space region from where detectable tracks originate is called the acceptance.

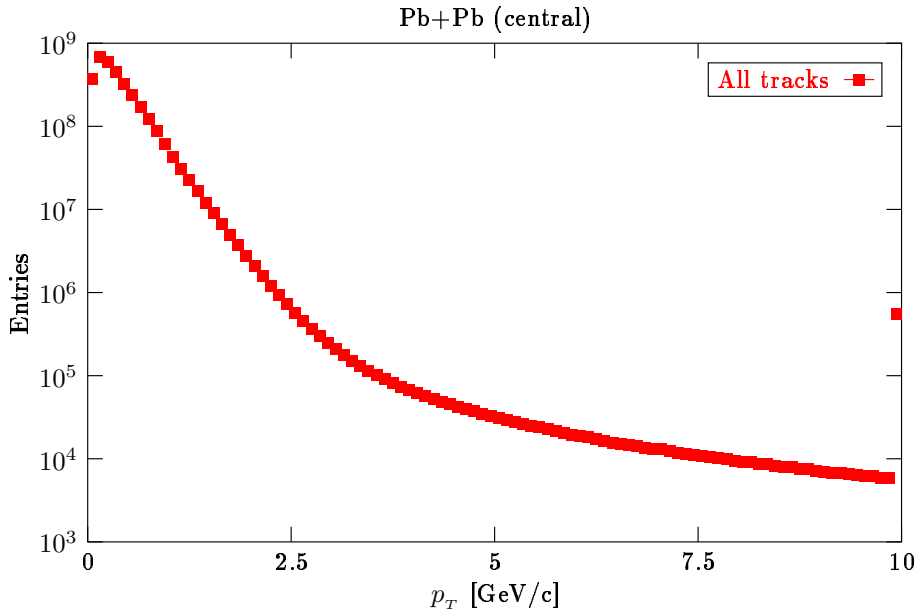

Figure 24: Transverse momentum distribution – all tracks.

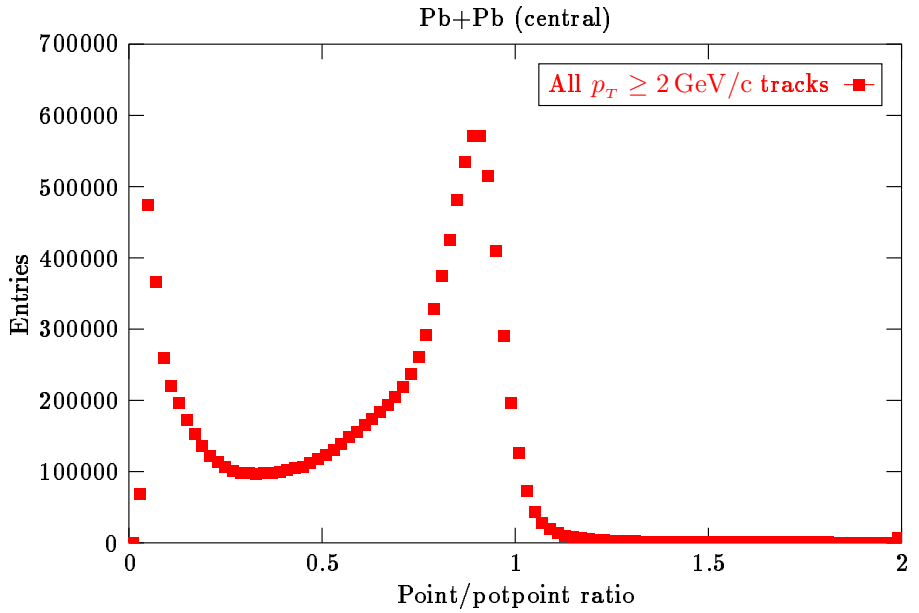

Figure 25: Point/potpoint distribution of $p_T \geq 2\,\mathrm{GeV/c}$ tracks.

selection of this clean momentum space region by a 3 dimensional momentum space cut, one would directly control the acceptance, and the reconstruction efficiency could be guaranteed to be close to 1. Therefore, a 3 dimensional differential study of the

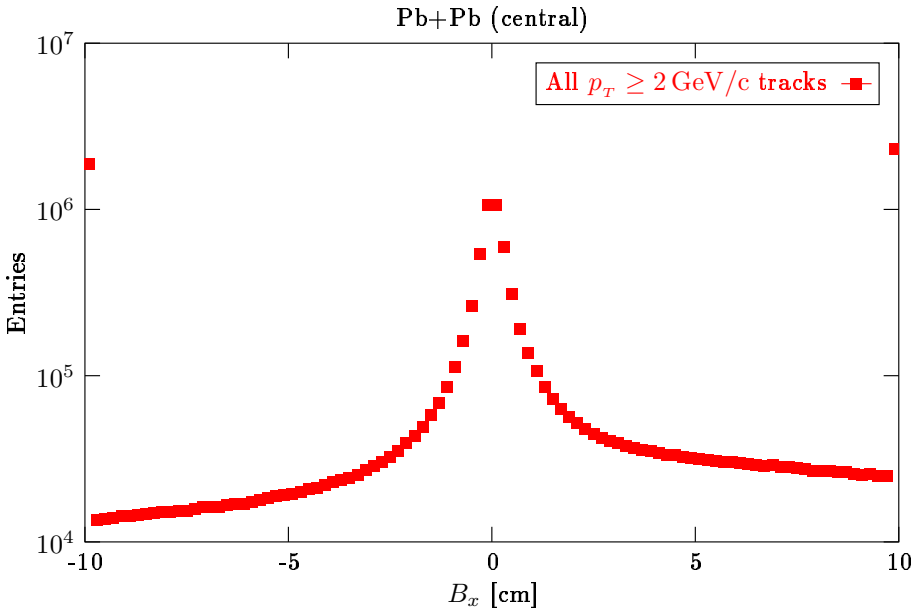

Figure 26: B_x distribution of $p_T \geq 2\,\mathrm{GeV/c}$ tracks.

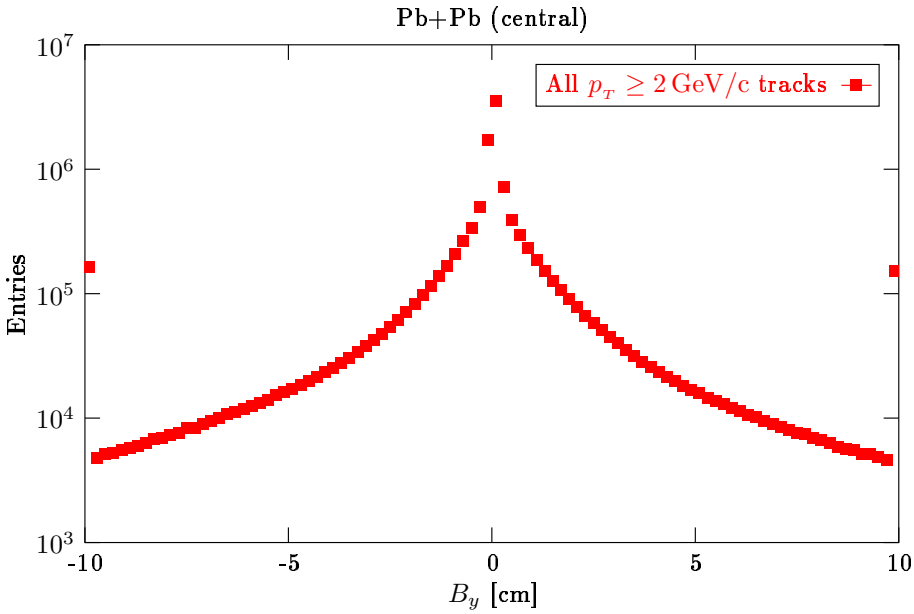

Figure 27: B_y distribution of $p_T \geq 2\,\mathrm{GeV/c}$ tracks.

tracks quality as a function of momentum space is needed.

In our momentum space study, we shall parameterize track momentum by rapidity y (with different particle mass hypotheses: assuming $\pi^{\pm}$, p and $K^{\pm}$ masses), charge-

reflected azimuth ϕ, and transverse momentum p_T. The charge-reflected azimuth is defined as follows: if the reconstructed momentum vector in the laboratory system of the given track is (p_x, p_y, p_z), then the charge-reflected azimuth is defined to be the azimuth of the vector (stdmsgn$\cdot$chargesgn$\cdot p_x, p_y, p_z$), where 'stdmsgn' is the sign of the magnetic field direction (± 1), 'chargesgn' is the sign of the charge of the particle (± 1). This charge-reflection allows us to treat the two different magnetic field directions and the two charge signs in a uniform way, due to the x-reflection symmetry of the detector. (The detector has an x-reflection symmetric, however it does not have an y-reflection symmetry. For our purposes, the x-reflection symmetry is sufficient, as x happens to be the particular transverse direction which is perpendicular to the magnetic field.)

We shall define the fraction of bad tracks in a given momentum space bin to be the fraction of point/potpoint< 0.6 tracks. The fraction of bad tracks as a function of momentum space is shown in Figure 28. (This is an example plot, where y is calculated with $\pi^{\pm}$ mass hypothesis. The survey was also performed with p and $K^{\pm}$ mass hypothesis.) The number of potential points is shown as a function of momentum by the color map. This was calculated from the geometry of the detector. The fraction of bad tracks is shown by the scaled boxes (the box size range corresponds to the fraction range from 0 to 1). The clean region of momentum space can be identified: those regions, which have potpoints≥ 50, and are not populated by the boxes, showing contamination of the track sample by badly fitted tracks. It is seen that the only clean regions are certain low $|\phi|$ domains with $p_T \leq 2\,\mathrm{GeV/c}$, no clean high p_T region is revealed. These plots were obtained by populating the momentum space with the tracks of our full Pb+Pb database.

Due to the used parameterization, the tracks which do not cross the plane defined by the beamline and the magnetic field direction (right-side tracks) can be found in the middle of the figures (low $|\phi|$ regions), while the tracks which do cross the given plane (wrong-side tracks) populate the left and right ends of the figures. Due to the nature of the track fitting procedure, the wrong-side tracks are more likely to generate fake tracks (however, no difference can be seen between right-side and wrong-side, yet, in Figure 28).

4.2 Rejection of Discontinuous Tracks + Momentum Space Cut

As the 3 dimensional momentum space survey shows, the high transverse momentum region is populated by misfitted tracks, even in the interior of the acceptance (i.e. far

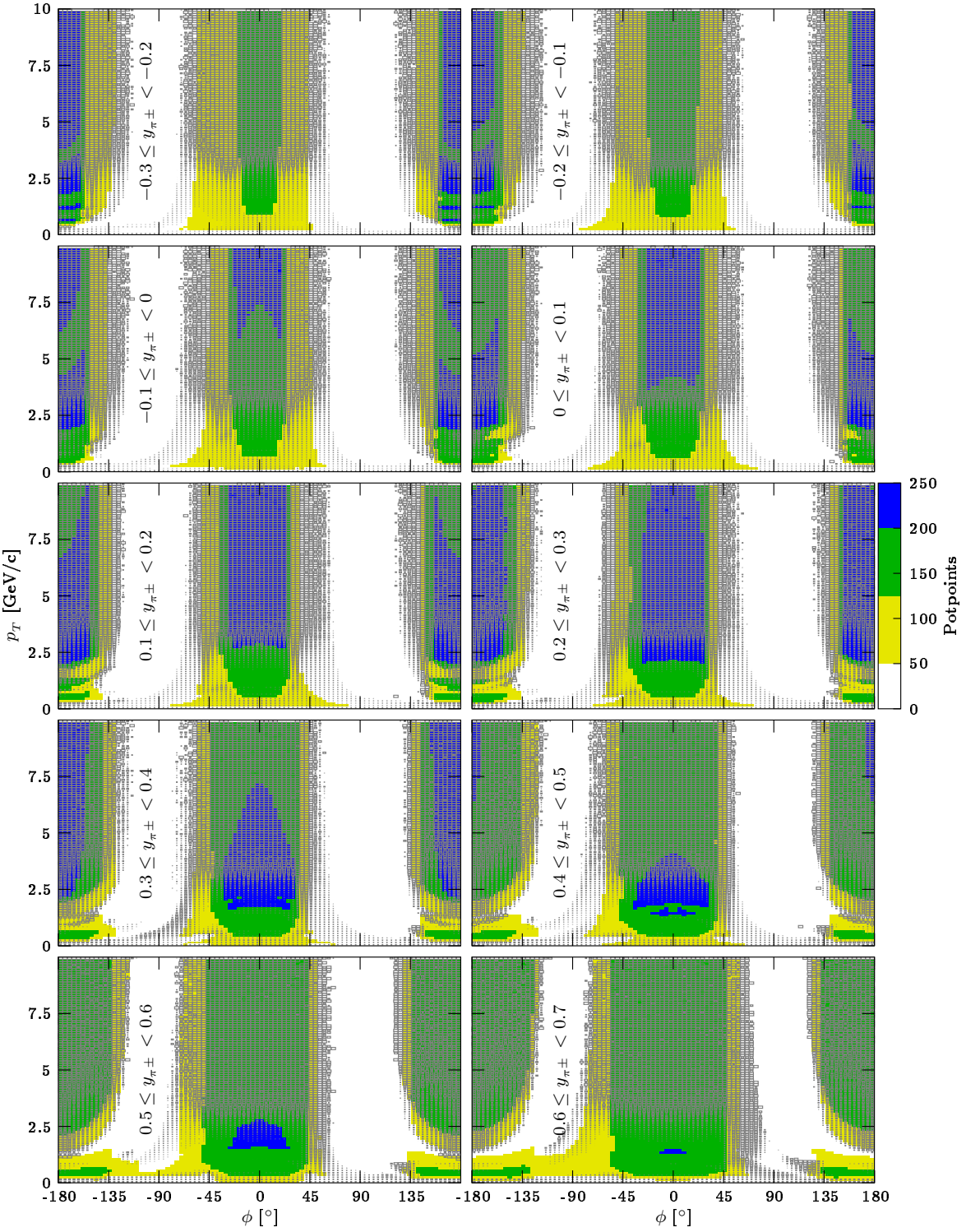

Figure 28: Fraction of bad tracks (scaled boxes) as a function of momentum – no previous track selection. (Box size range: 0 ≤fraction≤ 1.)

from the edges). The origin of these fake tracks inside the acceptance is be investigated below.

Each track may consist of three disconnected components: a VTPC1 piece, a VTPC2 piece and an MTPC piece. Eyescan results showed that most of the high transverse momentum (i.e. fake) tracks have the property of possessing a remarkable amount of potential points in a given TPC detector (i.e. VTPC1 or VTPC2 or MTPC), but possessing *zero* measured points there. This means that most of the high transverse momentum (i.e. fake) tracks are such, that at least one of its TPC segments, which should have been detected if it was a real particle trace, are missing. We call these discontinuous tracks. Obviously, these tracks cannot be real particle trajectories, rather they are such track candidates, which are composed of mismatched MTPC and VTPC1, VTPC2 pieces. Mostly, they consist of large MTPC pieces, matched to some residual points either in VTPC1 or in VTPC2, thus leading to *zero* measured points in the other VTPC.

The basic idea of our track sample cleaning method was to first reject these obviously bad tracks candidates. The cut was formalized by rejecting tracks with $p_T \leq 2.2\,\mathrm{GeV/c}$ if the track has at least 40 potential points in a TPC detector, but has 0 measured points there. For $p_T > 2.2\,\mathrm{GeV/c}$, a slightly stricter criterion was used: the track was rejected if it has 10 potential points in a TPC detector, but has 0 measured points there. The choice of these particular cut values were optimized via Monte Carlo simulations by maximizing tracking efficiency around low $|\phi|$ values.

After this cleaning procedure, the fraction of bad tracks as a function of momentum space is shown in Figure 29. (This is an example plot, where y is calculated with $\pi^{\pm}$ mass hypothesis. The survey was also performed with p and $K^{\pm}$ mass hypothesis.) A clean momentum space region, which is free of bad track candidates, can be identified around low $|\phi|$ values, which extends up to high transverse momenta. By selecting this clean momentum space region, one obtains a clean track sample, where the fake track contamination is low, and the tracking efficiency is high. The momentum space cut is done by a cut surface, which is guided by potential point isosurfaces, and is shown on the figure by the dotted lines. The ϕ distribution in an example transverse momentum slice $2.6\,\mathrm{GeV/c} \leq p_T < 2.7\,\mathrm{GeV/c}$ is shown in Figure 30.

The figures show that, after the rejection of discontinuous tracks, the interior of the right-side acceptance is not populated by bad tracks anymore. The local azimuthal symmetry of the spectrum also holds there around low $|\phi|$ values. As the particle production is axially symmetric, the ϕ distribution should be flat in ideal case. However,

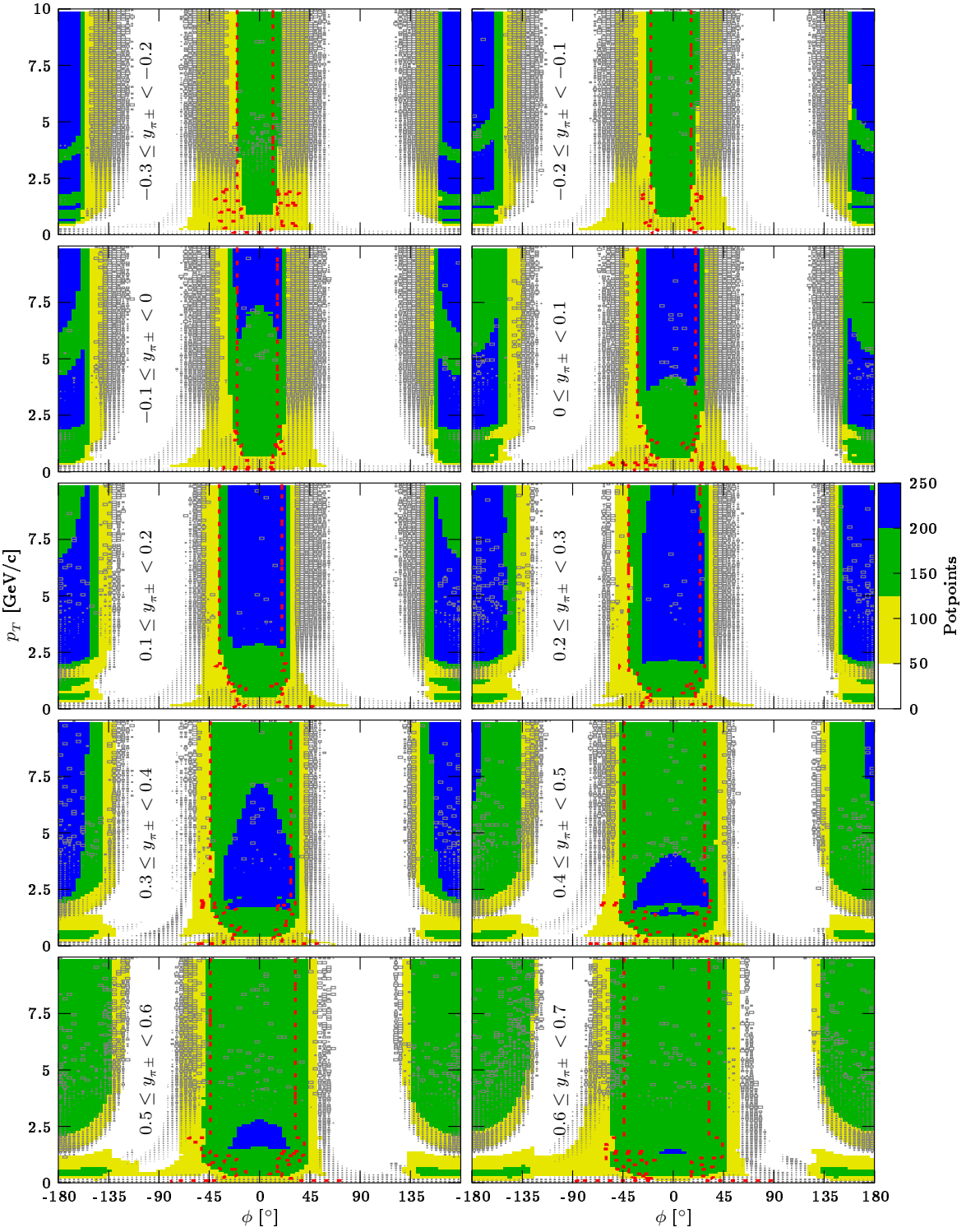

Figure 29: Fraction of bad tracks (scaled boxes), as a function of momentum – discontinuous tracks rejected. (Box size range: $0 \leq$fraction≤ 1.) Dotted line: momentum space cut.

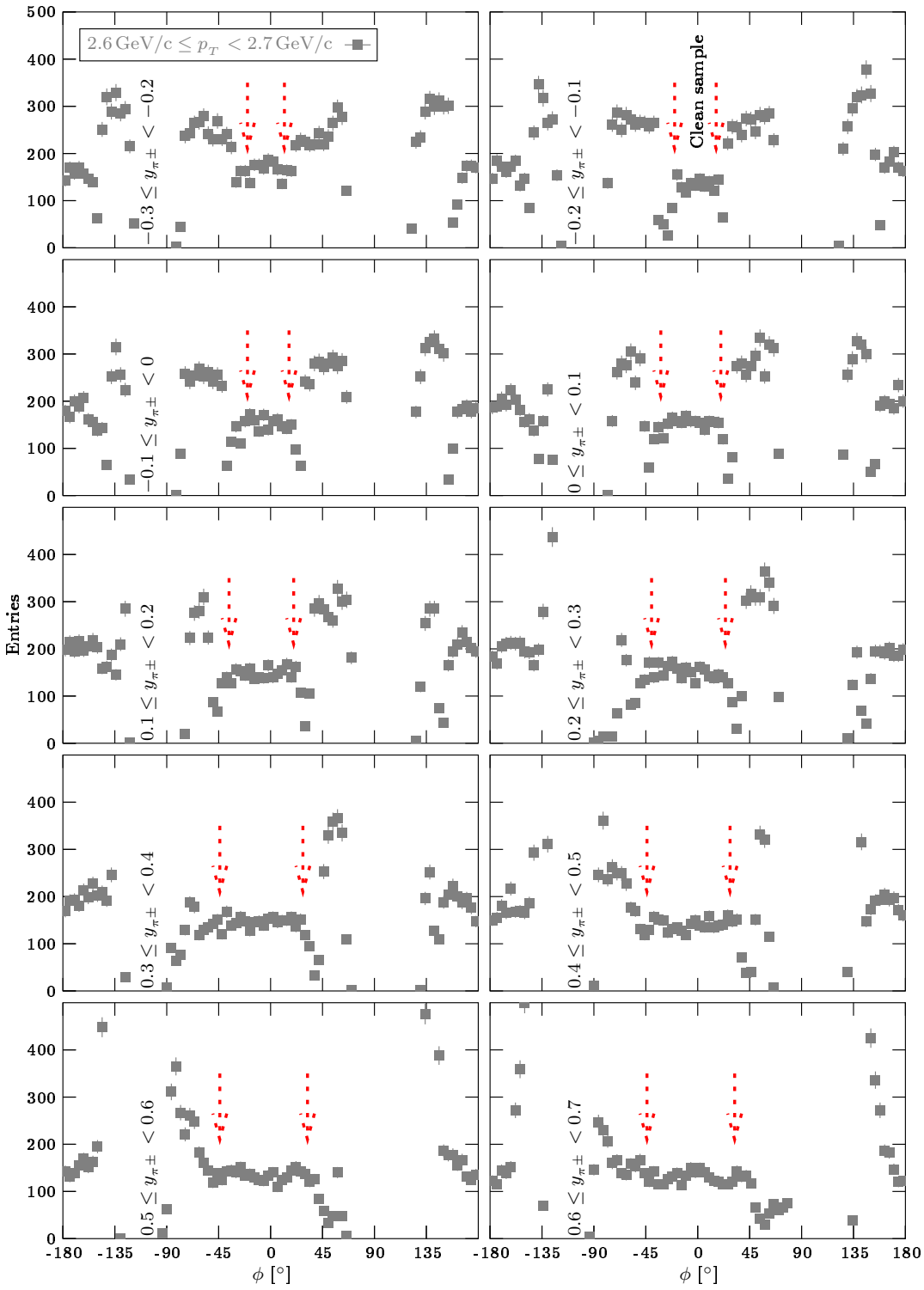

Figure 30: ϕ distribution in the 2.6 GeV/c ≤ p_T < 2.7 GeV/c slice – discontinuous tracks rejected. Dotted line: momentum space cut. (The avoiding of efficiency holes.)

as can be seen in Figure 30, this property does not extend up to higher $|\phi|$ values in the available detector acceptance due to efficiency holes and fake track contamination at the edges of the acceptance. To avoid these, the momentum space cut surface was not only guided by potential points, but the cut was more restrictive. Namely, at given (y, p_T) slice, the deviations of the ϕ distribution from the $\phi = 0^\circ$ value was watched. A ϕ scan was started from $\phi = 0^\circ$ to the $\phi < 0^\circ$ and to the $\phi \geq 0^\circ$ region, and if the value of the ϕ distribution at the given ϕ position was deviating from the $\phi = 0^\circ$ value by more than 5 standard deviations, then the momentum space cut was placed at that particular ϕ value to avoid efficiency holes and other variations in the ϕ distribution by construction. As at larger p_T-s our track statistics died out, a $\phi = \text{const}$ extrapolation was used, to extend this restriction to higher p_T-s. (The potential point isocurves at the $y = \text{const}$ slices are $\phi \approx \text{const}$ curves at $p_T \geq 2\,\text{GeV/c}$.)

For cross-checking purposes, we show some further figures about the performance of the introduced track selection method.

In Figure 31 the transverse momentum distribution is shown in a given y slice, with different ϕ cuts – here the discontinuous tracks are rejected. It is clearly seen, that the high p_T tail suddenly appears when approaching toward the border of the acceptance, i.e. at more permissive $|\phi|$ cuts. In Figure 32 the evolution of the point/potpoint distribution for high p_T tracks is shown during a similar $|\phi|$ scan.

In Figure 33 the point/potpoint and fit impact parameter coordinate distributions are shown, at given y, p_T and ϕ bin – no track cleaning and the rejection of discontinuous tracks is compared. The entries at low point/potpoint values and at large fit impact parameter values are clearly due to the discontinuous tracks. The large point loss in VTPC1 is due to the large track density. However, the track reconstruction still proves to work well.

As shall be shown in a next section, the good quality (low fakerate, high tracking efficiency) of the tracks, selected by our cuts is also confirmed by extensive Monte Carlo studies. However, it is important to note, that our cuts were fine-tuned by using real data and not Monte Carlo data, which makes the track selection method more safe and stable.

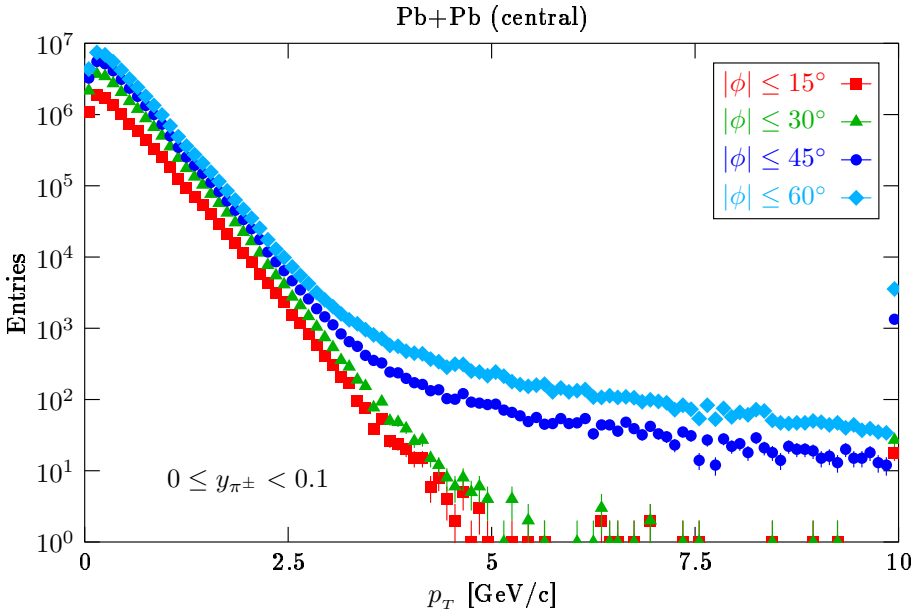

Figure 31: p_T distributions in $0 \leq y_{\pi^\pm} < 0.1$ slice, with different $|\phi|$ cuts – discontinuous tracks rejected.

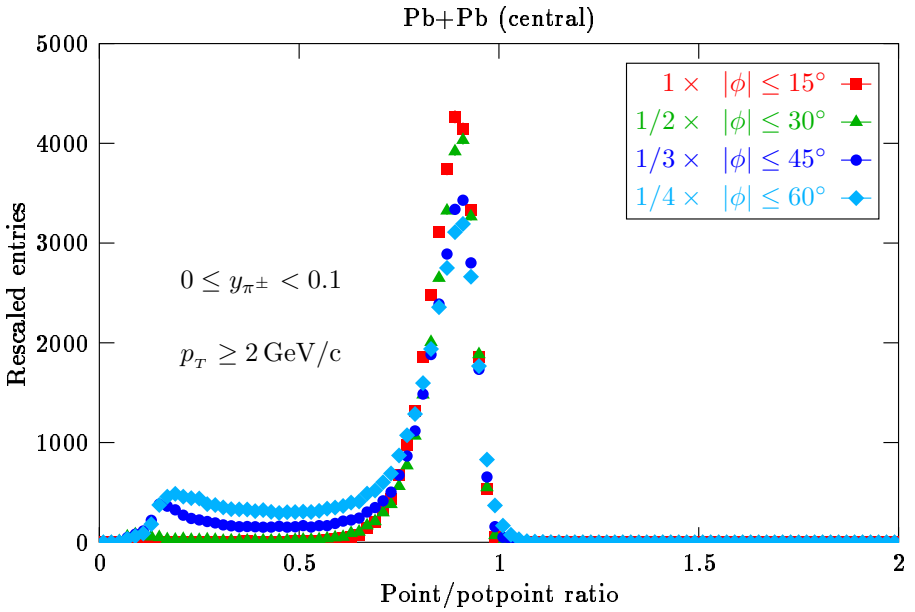

Figure 32: Point/potpoint distributions in $0 \leq y_{\pi^\pm} < 0.1$ slice for $p_T \geq 2\,\mathrm{GeV/c}$, with different $|\phi|$ cuts – discontinuous tracks rejected.

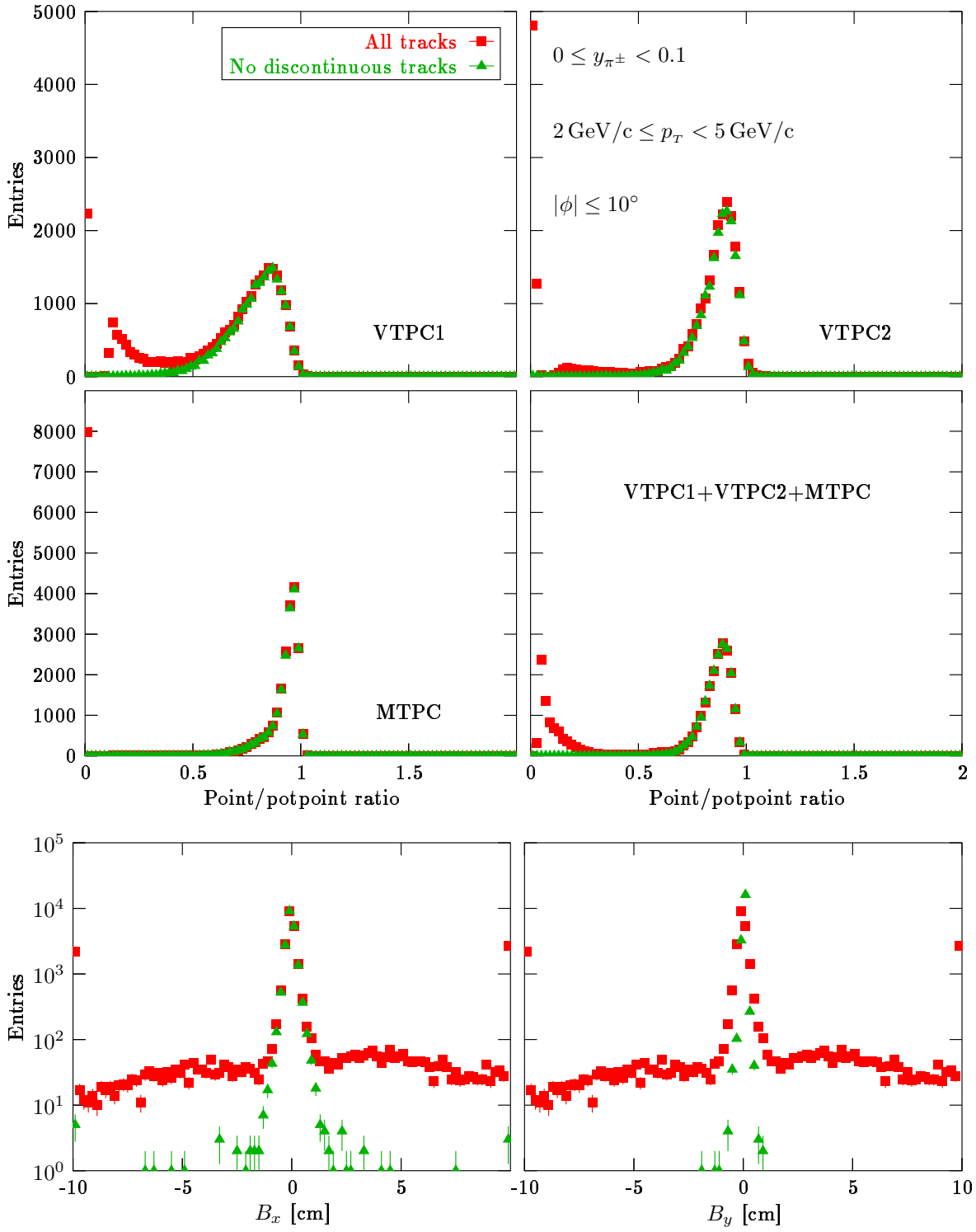

Figure 33: Point/potpoint and fit impact parameter coordinate distributions in slice $0 \leq y_{\pi^\pm} < 0.1$ and domain $2\,\mathrm{GeV/c} \leq p_T < 5\,\mathrm{GeV/c}$ and $|\phi| \leq 10°$. Two quality cuts are compared: tracks without selection and the rejection of discontinuous tracks.

5 Particle Identification

Our main goal is to measure the nucleon-nucleon collision energy dependence of the transverse momentum spectra of particles at midrapidity. As the transverse momentum spectra of the various particle species are rather different, the identification of particle types is crucial in our analysis.

The NA49 detector has two facilities for particle type identification. One is two ToF (Time of Flight) detectors after the MTPC chambers as was shown in Figure 6. These detectors measure the elapsed particle flight time in the laboratory frame from the collision instant to the arrival at the ToF walls along the particle trajectories. The track reconstruction measures the particle charge sign and momentum, furthermore the length of the tracks from the target to the ToF walls. By using the additional time information of the ToF walls, the particle velocity in the laboratory frame, and thus the particle mass can be determined, which (together with the charge sign information) allows the identification of particle type. An other possibility is to measure the specific energy loss (commonly denoted by $\frac{\mathrm{d}E}{\mathrm{d}x}$) in the TPC gas volume, characteristic to each particle trajectory. As the specific energy loss is known to depend only on the particle velocity (and not on momentum) in the rest frame of the traversed material, the $\frac{\mathrm{d}E}{\mathrm{d}x}$ information can be used indirectly for mass measurement together with the momentum information, supplied by the track reconstruction.

As the acceptance of the ToF walls do not cover the momentum space region of interest, the particle type determination shall be performed via $\frac{\mathrm{d}E}{\mathrm{d}x}$ measurement in our present analysis.

5.1 Particle Identification by Specific Energy Loss

The particle identification by $\frac{\mathrm{d}E}{\mathrm{d}x}$ is based on the knowledge that the distribution of the $\frac{\mathrm{d}E}{\mathrm{d}x}$ for a particle with given charge magnitude in a given traversed material only depends on the velocity of the particle in the rest frame of the material. This is known as the Bethe-Bloch rule, and is described in the classic literature. For reference, see e.g. [10, 29]. The most probable value[15] of the $\frac{\mathrm{d}E}{\mathrm{d}x}$ quantity for a given particle with charge number z, and velocity β relative to the speed of light (in the rest frame of the

[15] The position of the maximum of the probability density function.

traversed medium) is given by the well known Bethe-Bloch formula

$$\left(\frac{\mathrm{d}E}{\mathrm{d}x}\right)_{\substack{(\beta)\\ \text{Most prob.}}} = \frac{2\pi N r_e^2 m_e c^2 z^2}{\beta^2}\left(\ln\frac{2m_e c^2\beta^2\gamma^2(\beta)E_{\max}(\beta)}{I^2} - 2\beta^2 - \delta(\beta)\right),$$

where N is the electron density of the material, m_e is the electron mass, r_e is the classical electron radius, c is the speed of light, furthermore I is the average ionization energy of the material, $E_{\max}(\beta) = \frac{2m_e c^2\beta^2\gamma^2(\beta)}{1+2\gamma(\beta)m_e/m+(m_e/m)^2}$ is the maximum energy transfer in the ionization process, $\delta(\beta)$ describes the shadowing effects of the polarization, and $\gamma(\beta) = (1-\beta^2)^{-1/2}$ is the relativistic gamma factor, while m is the mass of the incident particle. If the relation $2\gamma m_e/m \ll 1$ holds (low-energy approximation), then the maximal energy transfer $E_{\max}(\beta) \approx 2m_e c^2\beta^2\gamma^2(\beta)$ is independent of the mass m, thus only depends on the velocity, not on momentum (indeed, this approximation holds up to about $100\,\mathrm{GeV}$ for pions). Note that if the particle momentum is p, then $\beta = \frac{p/(mc)}{\sqrt{1+(p/(mc))^2}}$ and $\beta\gamma = p/(mc)$, thus $\left(\frac{\mathrm{d}E}{\mathrm{d}x}\right)_{\text{Most prob.}}$ can be expressed purely as a function of $p/(mc)$. In fact, this is also true for the $\frac{\mathrm{d}E}{\mathrm{d}x}$ distribution: the shape of the $\frac{\mathrm{d}E}{\mathrm{d}x}$ probability density function for a particle only depends on the velocity. The Bethe-Bloch function has four important regions: at low velocities the most probable ionization energy loss decreases with growing velocity ($\frac{1}{\beta^2}$ dominates), then it reaches a minimum value (so called minimum ionization particle – MIP – region; at $p/(mc) \approx 3$), then it starts to rise again (relativistic rise range; $\ln\beta\gamma$ dominates), finally it shows a saturation (Fermi plateau) at very high speeds. Due to the fixed target setup, our particles around midrapidity are fast, therefore we cover the relativistic rising range for $\pi^\pm$, $p, \bar{p}$, $K^\pm$, while for $e^\pm$ we are already in the plateau region.

As the momentum space cut implicitly guarantees high number of spacepoints, particle identification by specific energy loss can be performed. Due to our momentum space cut, the minimal number of potential points is 40 at low transverse momentum ($p_T \leq 2\,\mathrm{GeV/c}$), while it is 80 at high transverse momentum ($p_T > 2\,\mathrm{GeV/c}$). The $\frac{\mathrm{d}E}{\mathrm{d}x}$ value, characteristic to a track, can be estimated from the $\frac{\mathrm{d}E}{\mathrm{d}x}$ samples at the detected spacepoints. However, the $\frac{\mathrm{d}E}{\mathrm{d}x}$ distribution at fixed velocity is known to follow Landau distribution, which grows until the most probable value and then decays with a $\frac{\mathrm{d}E}{\mathrm{d}x} \mapsto \left(\frac{\mathrm{d}E}{\mathrm{d}x}\right)^{-2}$ powerlaw-like tail, thus the expectation value of the $\frac{\mathrm{d}E}{\mathrm{d}x}$ distribution does not exist. Therefore, the calculation of a characteristic specific energy loss value from the available samples is not trivial. E.g. a simple statistical mean would not give a $\frac{\mathrm{d}E}{\mathrm{d}x}$ response close to the most probable value, it would also be sensitive to the number of samples. An adequate solution would be a maximum-likelihood fit to the available

sample values, which could extract an estimate for the most probable value out of the available point samples, along a given track. However, given the large number of point samples along tracks and the large number of tracks in heavy-ion events, this would have been an unbeatable computing challenge at the time of the data taking and reconstruction (1996 and 2000). Therefore, a much less CPU-intensive method was used, namely the method of truncated means. This method attaches a characteristic $\frac{\mathrm{d}E}{\mathrm{d}x}$ value to the given track from the available point samples by calculating the statistical mean value of the lower half of the samples and by applying some further corrections to them (see: [59, 60]). A typical $\frac{\mathrm{d}E}{\mathrm{d}x}$ spectrum as a function of momentum can be seen in Figure 34, together with the most probable values of various particles, predicted by the Bethe-Bloch formula. The Bethe-Bloch rule can be observed: the $\frac{\mathrm{d}E}{\mathrm{d}x}$ distributions only depend on the particle velocity, thus the $\frac{\mathrm{d}E}{\mathrm{d}x}$ information together with the particle charge and momentum can be used for particle type identification.

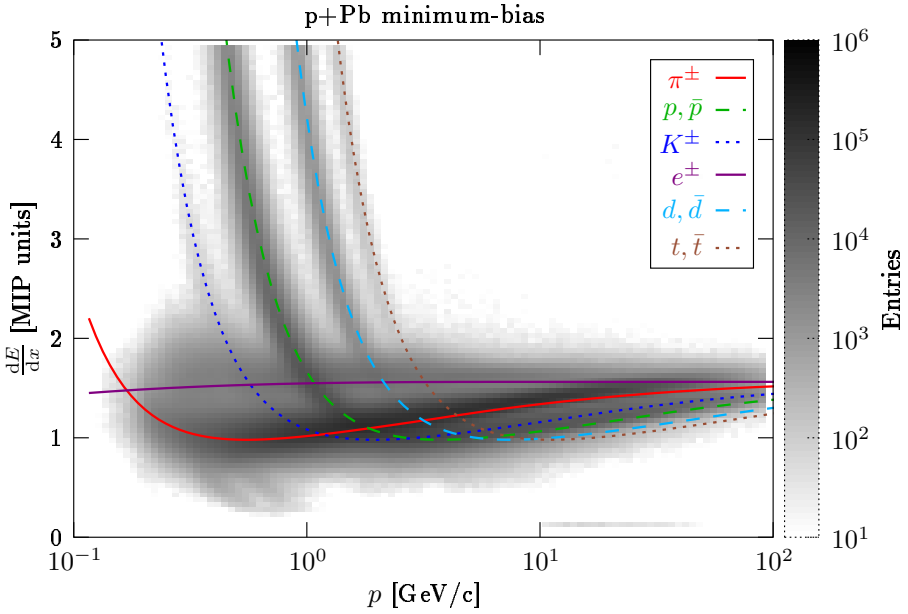

Figure 34: The correlation of the momentum and the specific energy loss for different particle types, together with the most probable energy loss values.

As was discussed in Section 4.2, the accepted momentum space region is located around midrapidity, and is elongated in the transverse momentum direction. The accepted region was sliced up in the transverse momentum direction, and the resulting momentum space bins are indexed by the p_T values of their centers in the p_T projection. We shall refer to these bins as the transverse momentum bins or p_T bins. However, we have to emphasize, that the resulting bins also extend significantly in the longitudinal

rapidity and charge-corrected azimuth directions in a p_T-dependent way. This shall be treated by the acceptance correction, later in Section 6.4. It also has to be noted, that the definition of the longitudinal rapidity depends on the mass hypothesis ($\pi^{\pm}$, $p, \bar{p}$, $K^{\pm}$ masses), therefore the accepted momentum space region is slightly different at low p_T for the different mass assumptions. To treat each particle with its right mass hypothesis, the momentum space cut and particle identification procedure was performed with all the three mass hypotheses, and the yield of each particle type was finally taken from the results of the according analysis, which assumes the correct mass for it.

In every transverse momentum bin, a fit to the specific ionization spectrum was performed, assuming the presence of the particle types $\pi^{\pm}$, $p, \bar{p}$, $K^{\pm}$, $e^{\pm}$. The fit was done separately for both charge signs. The $\frac{\mathrm{d}E}{\mathrm{d}x}$ response function of each particle type is known accurately, however the weights of the response functions (the particle entries) are unknown, and was kept as free parameters during the fits. In this way, the entries of each particle kind can be determined in each transverse momentum bin, thus the raw particle spectra are obtained as a function of transverse momentum. This method is known as inclusive particle identification, i.e. particle identification on the spectrum level: we cannot tag the reconstructed tracks with particle types, instead we are able to tell the amount of each particle type in a given momentum space bin. This method is also used in many NA49 publications (for references see e.g. [51, 58, 59, 60]).

For the $\frac{\mathrm{d}E}{\mathrm{d}x}$ response functions, the following parameterization (see e.g. [58]) was used for particles having tracks with fixed number of spacepoints N, having a fixed momentum p and corresponding to a fixed particle type (namely: $\pi^{\pm}$, $p, \bar{p}$, $K^{\pm}$ or $e^{\pm}$). The conditional probability density function of specific ionization (the condition is N, p and the particle type) is assumed to be Gaussian with mean value M and standard deviation $\sigma(C, M, N) = \frac{C}{\sqrt{N}} \cdot M^{0.625}$. Here C is a common global phenomenological constant, and M is the most probable value of the specific ionization distribution for particles with the given momentum p and type. The value M should correspond in ideal case to the nominal value given by the Bethe-Bloch function, however it is kept as a free parameter in the fits, because detector distortions can make the specific energy loss distributions slightly different from the Bethe-Bloch prediction. Thus, for a single particle type with fixed momentum and number of spacepoints, the theoretical function fitted to data would look like

$$\frac{\mathrm{d}E}{\mathrm{d}x} \mapsto \text{Entries} \cdot \Delta \cdot \frac{1}{\sqrt{2\pi\sigma^2(C, M, N)}} \exp\left(-\frac{\left(\frac{\mathrm{d}E}{\mathrm{d}x} - M\right)^2}{2\sigma^2(C, M, N)}\right),$$

where Entries is the number of entries of the particle type, and Δ is the binwidth of the specific ionization histogram. Thus, nine parameters are free in the fit, namely Entries and M for the four particle type, and the common width parameter C.

Each p_T bin is a rather large momentum space bin: belonging to a p_T bin cannot be viewed as a momentum fixing condition (and thus as a potential point fixing condition). The most probable value M varies with momentum p approximately according to the Bethe-Bloch formula. As the particle sample of a p_T bin is a mixture of a wide range of momenta, the variation of M with p introduces an additional smearing effect. This can be partly factorized out, as for pion, proton and Kaon $M(p) \approx a + 0.13 \cdot \ln \frac{p}{\mathrm{GeV/c}}$, while for electron $M(p) \approx a$ holds in the relativistic rising branch, where the offset parameter a only depends on the particle type.[16] In order to make the most probable values of the $\frac{\mathrm{d}E}{\mathrm{d}x}$ distributions of pion, proton and Kaon to be momentum independent, we transform our data, and consider the quantity $\frac{\mathrm{d}E}{\mathrm{d}x} - 0.13 \cdot \ln \frac{p}{\mathrm{GeV/c}}$ instead of $\frac{\mathrm{d}E}{\mathrm{d}x}$. The most probable value of this quantity will be approximately momentum independent (it is the offset parameter a) for pion, proton and Kaon, but the width will sill be momentum dependent (it is $\frac{C}{\sqrt{N}} \cdot \left(a + 0.13 \cdot \ln \frac{p}{\mathrm{GeV/c}}\right)^{0.625}$). For electron, the most probable value will be momentum dependent (it is $a - 0.13 \cdot \ln \frac{p}{\mathrm{GeV/c}}$), but the width will be momentum independent (it is $\frac{C}{\sqrt{N}} \cdot a^{0.625}$). The momentum independence of the most probable value of the quantity $\frac{\mathrm{d}E}{\mathrm{d}x} - 0.13 \cdot \ln \frac{p}{\mathrm{GeV/c}}$ guarantees that the resulting hadron peaks will be sharper (better resolution), thus the fits will be safer.

A single transverse momentum bin contains a mixture particles with different momenta and number of spacepoints. The variation of the momentum and of the number of spacepoints in a single transverse momentum bin can be rather large (e.g. 30%). Therefore, the realistic fit function for a single transverse momentum bin and particle type should be taken to be a superposition of the above Gaussian distributions with appropriate weights: the resultant probability density function of the specific ionization is obtained by mixing the discussed conditional probability density function with the observed density function of the $\left(\frac{1}{\sqrt{N}}, \ln \frac{p}{\mathrm{GeV/c}}\right)$ pair in each transverse momentum bin. This latter density function is obtained form the data (in each given transverse momentum bin) by histograming, as shown in Figure 35.

The used fitting algorithm is not the usual χ^2 minimization, because it underestimates the area, when fitting histograms with low number of entries. The reason is that the χ^2 method is only equivalent to a maximum-likelihood fitting, when the number of entries in the histogram bins follow Gaussian distribution. However, the entries in

[16] This approximate parameterization was determined from the data.

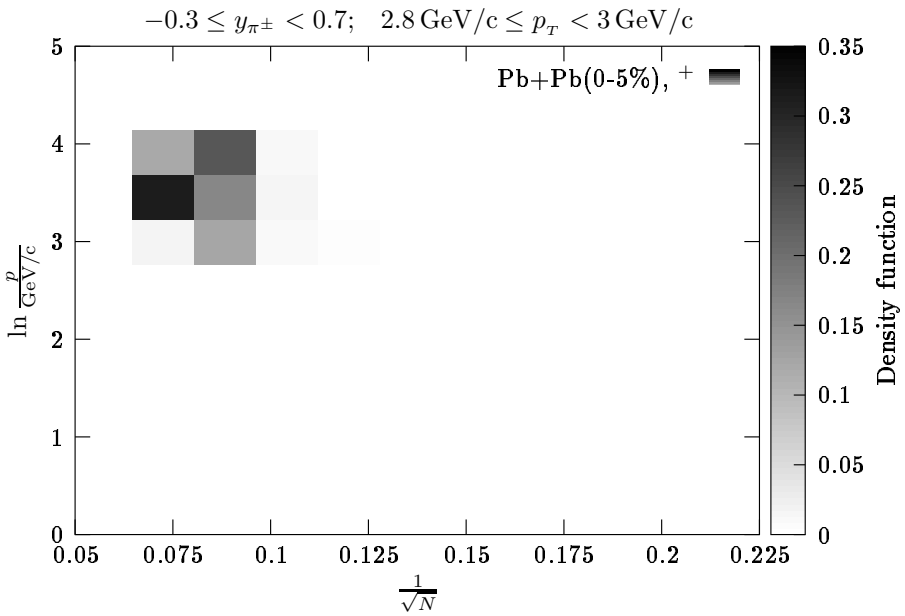

Figure 35: Example plot for the $\left(\frac{1}{\sqrt{N}}, \ln \frac{p}{\mathrm{GeV/c}}\right)$ distribution.

a histogram bin obey Poisson distribution (which is approximately Gaussian only for large number of entries). Therefore, a maximum likelihood fit with Poisson hypothesis is the exact solution, which can be transformed to a usual minimization problem as in the Gaussian case. The function to be minimized, which is -2 times the natural logarithm of the likelihood function with Poisson hypothesis is (see [23]):

$$2 \sum_i \left(y_i(\lambda) - n_i + n_i \ln \left(n_i / y_i(\lambda) \right) \right)$$

instead of the naive (Gaussian hypothesis) χ^2 expression

$$\sum_i \frac{\left(n_i - y_i(\lambda) \right)^2}{n_i},$$

where $i \mapsto n_i$ are the measured entries of the histogram, $i \mapsto y_i(\lambda)$ are a model for these, while λ is some parameter set of the model. The latter χ^2 formula would only be valid for histograms with large number of entries, i.e. in the large statistics limit. The minimization procedure was performed with the Levenberg-Marquardt method (see e.g. [49]).

In order to show the quality of the particle identification fits, a few example plots are

presented in Figure 36. The quality of the particle identification fits varies in transverse momentum: it is good in the low transverse momentum region, and becomes very good at high transverse momentum ($p_T \geq 1\,\mathrm{GeV/c}$), as the tracks become longer.

It is a rather important question to estimate the particle yield loss by the particle identification fits. Therefore, an efficiency notion of the fits was introduced in the following way. The entries in each $\frac{\mathrm{d}E}{\mathrm{d}x} - 0.13 \cdot \ln \frac{p}{\mathrm{GeV/c}}$ histogram was counted, then the fitted entries for the four particle type (pion, proton, Kaon, electron) for the given histogram was summed. The efficiency was defined by the relative difference of this fitted entries to the counted entries. As observed, this results in at most about 1% systematic underestimation (negligible).

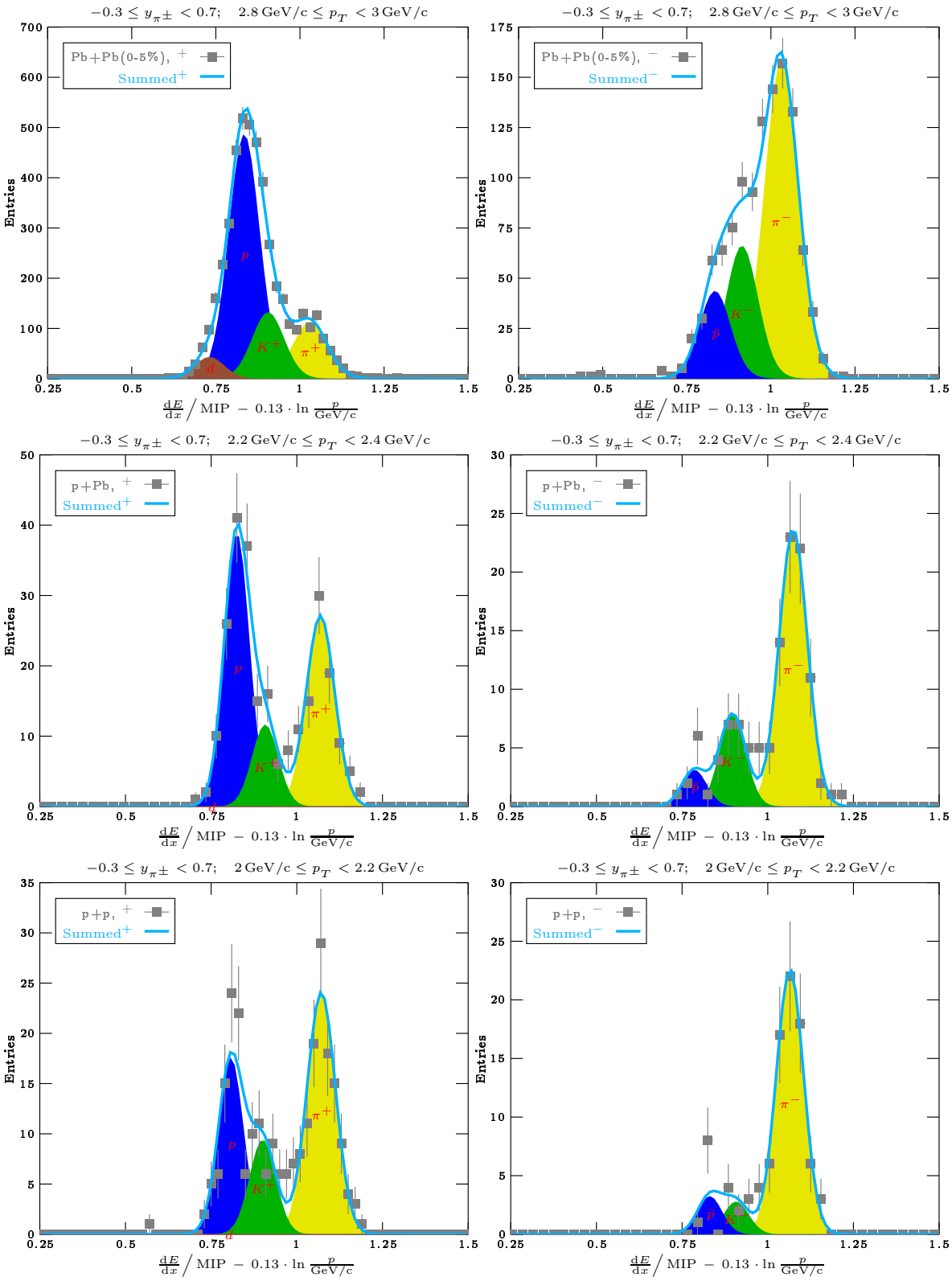

Figure 36: Demonstration of the particle identification fits, $\pi^\pm$ mass hypothesis.

6 Corrections

In the next sections, the applied corrections to the raw particle spectra are discussed in detail.

6.1 Correction for Non-Target Contamination and Loss by the Main-Vertex Cut

The Pb+Pb particle yield studies were performed by using the narrow V_z-cut, which means a ± 1 standard deviation cut in the V_z distribution for the lowest total multiplicity events. The reason for the use of such a strict V_z-cut instead of the more permissive wide V_z-cut is that in the case of the wide V_z-cut, a remarkable amount of non-target events contaminate our peripheral event sample (we refer to Figure 12). In principle, this could be corrected by subtracting the non-target particle yields, collected by using the gas V_z-cut, as shown before. However, as the non-target event sample is rather limited in statistics, this is not feasible at high p_T, because the track statistics of the non-target background vanishes at about $p_T \geq 2\,\mathrm{GeV/c}$. Therefore, to reduce the non-target contamination, we chose a stricter V_z-cut, the narrow V_z-cut, to limit the non-target contamination at the price of losing some low multiplicity (ultraperipheral) target events.

The remaining non-target contamination can directly be estimated by the gas V_z-cut event sample, as in the case of the wide V_z-cut. The lost target event sample can be estimated by doing the same analysis also with the wide V_z-cut, correcting for non-target, which delivers the true event and track counts. Then, by subtracting the non-target corrected counts obtained with the narrow V_z-cut, delivers the amount of target events and tracks, which were erroneously thrown away by the narrow V_z-cut. The remaining non-target contamination among the recorded events in the $(33.5-80\%)$ centrality interval turned out to be 5%, while the lost target events are also about 5%, cancelling each-other[17]. The non-target track counts are about 4%, p_T-independently, while the amount of lost tracks starts from about 3% and gradually vanishes with p_T, as can be seen in Figure 37. Clearly, the vanishing of the track count loss with p_T is due to the fact that events with high-p_T track(s) have better V_z resolution, thus it is not rejected by the narrow V_z-cut accidentally.

[17]This cancellation means that we replace the lost target events by non-target events. Fortunately, as the non-target events are mainly Pb+O and Pb+N reactions, these events are not expected to differ largely form the Pb+Pb(Peripheral) events around midrapidity.

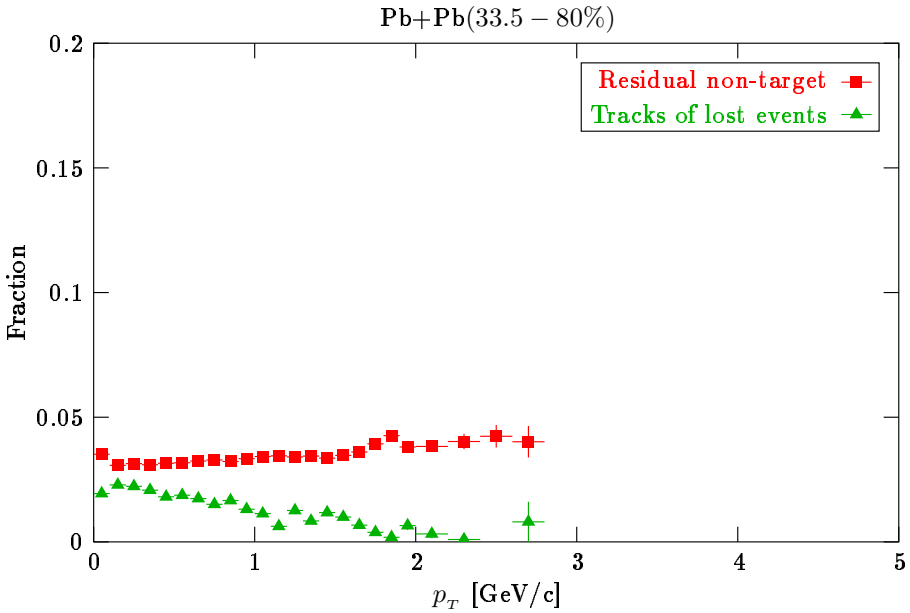

Figure 37: The systematic errors caused by the residual non-target contamination and the lost events on the track count level, in Pb+Pb(33.5 – 80%), with $\pi^{\pm}$ mass hypothesis.

By scaling down the particle yields in centrality interval $(33.5 - 80\%)$ with 1+ the difference of the curves, presented in Figure 37, these systematic errors can be corrected. (The curve of event loss can be extrapolated by zero at $p_T \geq 2.4\,\mathrm{GeV/c}$, while the curve of non-target contamination can be extrapolated by constant value from $p_T \geq 2.8\,\mathrm{GeV/c}$.)

A similar correction was to be done for the p+Pb and the p+p particle spectra. The difference is that for the determination of the non-target contribution, dedicated empty-target runs were used, which were identical to the normal runs, except that the target material was temporarily removed from the beamline. With the used V_z cuts, the non-target contamination and the event loss fractions were the following: in the case of p+Pb runs, 1% event loss was encountered, and the non-target contamination was 4% on the event count level, while for p+p, 2% event loss was registered, and the non-target contamination proved to be 6.5% on the event count level. The event counts were corrected for these effects. The track miscount, caused by the same effects for p+Pb and p+p are shown in Figure 38. The raw identified particle spectra were also corrected for these track miscount effects, just like in the case of peripheral Pb+Pb reactions.

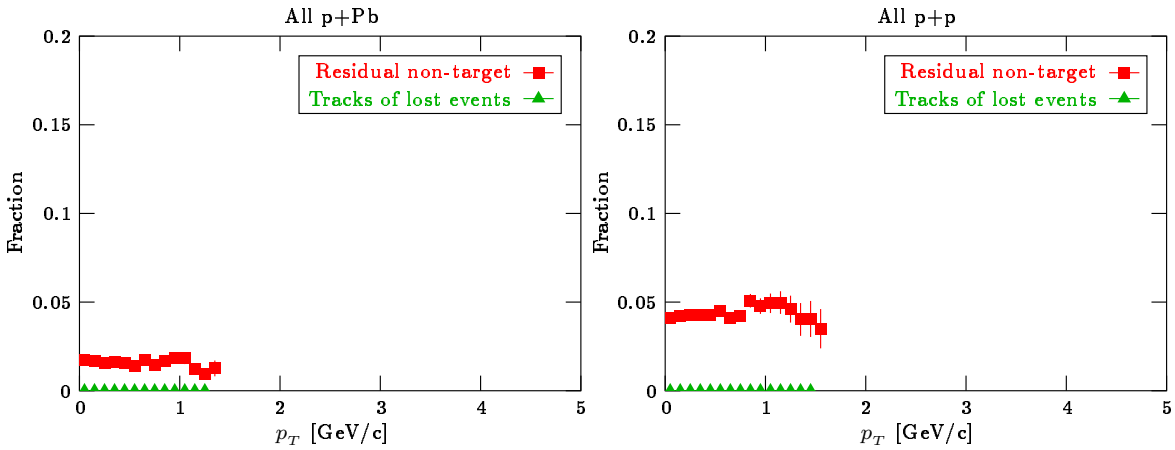

Figure 38: The systematic errors caused by the residual non-target contamination and the lost events on the track count level, in p+Pb (left) and p+p (right), with $\pi^{\pm}$ mass hypothesis.

6.2 Trigger Bias Correction

This correction is only relevant for the p+p and p+Pb spectra. In these cases the interaction trigger is a small (1 cm radius) downstream scintillator (4 m from the target), the S4, which if hit by a particle, rejects the event. With this concept, events falling into about 85% of the total inelastic cross-section are recorded, the rest is rejected as the S4 scintillator (erroneously) vetoes them. This is called the trigger bias. This distortion was studied by making off-line selection by using the GTPC (located directly behind the S4), simulating different S4 sizes. An extrapolation to the zero S4 size gives the undistorted cross-sections (detailed study was performed in [11, 12, 58]).

The biased events are mainly characterized by fast forward going particles, typical to diffractive events. The shape of the trigger bias function as a function of particle momentum is also qualitatively well understood. The loss is small for fast forward going particles, as if such a particle is detected in a recorded event, then it must have passed in the detector acceptance, and it must have missed the S4 counter. Due to momentum conservation, it is not possible to produce an other fast forward going particle in the event, hitting the S4, which could cause vetoing. Thus, losing such an event can only be due to slow particle hits, which are very unlikely, as they are bent out from the beamline by the magnetic field. The trigger bias can grow up to about 16% towards the backward region, as the previous argument may be reverted: due to the two-component picture, it is very likely that a fast backward particle is associated to a fast forward particle, which is likely to hit the S4 counter. Around midrapidity, the correction is

about 8% for p+p and about 3.5% for p+Pb, approximately p_T-independently above about $p_T \geq 0.5\,\mathrm{GeV/c}$.

6.3 Corrections from Monte Carlo

Some further corrections need Monte Carlo simulation of the detector. The full simulation of the apparatus is available in GEANT. Thus, one is able to follow the particle reconstruction from the signal generation level to the track fitting level. For Monte Carlo surveys, various event generation methods are used. One can use physical models, like VENUS-4.12, or one can prepare hand-made events. A special king of Monte Carlo event is an embedded event: such an event consists of a real measured event, onto which one embeds hand-made particles (e.g. a single proton track, whose momentum is known). Embedded events can be used to measure conditional probability values in connection with particle reconstruction in a very realistic way, the condition being the particle type and momentum.

To be able to follow the particle reconstruction procedure with the simulation, one does not only need generation, simulation and reconstruction of particles, but one also has to be able to pair the Monte Carlo particles to the reconstructed tracks. This is done by a $5\,\mathrm{mm} \times 5\,\mathrm{mm}$ searching tube around the simulated track: a reconstructed track is defined to be associated to a simulated (input) track if the reconstructed track has a point in this searching tube. Of course, this does not necessarily lead to a one-to-one correspondence between simulated tracks and reconstructed tracks: there may be simulated tracks with no associated reconstructed tracks (lost tracks), there may be reconstructed tracks not associated to any simulated track (fake tracks), or there may be more than one reconstructed tracks associated to a single simulated track (multiply reconstructed split tracks, or crossing tracks). To have only at most one valid reconstructed track associated to each simulated track, only the best match is considered (highest reconstructed points / simulated points ratio). This approach leaves the set of well reconstructed tracks intact, it is not disturbed by the crossing tracks, does not touch the original set of fake tracks, and each copy of a multiply reconstructed split track, which is not a best match to a simulated track, is considered as a fake track. It has to be noted, that by this classification, we do not lose any case of imperfectly reconstructed tracks, i.e. the bookkeeping of tracks by this method is correct: all the reconstructed tracks, which are not best matches are contributing to be fake track counts, i.e. any deviant way of track reconstruction can be immediately spotted out by an increased amount of fake track counts or by an increased amount

of track loss counts. After this pairing, the distribution of number of reconstructed points / number of simulated points can be seen in Figure 39. The figure was prepared by embedding single proton tracks into real Pb+Pb(0-5%) central events, uniformly in the accepted momentum space region.[18] As can be seen: the quality of the matching of reconstructed to simulated tracks is very good, independently of the transverse momentum, which demonstrates that the track matching procedure works properly.

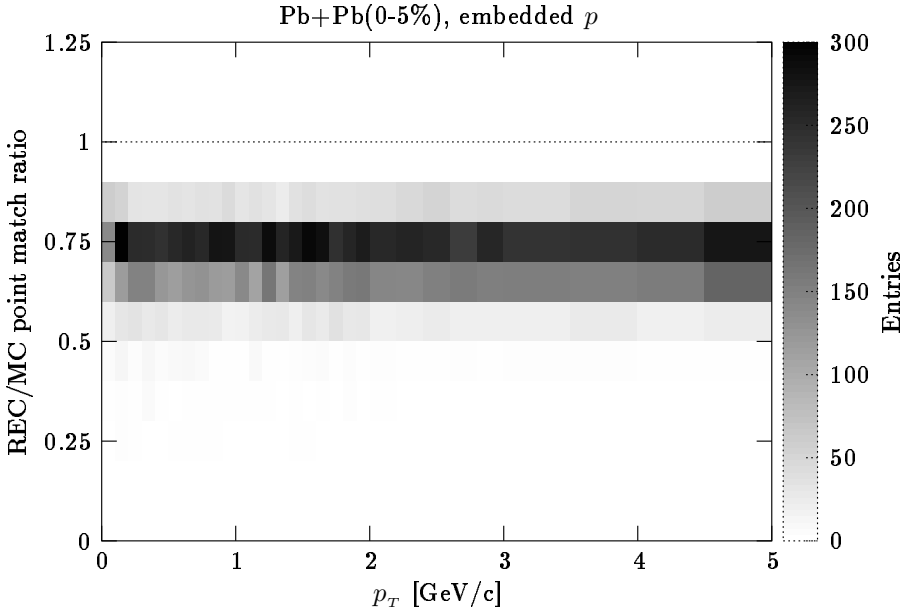

Figure 39: Quality of the matching of the Monte Carlo tracks to the reconstructed tracks in Pb+Pb$(0-5\%)$, $\pi^{\pm}$ mass hypothesis.

Now we are able to match reconstructed tracks to simulated tracks if the reconstruction was successful. It has to be checked that whether the reconstructed momentum is close to the input momentum, i.e. the momentum resolution is good. The relative difference of reconstructed momentum vectors to the input momentum vectors is shown in Figure 40. The points show the statistical mean value of this quantity, while the errorbars show the statistical standard deviation (and not the statistical error of the mean values). The figure was prepared by embedding single proton tracks into real Pb+Pb(0-5%) central events, uniformly in the accepted momentum space region. As can be seen, the reconstructed momentum vectors reproduce the input values accurately.

[18] The procedure of superimposing an artificial particle track onto a real event is called *embedding*. This is a widely applied technique in our experiment to take the actual track density environment into account in a realistic way.

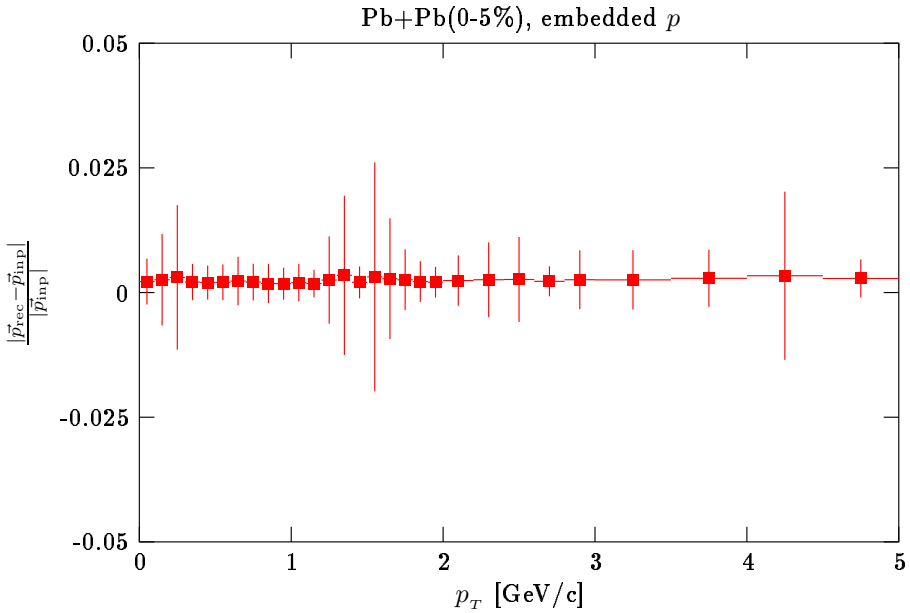

Figure 40: Momentum reconstruction quality in Pb+Pb$(0-5\%)$, $\pi^{\pm}$ mass hypothesis.

Finally, it has to be checked that the amount of fake tracks among the reconstructed tracks is negligible. For this, embedding cannot be used, realistic pure Monte Carlo events have to be applied: the fake tracks are defined by those reconstructed tracks, which cannot be paired to any simulated track (note that also multiply reconstructed copies of split tracks, which are not best matches to their input tracks, are also counted by this definition, thus all "deviant" reconstructed tracks stay in our scope). For this purpose, 100 k VENUS-4.12 events were used, which reproduce the track density of Pb+Pb events quite realistically. The fraction of fake tracks can be seen in Figure 41. As can be seen, the fake track contamination is negligible in our accepted momentum space region, after our track cuts, discussed in Section 4.2.

6.3.1 Feed-Down Correction

The feed-down contamination means contribution of secondary particles, i.e. particles which are decay products of other particles, accidentally reconstructed as primary particles. The main source of feed-down contributions are the decay channels, listed in Table 5.

To calculate the decay contributions, the table of conditional probabilities of reconstructing a child particle (with given type and momentum) as a primary particle from a

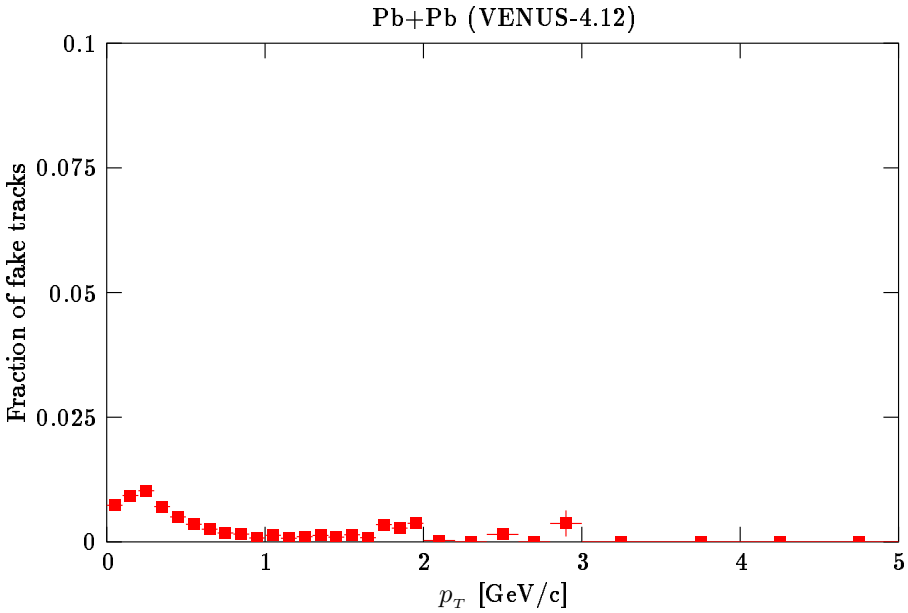

Figure 41: Fraction of fake tracks in Pb+Pb (VENUS-4.12), $\pi^{\pm}$ mass hypothesis.

K^0_s	$\rightarrow$	$\pi^+ \pi^-$	$\leq 5\%$ to $\pi^{\pm}$
Λ	$\rightarrow$	$p \pi^-$	$\leq 30\%$ to p
$\bar{\Lambda}$	$\rightarrow$	$\bar{p} \pi^+$	$\leq 30\%$ to $\bar{p}$
Σ^+	$\rightarrow$	$p \pi^0$	$\leq 6\%$ to p
Σ^+	$\rightarrow$	$n \pi^+$	
Σ^-	$\rightarrow$	$n \pi^-$	
$\bar{\Sigma}^-$	$\rightarrow$	$\bar{p} \pi^0$	$\leq 6\%$ to $\bar{p}$
$\bar{\Sigma}^-$	$\rightarrow$	$\bar{n} \pi^-$	
$\bar{\Sigma}^+$	$\rightarrow$	$\bar{n} \pi^+$	

Table 5: The list relevant feed-down channels.

mother particle (with given type and momentum) was measured by embedding mother particles into empty events. (The feed-down contribution is mainly of kinematic nature, and is expected to have very weak dependence on track density, therefore empty events were used, to reduce the need for computing power.) Given the yield of mother particles as a function of particle type and momentum

$$(t_m, \vec{p}_m) \mapsto f_m(t_m, \vec{p}_m),$$

one can calculate the feed-down yield of child particles as a function of particle type

and momentum by the integral

$$(t_c, \vec{p}_c) \mapsto f_c(t_c, \vec{p}_c) = \sum_{t_m} \int \rho(t_c, \vec{p}_c | t_m, \vec{p}_m)\, f_m(t_m, \vec{p}_m)\, \mathrm{d}^3 p_m,$$

once the conditional probabilities

$$(t_c, \vec{p}_c, t_m, \vec{p}_m) \mapsto \rho(t_c, \vec{p}_c | t_m, \vec{p}_m)$$

are measured by simulation. The particle spectra are then corrected for feed-down by subtracting these calculated yields from the raw particle spectra.

The yields of relevant mother particles K^0_s, Λ and $\bar{\Lambda}$ were obtained by parameterizations of yields, measured previously in our experiment (see [22, 31, 34]). The parameterizations themselves are presented in detail in [44]. The Λ, $\bar{\Lambda}$ spectra also include the $\Sigma^0 \to \Lambda\gamma$ and the $\bar{\Sigma}^0 \to \bar{\Lambda}\gamma$ contributions, however they are feed-down corrected for the $\Xi^0 \to \Lambda\pi^0$, $\Xi^- \to \Lambda\pi^-$ and the $\bar{\Xi}^+ \to \bar{\Lambda}\pi^+$, $\bar{\Xi}^0 \to \bar{\Lambda}\pi^0$ decays. Despite of this fact, their missing contribution to the $\Lambda, \bar{\Lambda}$ production is small, as the $\Xi^0, \Xi^-, \bar{\Xi}^+, \bar{\Xi}^0$ yields are below the 20% of the $\Lambda, \bar{\Lambda}$ yields, respectively. The K^0_s are not contaminated by feed-down contributions.

For π^+ the only sizeable contribution is given by the $K^0_s \to \pi^+\pi^-$ channel, while for π^- also the $\Lambda \to p\pi^-$ decay has to be taken into account. The p ($\bar{p}$) yield is mostly contaminated by Λ ($\bar{\Lambda}$) decays, however there are also other sources (Σ^+, $\bar{\Sigma}^-$). The $K^\pm$ yields are practically not contaminated by feed-down.

The $\bar{p}$ feed-down yield largely depends on the measured $\bar{\Lambda}$ temperatures, which bear a relatively large error. To quantify the systematic errors of the $\bar{p}$ feed-down yields, the analysis was redone by assuming the $\bar{\Lambda}$ temperatures to be equal to the Λ temperatures. This provides an upper estimate for the $\bar{\Lambda}$ temperatures. The resulting systematic error of the feed-down corrected $\bar{p}$ spectra is 5%.

The contribution of Σ^+ and $\bar{\Sigma}^-$ was taken into account by scaling up the Λ and $\bar{\Lambda}$ yields by 20%. This treatment was suggested by the VENUS-4.12 model: the relative intensity of the Σ^+ channel to the Λ channel, furthermore the relative intensity of the $\bar{\Sigma}^-$ channel to the $\bar{\Lambda}$ channel was predicted to be about constant 20% by this model. Assuming an 50% uncertainty of this scaling, we end up with at most 3% systematic uncertainty of the feed-down corrected $p, \bar{p}$ yields, originating from this error source.

The resulting feed-down contributions are shown in Figure 42 relative to the measured raw particle spectra. As can be seen, this correction is the most relevant for

the $p, \bar{p}$ particles, because of the feed-down from $\Lambda, \bar{\Lambda}$ decays. (Due to the small mass difference between p and Λ or between $\bar{p}$ and $\bar{\Lambda}$, the dominant part of the momentum of the mother Λ or $\bar{\Lambda}$ is inherited by the resulting p or $\bar{p}$, which fakes primary p or $\bar{p}$ tracks.) For $\pi^{\pm}$, the feed-down correction is under about 7% and vanishing with p_T, while for $p, \bar{p}$, this correction can be up to 30%, decreasing with p_T. Thus, the systematic errors of the feed-down estimation dominates the systematic errors of the particle spectra.

6.3.2 Tracking Inefficiency Correction

The spectra are also corrected for tracking inefficiency. The inefficiency correction was determined by measuring the conditional probability of losing a track during the reconstruction (the condition being the particle type and momentum). This study was performed by embedding single particles into real events, as this correction is expected to depend largely on the track density. For decaying particles ($\pi^{\pm}$ and $K^{\pm}$), this approach ensures that the failure of track reconstruction due to early decay of particles is also taken into account (decay loss correction). The resulting tracking inefficiencies can be seen in Figure 43. The tracking inefficiency is on the level of 10% for Pb+Pb events. The decay loss correction is negligible for $\pi^{\pm}$, and it varies between 30% and 0% for $K^{\pm}$. For p+p and p+Pb events, the tracking inefficiency is negligible, and the decay loss correction is the same as for Pb+Pb, as the decay loss is of purely kinematic/geometrical origin.

The spectra are corrected for tracking inefficiency and decay loss by dividing them by 1− the cumulative inefficiency curves (which depend on particle type due to different decay loss curves).

6.4 Acceptance Correction

An ideal goal for particle spectrum measurement can be to determine the spectra of identified particles as a function of all kinematic degrees of freedom, e.g. as a function of (y, p_T) (the azimuthal degree of freedom is irrelevant, as the single particle spectra are axially symmetric). This is the largest possible amount of knowledge, which one can extract on single particle production. (Of course, particle correlation studies can give further insights to the structure of events, but this is not in the scope of our analysis.) A commonly used quantity for yield measurement is the 'invariant yield'

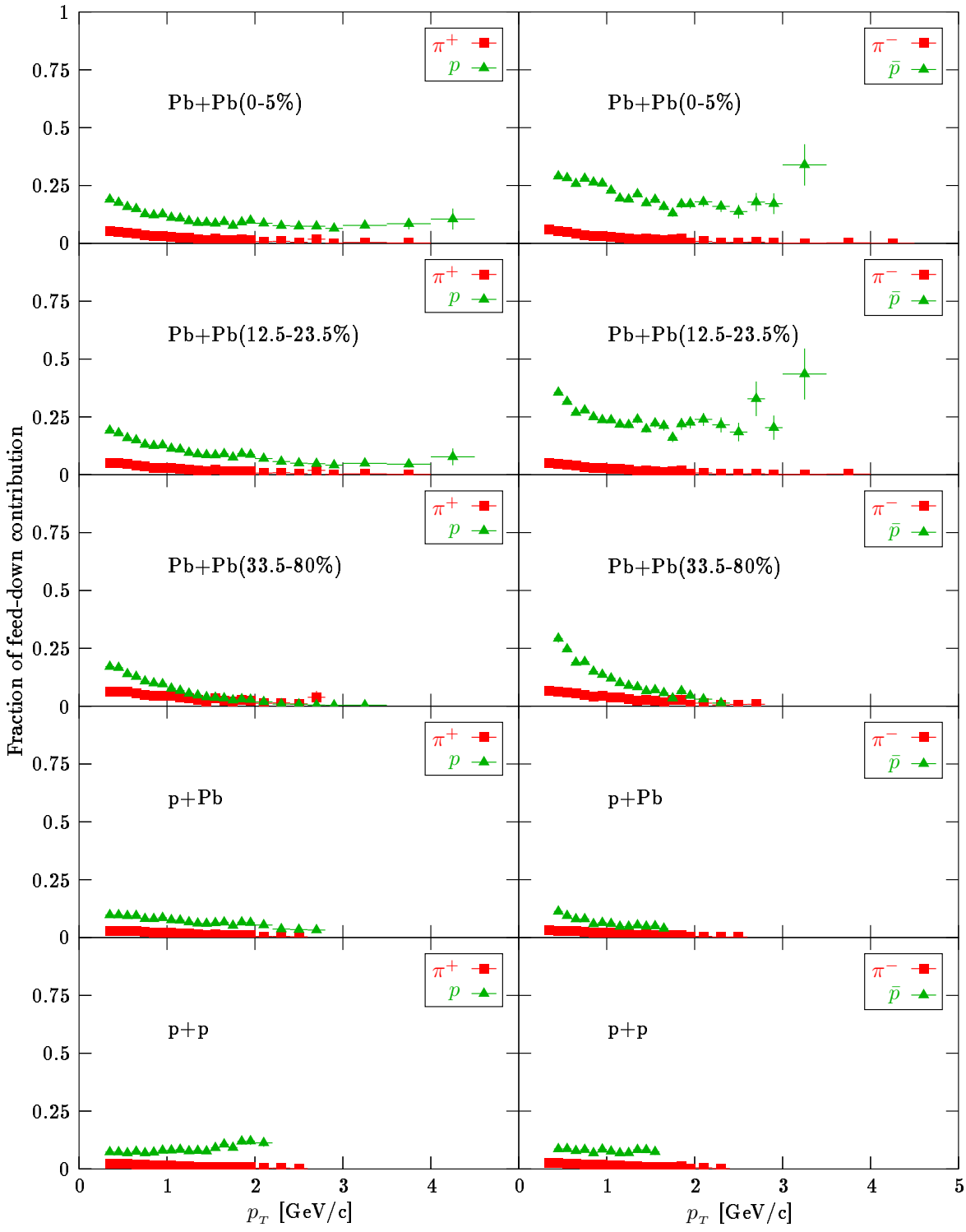

Figure 42: Feed-down contributions to the $\pi^{\pm}$ and $p, \bar{p}$ channels. ($K^{\pm}$ are omitted, as they have do not have significant feed-down contributions.)

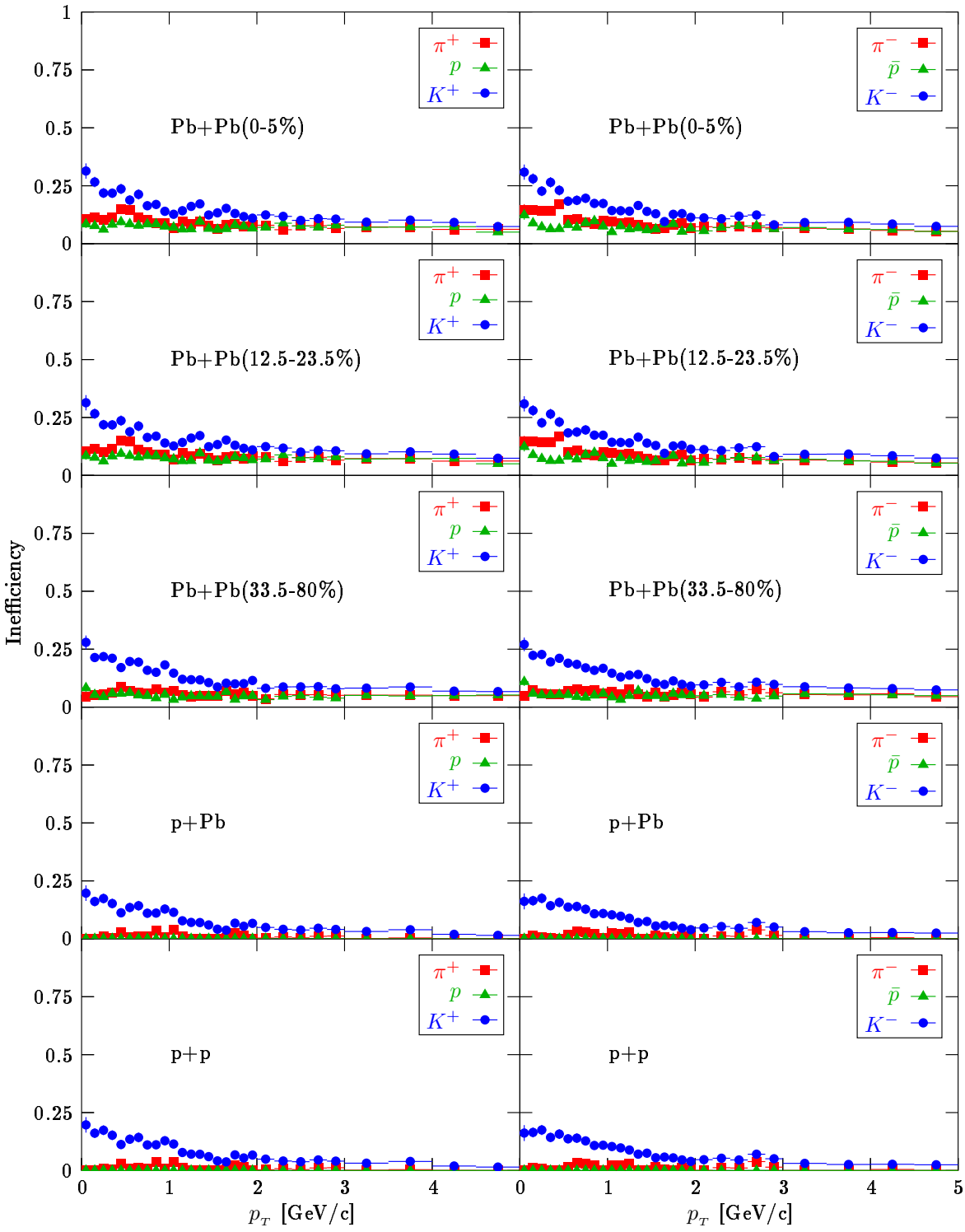

Figure 43: Tracking inefficiency for $\pi^{\pm}$, $p, \bar{p}$ and $K^{\pm}$. (For $\pi^{\pm}$ and $K^{\pm}$ decay loss correction is also included.)

(see Appendix A), which is defined by

$$(y, p_T) \mapsto \frac{1}{2\pi \cdot p_T} \cdot \frac{\mathrm{d}^2 n}{\mathrm{d}y \, \mathrm{d}p_T},$$

where the quantity $\frac{\mathrm{d}^2 n}{\mathrm{d}y \, \mathrm{d}p_T}$ means the particle yield per event, differentiated in y and p_T. The name invariant yield comes from the fact, that this quantity means a differential yield on the mass shell of the given particle, with respect to the Lorentz invariant volume measure of the mass shell $p_T \, \mathrm{d}y \, \mathrm{d}p_T \, \mathrm{d}\varphi$ (φ being the azimuth coordinate). This quantity is also invariant in the sense that the action of a longitudinal boost with a rapidity value Δy on the invariant yield is merely a translation in the y direction by Δy.

A both longitudinally and transversally differential study was performed e.g. in [11, 12] for p+p and p+C, furthermore there is such a study for p+Pb in preparation. However, the available track statistics of our experiment is not enough to go to $p_T \geq 2\,\mathrm{GeV/c}$ if the single particle spectra are also differentiated longitudinally (this is also the case for most experiments). Furthermore, due to the high track density, the Pb+Pb reactions cannot be studied in a too wide y range, because of the difficulties of high p_T track reconstruction, as was discussed in Section 4.2: the region of high p_T studies is limited to the $-0.3 \leq y < 0.7$ rapidity interval. As a fall-back, our goal shall be to measure the identified particle spectra (invariant yields) as a function of p_T at midrapidity, i.e. at the $y = 0$ slice.

To measure the $\frac{\mathrm{d}^2 n}{\mathrm{d}y \, \mathrm{d}p_T}$ quantity at $y = 0$, we use the raw $\frac{\mathrm{d}^2 n}{\mathrm{d}y \, \mathrm{d}p_T}$, measured on the accepted momentum space region as a function of p_T, which we measure for $\pi^{\pm}$, $p, \bar{p}$ and $K^{\pm}$ as a result of the particle identification fits in the p_T bins, described in Section 5.1. As the particle spectra of Pb+Pb and p+p reactions are changing very little on the $-0.3 \leq y < 0.7$ interval (see e.g. the rapidity spectra published in [7]), the rapidity distributions may assumed to be approximately flat in this given rapidity window.[19] Therefore, to gain track statistics, the full $-0.3 \leq y < 0.7$ rapidity interval may be used to approximate the $y = 0$ slice. (This approximation causes about a 2% systematic underestimation of identified particle yields.) However, as was shown in Figure 29, the accepted ϕ region is (y, p_T) dependent. As our goal is to measure the $\frac{\mathrm{d}^2 n}{\mathrm{d}y \, \mathrm{d}p_T}$ integrated on the full $-180^\circ \leq \phi < 180^\circ$ domain, we have to extrapolate the particle yields

[19] The Pb+Pb and p+p reactions are symmetric, thus their particle spectra are also symmetric in y. As the rapidity spectra of these reactions are known to have an at most parabolic maximum at $y = 0$, they are approximately flat around midrapidity. This region around the maximum, where the variation of the particle spectra is small, is known to be very broad in y.

from our limited ϕ coverage to the full $-180^\circ \leq \phi < 180^\circ$ coverage. This is handled by the acceptance correction: the particle spectra at each p_T bin are divided by the actual volume of the p_T bin and are multiplied by the volume of the p_T bin assuming $-180^\circ \leq \phi < 180^\circ$ coverage. As the ϕ distribution is flat in an exact manner, this approach delivers the acceptance corrected spectra, provided that the y distribution in the region is approximately also flat.

As the p+Pb reaction is not symmetric, its rapidity spectra are also not symmetric: they have a significant slope around $y = 0$. Therefore, the y spectra of p+Pb reaction cannot be approximated as flat around $y = 0$: if one uses the whole $-0.3 \leq y < 0.7$ interval for the approximation of the p_T spectra at $y = 0$, one also has to correct for the y dependence. This is simply treated by measuring the y spectrum at each p_T-bin (by taking a very narrow y- and p_T-independent ϕ slice around 0°), and using this shape instead of flat y distribution in the above discussed correction procedure: instead of the volume of the p_T bin, one has to take the (y, ϕ) distribution (normalized to 1 at $y = 0$) integrated on the p_T bin. Of course, the needed computing power increases by this double differentiating, plus the track statistics dies out quicker. Therefore, the shape of the y distributions was extrapolated in p_T from the $p_T = 2\,\mathrm{GeV/c}$ y distribution curves. As was observed, the change of the y spectrum shape is very small (negligible) when evolving in p_T, therefore this extrapolation is meaningful.

As an example, the acceptance correction curve for symmetric reactions (Pb+Pb and p+p) is shown in Figure 44. Although this correction is large and rapidly varying, it can be calculated with high accuracy, as it is only influenced by the detector geometry and kinematics, and can be determined without Monte Carlo. The large steps in the correction curve are due to changes in the p_T binsize at $p_T = 2\,\mathrm{GeV/c}$ and $p_T = 3\,\mathrm{GeV/c}$, the correction for which is included in the acceptance correction curve.

The fully corrected particle spectra in Pb+Pb carry the cumulative systematic uncertainties, listed in Table 6, while the p+Pb and p+p particle spectra carry additional 5% systematic errors, originating from the uncertainties of the trigger bias, discussed in Section 6.2. The systematic errors of p and $\bar{p}$ spectra are larger due to the lack of accurate knowledge on the Λ and $\bar{\Lambda}$ yields.

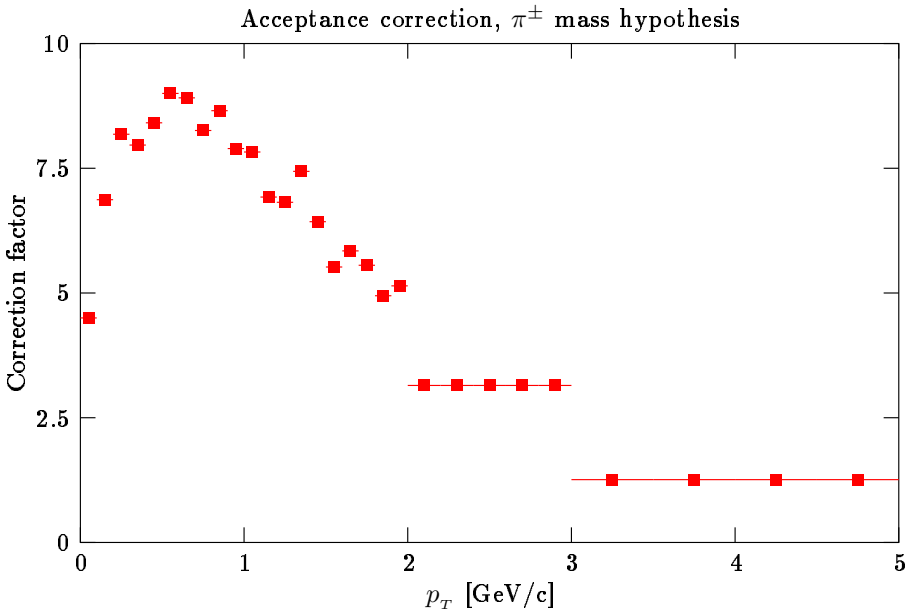

Figure 44: The acceptance correction curve for symmetric reactions, with $\pi^{\pm}$ mass hypothesis.

particle type	acceptance correction	feed-down yields	feed-down shapes	quadratic sum
$\pi^{\pm}$	2%			2.0%
p	2%	3%		3.6%
$\bar{p}$	2%	3%	5%	6.2%
$K^{\pm}$	2%			2.0%

Table 6: Systematic error sources for Pb+Pb particle production spectra.

7 Results and Discussion

In the next sections, we shall present the $\pi^{\pm}$, $p, \bar{p}$, $K^{\pm}$ single particle spectra, obtained by the discussed procedures, for the $\sqrt{s_{NN}} = 17.3\,\mathrm{GeV}$ Pb+Pb, p+Pb and p+p reactions. A new method, developed by the author for the purpose of π^0 spectrum extraction, is also introduced.

The derived quantities of the particle production spectra are also shown and discussed. The underlying physical picture is elucidated by comparing data to the $\sqrt{s_{NN}} = 200\,\mathrm{GeV}$ RHIC results [4, 6], to blast-wave parameterization published in [13] based on [50], and to perturbative QCD calculations [64] based on [63]. The comparison to RHIC data is used to extract an energy dependence picture on the elementary properties of the single particle spectra. The consistency check to blast-wave parameterization shall evaluate, whether the different temperatures of the low p_T particle species can be explained by a common temperature, and a boost introduced by an expanding source. The comparison to the predictions of the perturbative QCD based in-medium energy loss model shall provide information on whether the involved high p_T particle production processes are already in the perturbative region.

The related publications of the author on the stated results are also emphasized in the text. These reference entries are typeset with **bold face** characters for transparency.

7.1 Identified Charged Hadron Spectra in Pb+Pb, p+Pb and p+p Reactions

The main result of our analysis, the identified charged hadron inclusive spectra ($\pi^{\pm}$, $p, \bar{p}$, $K^{\pm}$) in $\sqrt{s_{NN}} = 17.3\,\mathrm{GeV}$ Pb+Pb, p+Pb and p+p collisions, are shown in Figure 45 and are listed in Table 9, 10, 11, 12, 13 in Appendix C. In Figure 45, the formerly published NA49 production spectra from [7, 16, 11] are also drawn on top of the newly obtained data, by solid bands, for comparison. It is seen that the agreement to the formerly published low p_T spectra is excellent. It also has to be noted, that the p_T coverage of the presented new analysis is far larger than that of the formerly published spectra, especially for the central Pb+Pb case, for which the p_T coverage was extended from $0 - 1.5\,\mathrm{GeV/c}$ to $0 - 4.5\,\mathrm{GeV/c}$. Also the variety of the presented particle species is larger. The simple reason for the larger p_T coverage is that without the track selection method, presented in Section 4.2, the very high fake rate makes

the single particle spectrum extraction impossible, as was shown in Figure 24. Since this cleaning method, developed by the author, was not known at the time of the publication of [7, 16, 11], the measurement of the single particle spectra at higher p_T was not feasible.

The presented particle spectra carry at most about 5% systematic uncertainty in the Pb+Pb case, and about 8% in the p+Pb and p+p case. This difference can be accounted for the uncertainties of the trigger bias correction in the p+Pb and p+p case, discussed in Section 6.2. The uncertainty is slightly larger for $p, \bar{p}$, and smaller for $\pi^{\pm}, K^{\pm}$ particles, due to the larger uncertainty in the $p, \bar{p}$ feed-down correction from $\Lambda, \bar{\Lambda}$ decays, as discussed in Section 6.3.1. From the experimental point of view, the stated high accuracy is a result of the following philosophy of the applied data handling:

(a) either the cuts (event and track selection methods) were optimized in such a way that the corrections become small (non-target and event loss correction, trigger bias correction, inefficiency correction), or when this was not possible,

(b) the cuts were optimized in such a way that the large corrections can be calculated with a high accuracy, e.g. because the given corrections are of geometrical or of kinematic nature (acceptance correction, decay loss correction, and partly also the feed-down correction[20]).

Preliminary versions[21] of the presented particle spectra were published by the author for the NA49 Collaboration in **[40, 54, 45]**. These spectra were also used in the argumentation of **[17, 18, 19, 46]**, written by the author for the NA61 Collaboration. The final form of the Pb+Pb spectra were published in the experimental article **[15]**, together with a brief overview of the experimental methods, discussed in Chapters 3, 4, 5, 6.

The physical information, which directly can be seen from Figure 45, is that the baryon spectra are harder than the meson spectra (harder spectrum: the fall-off slope is smaller). Later, this shall be shown more explicitly by particle production ratios.

[20] Despite of the fact that the feed-down correction is of kinematic kind, the largest uncertainty is introduced by this correction, due to the insufficient knowledge on the double differential yields of the mother particles.

[21] Only with acceptance correction. Also the calculation of the average collision parameters was not as accurate as for the final version.

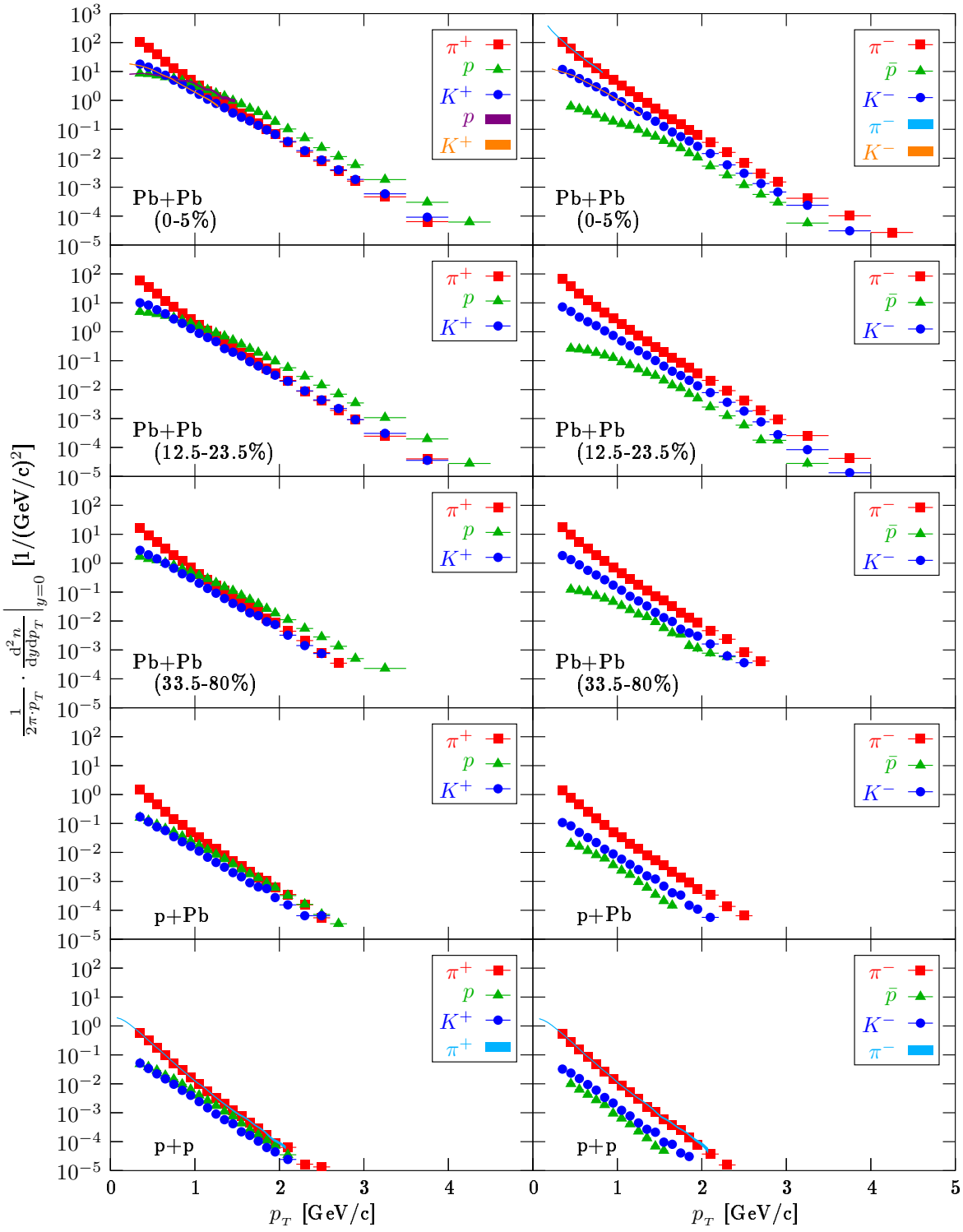

Figure 45: The fully corrected invariant yields at $y = 0$ of $\pi^{\pm}$, $p, \bar{p}$, $K^{\pm}$ particles in $\sqrt{s_{NN}} = 17.3$ GeV Pb+Pb, p+Pb and p+p reactions.

7.2 A New Method for π^0 Spectrum Measurement

Besides of charged hadrons, the behavior of the neutral hadron spectra is also interesting. Therefore, an attempt was made by the author to extract p_T spectra for π^0 particles at midrapidity from the NA49 data. Although dedicated π^0 measurements were made at the CERN SPS by the WA98 collaboration [9], these results are not in perfect consistency with the presented $\pi^\pm$ results. Similar phenomenon can be observed on data of the RHIC experiments [4, 2] (see a comparison plot in [15]). A very likely explanation of the difference between the $\pi^\pm$ and π^0 spectra may be the shortcomings of the calorimetric detection method of π^0 particles via their $\pi^0 \to \gamma\gamma$ decay channel: even the best calorimeter has much worse momentum resolution than a charged particle tracking detector.[22] There is a possibility at NA49 to detect π^0 particles with a non-calorimetric method. The idea of detection is based on the fact, that the $\gamma \to e^+e^-$ conversion probability, for γ-s formed inside the target, is about 1%. The γ photons may be reconstructed via the tracks of the e^+ and e^- particles in the TPC volumes, and the π^0 particles may be reconstructed from the γ candidate pairs. Indeed, the π^0 signal can be seen by this method at NA49, as shown in Figure 56 in Appendix B, however the statistics is too low for momentum spectrum extraction, due to the very low γ pair detection probability. Motivated by the statistical shortcomings of the direct π^0 spectrum measurement method by γ pairs, a theory for indirect π^0 spectrum measurement was developed by the author, which only needs the detection of single γ particles. The philosophy of this indirect method is to measure the single γ momentum spectrum, and (assuming that all the γ particles originate from π^0 decays) the π^0 momentum spectrum is reconstructed from this, by unfolding. The unfolding means the inversion of certain integral operators in probability theory.[23] Unfortunately, there is no generally applicable method known in literature, for solving a general unfolding problem. Seeing this theoretical shortcoming, the author developed a generally

[22] The smearing effect of the non-ideal resolution of a calorimeter can largely change the shape of the measured particle spectra. As was shown by the author in [42], this can be a large effect even with the best calorimeters, and not necessarily only dominant at low momenta (as one would naively think), where the resolution gets poor. The smearing has increasing effect with growing momentum, and cannot be corrected by naive Monte Carlo.

[23] Let two probability density functions be g and f over some finite dimensional vector space X, and a conditional probability density function be ρ over $X \times X$, and assume that $g(y) = \int\limits_{x \in X} \rho(y|x)\, f(x)\, \mathrm{d}x$ for all $y \in X$. The unfolding means the reconstruction of the unknown 'initial' f from the known 'measured' g and the known 'response function' ρ. A special case of unfolding is the deconvolution, when ρ is translation invariant in the sense that for all $x, y, z \in X$ we have $\rho(y + z|x) = \rho(y|x - z)$. In that case $\rho(y|x) = \rho(y - x|0)$, i.e. ρ may be expressed by a single probability density function $x \mapsto \rho(x|0)$.

applicable iterative method for unfolding (see Appendix B). This theoretical result, which has a general relevance in signal processing, was published by the author in the mathematical article **[41]**.

7.3 Anti-particle/Particle Asymmetry

The anti-particle/particle yield asymmetry is shown in Figure 46. For comparison, $\sqrt{s_{NN}} = 200\,\mathrm{GeV}$ RHIC results are also shown. It is seen, that the production of lightest mesons (π^-/π^+) is already approximately symmetric at SPS energy. This is due to the fact that the $\pi^\pm$ production threshold is far lower than the given nucleon-nucleon collision energy. The yields of the heavier hadrons do not admit such anti-particle/particle symmetry at SPS energy. As the $\sqrt{s_{NN}} = 200\,\mathrm{GeV}$ is far larger than the production threshold of $\pi^\pm, p, \bar{p}, K^\pm$, the anti-particle/particle yields are approximately symmetric at RHIC. Both the K^-/K^+ and $\bar{p}/p$ ratios decrease with p_T at SPS energy. This means that the K^+ spectra are harder than the K^- spectra, and the p spectra are harder than the $\bar{p}$ spectra.

The small but well visible difference of π^- relative to π^+ yields can be accounted for the isospin asymmetry of the initial state. This is most pronounced for the p+p collisions: as the initial system is maximally non-isospin symmetric, the asymmetry in the π^-/π^+ ratio is the most pronounced. The π^- particles are suppressed relative to π^+ particles, as the isospin of the initial state is positive. As the p+Pb and Pb+Pb systems are far less asymmetric in isospin, their π^-/π^+ ratios are much closer to one. In these cases, the π^- production is slightly enhanced relative to the π^+ production, as the initial system has negative isospin.

The $p, \bar{p}$ yields are highly asymmetric at SPS energy. The two reasons are:

(a) the energy threshold for baryon production is not too far from the collision energy, leading to a low baryon production cross-section, i.e. the dominant part of the final state baryons are inherited from the initial state, and

(b) the initial state is highly asymmetric in the anti-baryon/baryon content, as it purely consists of baryons, thus the baryon number conservation implies a large baryon excess over anti-baryons (as was already depicted in Figure 3).

This spectrum asymmetry becomes less pronounced with increasing collision energy, as the baryon production cross-section increases: at higher energies, the produced baryons dominate the yield at midrapidity, and not the inherited (net-) baryons.

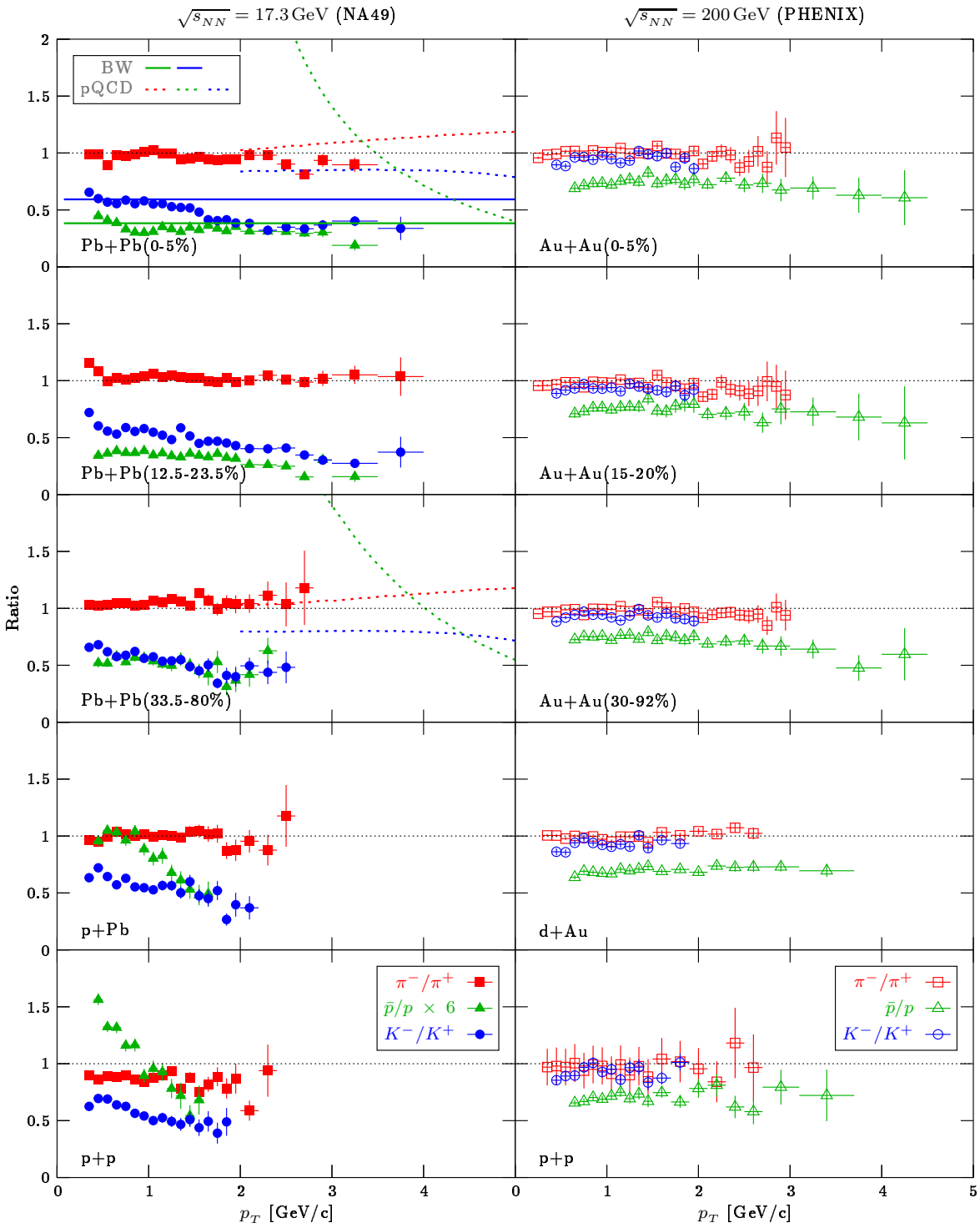

Figure 46: Anti-particle/particle ratios at $y = 0$ in $\sqrt{s_{NN}} = 17.3\,\text{GeV}$ Pb+Pb, p+Pb and p+p reactions. Similar data for $\sqrt{s_{NN}} = 200\,\text{GeV}$ Au+Au, d+Au and p+p reactions are also shown. BW: blast-wave parameterization. pQCD: perturbative QCD calculation.

The $K^{\pm}$ yields are also not symmetric. A primary reason for this effect is that the K^+ and K^- mesons are not isospin partners, so the isospin conservation does not impose any constraint on the production symmetry. Despite of this fact, the $K^{\pm}$ yield is expected to be symmetric for those Kaons, which originate from pair production, as they are the anti-particles of each-other. The excess of K^+ over K^- production can be explained by a gluonic $\bar{u}+u \rightarrow \bar{s}+s$ and $\bar{d}+d \rightarrow \bar{s}+s$ transition, which is able to open other channels than pair production: the 'associated production' channels. Taking into account the valence quark structure, such reactions can be e.g. the $\pi^+ + p \rightarrow K^+ + \Sigma^+$, $\pi^+ + n \rightarrow K^+ + \Lambda$, or $\pi^- + p \rightarrow K^0 + \Lambda$, $\pi^- + n \rightarrow K^0 + \Sigma^-$ associated productions. Also such associated production processes can exist, where the u, d valence quarks of the colliding baryonic matter is paired with an $\bar{s}$ sea quark (resulting in K^+ and K^0 production), and its s pair is picked up by other u, d valence quarks (resulting in strange baryon production). Also 'associated absorption' processes can exist: K^- particles may be absorbed in the baryonic matter, based on a strangeness exchange of the form $K^- + p \rightarrow \pi^- + \Sigma^+$, $K^- + n \rightarrow \pi^- + \Lambda$, or $\bar{K}^0 + p \rightarrow \pi^+ + \Lambda$, $\bar{K}^0 + n \rightarrow \pi^+ + \Sigma^-$. These associated reactions are driven by the baryon (or u, d) excess of the initial state. The similar associated channels of the charge-conjugated particles are suppressed by the low amount of anti-baryon (or $\bar{u}, \bar{d}$) content of the formed matter. It is seen that the $K^{\pm}$ asymmetry vanishes with increasing collision energy. This fact can be accounted for the increased amount of produced anti-baryon content, which opens the associated production/absorption channels also for the anti-Kaons. Both associated production and absorption scenarios enhance K^+ yields relative to K^-, and increase the strange baryon yield, therefore the dominance of associated production versus absorption cannot be judged a priori. However, associated absorption is expected to need higher net-baryon density. It is seen from Figure 46, that the $K^{\pm}$ asymmetry at SPS energy is independent of the colliding system (Pb+Pb(Central), Pb+Pb(Midcentral), Pb+Pb(Peripheral), p+Pb and p+p), which suggests that the Kaon production mechanism is similar for all the shown reactions. This would mean that the associated production is dominant, as in p+p the net-baryon density is only high at very forward and very backward regions, furthermore there is no final state rescattering, thus the associated absorption is "chemically" not supported.

The blast-wave parameterization predicts constant anti-particle/particle ratios[24], agreeing well to our data in the region $p_T \leq 1.5\,\mathrm{GeV/c}$, as expected: the blast-wave result of [13] was obtained by fitting the blast-wave parameterization [50] simultane-

[24] In the blast-wave description, the shape of the particle spectra only depends on particle mass, therefore the spectrum shape for particles and anti-particles are the same.

ously to the m_T spectra of [7] (low p_T NA49 results) and to the measured source radii, obtained by the two-boson correlation analysis, presented in [13]. The good agreement to the blast-wave parameterization at low p_T means, that the particle spectra (at low transverse momentum) are consistent to a physical picture, assuming collective behavior of particles, thermally emitted from an expanding cylindrical source. In the region $p_T \geq 1.5\,\mathrm{GeV/c}$ the blast-wave parameterization slightly overpredicts the ratios. This is not surprising, as good agreement to collective models at high p_T is not expected to hold: the high p_T part of the spectrum is rather expected to originate either from hard QCD processes, or from excited nucleon decays, both of which are not necessarily expected to be collective.

The perturbative QCD calculation does not seem to be consistent with the measured $\bar{p}/p$ and K^-/K^+ ratios, as it highly underpredicts the asymmetry for $K^\pm$ and $p, \bar{p}$. The π^-/π^+ ratios are well reproduced, however this is expected, as approximate symmetry already holds for $\pi^\pm$ production at SPS energy. An inconsistency to perturbative QCD calculation at intermediate energies or momenta may always be explained by assuming soft processes being responsible for the given interaction, i.e. with the assumption that the elementary momentum transfers are not sufficiently large compared to the momentum scale of QCD, leading to large effective coupling factor. Most probably, the net-baryon number transfer is not a purely perturbative QCD process at SPS energies in the covered momentum region, which can give rise to wrong $\bar{p}/p$ predictions (e.g. some of the baryon content may simply be inherited from the initial state). However, as we shall show, purely this assumption is not enough to explain this discrepancy, as the produced $\bar{p}$ spectra carry most of this effect (see later in Sections 7.5, 7.6). The disagreement to the measured K^-/K^+ ratio may also be explained by such scenario: most probably the associated K^+ production is not a hard process, thus it need not be described well by perturbative QCD at SPS energies. However, also for this case we shall show, that purely this assumption is not enough to explain the discrepancy, as the K^- spectra carry most of this effect (see later in Section 7.4).

7.4 Strange Meson Production

The K^+/π^+ and K^-/π^- ratios are shown in Figure 47. Similar quantities at $\sqrt{s_{NN}} = 200\,\mathrm{GeV}$ are also shown for comparison. The "net associated K^+" yield relative to the average $\pi^\pm$ yield (defined by $\frac{2(K^+-K^-)}{\pi^++\pi^-}$) is also shown, which should depict the production of the associated K^+ particles relative to $\pi^\pm$. This latter quantity can be easily calculated from the NA49 data, but cannot be extracted with reasonable statistical

errors from the PHENIX data, nevertheless the obtained RHIC result is also shown for comparison. (The physical meaning of the $\frac{2(K^+-K^-)}{\pi^++\pi^-}$ ratio is different at RHIC, as the K^- particles are also expected to include associated production contribution, therefore at RHIC energy, this ratio cannot be interpreted as purely the associated K^+ production contribution.)

Some features of the data can immediately be observed. Due to the behavior of the $K^\pm$ asymmetry and $\pi^\pm$ symmetry, the K^+/π^+ and K^-/π^- ratios differ from each-other at SPS energy, and become very similar at higher energies, as the $K^\pm$ yields become symmetric with increasing collision energy. It is seen, that the production of $K^\pm$ relative to $\pi^\pm$ shows a monotonic increase with p_T, i.e. the $K^\pm$ spectra are harder than the $\pi^\pm$ spectra. The K^-/π^- ratio shows a saturation at $p_T = 1.5\,\mathrm{GeV/c}$ at SPS energy. The RHIC K^+/π^+ and K^-/π^- data resemble more to the K^+/π^+ at SPS, which can be explained by the presence of associated Kaon production. The large difference between the K^-/π^- ratios at SPS and RHIC can be explained by the lack of associated K^- production at SPS: it is seen that the K^-/π^- ratio shows an excess at RHIC over the SPS values. It is surprising, however, that the K^+/π^+ production at RHIC is practically the same for p+p, d+Au and Au+Au (centrality independently), and is very similar to the corresponding SPS data in p+p, whereas the SPS K^+/π^+ ratio shows an excess over the RHIC results in nucleus-nucleus collisions (centrality independently).

The discussed effects are better seen in Figure 48, where we show the energy dependence of the results by double ratios. It is clearly seen, that the K^+/π^+ ratio at SPS energy (which also contains the contribution of associated production just like the higher energy RHIC data) shows an excess over the RHIC result in nucleus-nucleus collisions, p_T and centrality independently. For proton-proton and proton(deuteron)-nucleus collision, the RHIC to SPS ratio of K^+/π^+ is approximately constant one within errors. The surprising phenomenon of K^+/π^+ integrated yield excess at SPS nucleon-nucleon collisions was already a known fact (see [14] Figure 4, left panel), and is commonly referred to as "the horn". A possible interpretation of this phenomenon is the onset of deconfinement. The K^+/π^+ peak, presented in [14], can be qualitatively explained in the framework of statistical models, assuming the change of degrees of freedom from hadronic to partonic at the collision energy, corresponding to the peak position. An alternative explanation assumes purely hadronic scenario, and the peak is explained by the opening of the K^+ associated production channel at SPS energies (resulting in the rise), and the decrease of the net-baryon rapidity density at higher

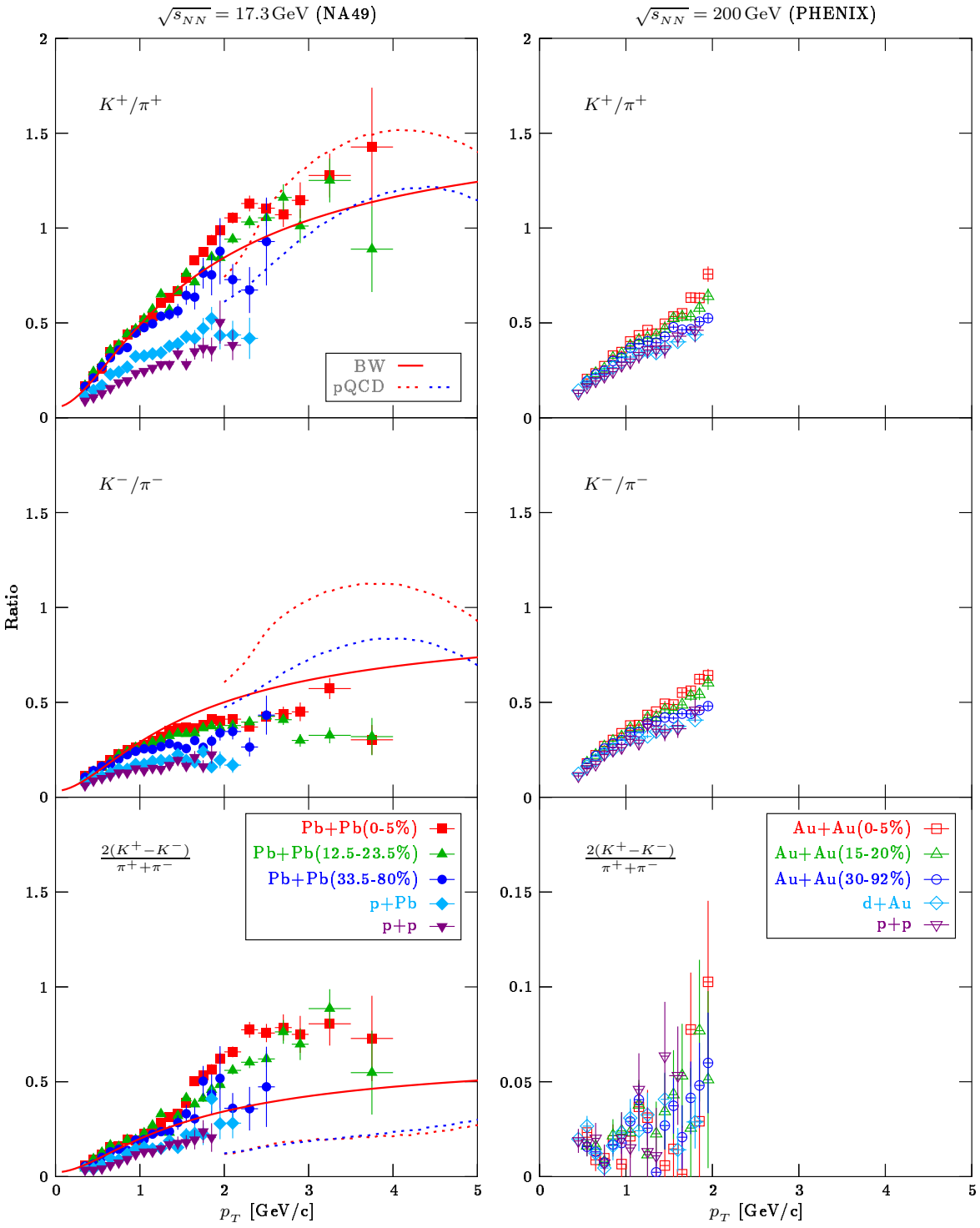

Figure 47: K^+/π^+, K^-/π^-, and $\frac{2(K^+-K^-)}{\pi^++\pi^-}$ ratios at $y = 0$ in $\sqrt{s_{NN}} = 17.3\,\mathrm{GeV}$ Pb+Pb, p+Pb and p+p reactions. Similar data for $\sqrt{s_{NN}} = 200\,\mathrm{GeV}$ reactions are also shown. BW: blast-wave parametrization. pQCD: perturbative QCD calculation.

energies (resulting in the fall). This scenario is suggested by the fact that the K^-/π^- integrated yield ratio does not show such yield excess peak, instead it admits a smooth evolution. A possible counter-argument for this can be that the K^-/π^- ratio is, in fact, artificially suppressed by associated absorption. However, due to the similarity of the K^-/K^+ ratios in p+p, p+Pb and Pb+Pb (centrality independently), the associated absorption scenario is not very likely, as this contribution is expected to be very low in p+p, as there is no final state rescattering.

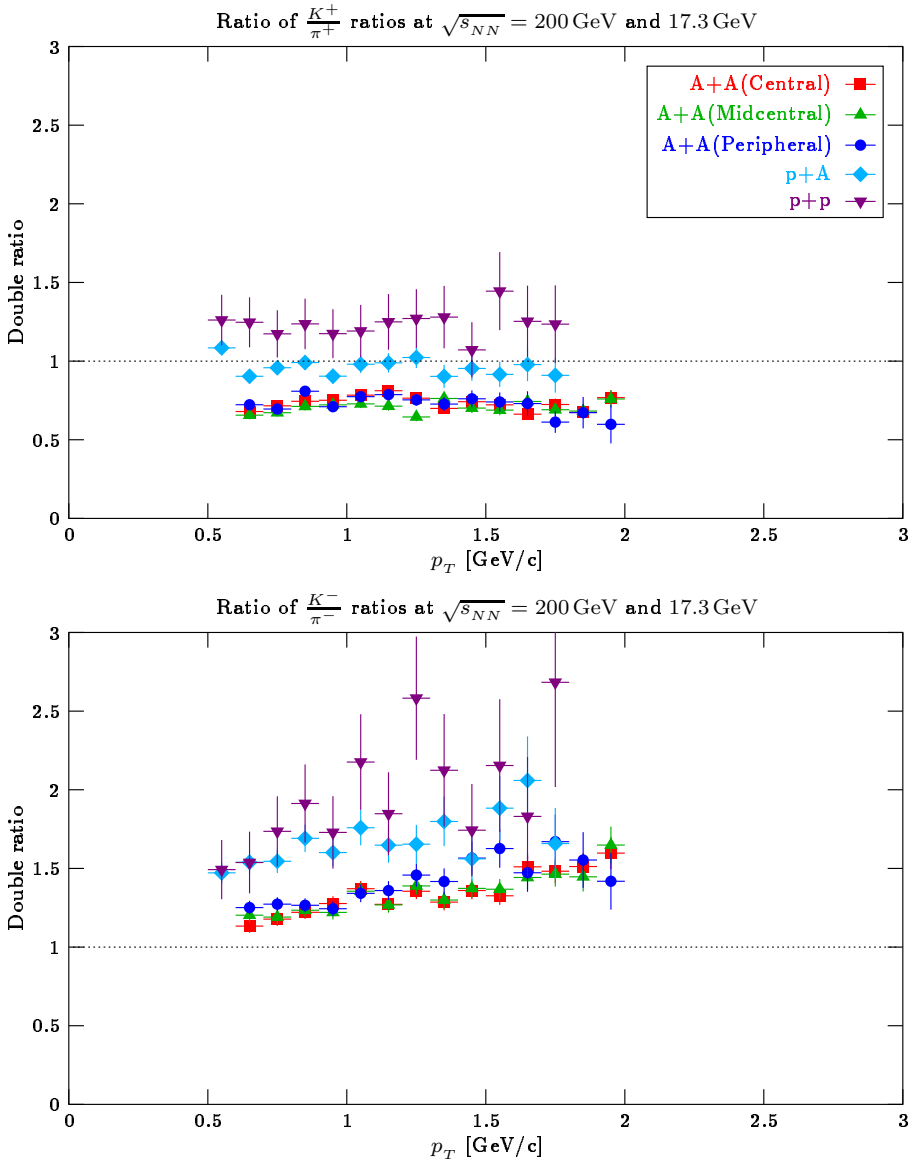

Figure 48: Ratio of K^+/π^+ and K^-/π^- ratios at $\sqrt{s_{NN}} = 200\,\text{GeV}$ and $\sqrt{s_{NN}} = 17.3\,\text{GeV}$ collision energy.

The blast-wave parameterization has proved again to be consistent to the low transverse momentum data, whereas at high transverse momenta (above $1.5\,\mathrm{GeV/c}$) it deviates from the data, as expected.

The perturbative QCD calculation seems to be consistent with the K^+/π^+ ratio, however it fails to describe the K^-/π^-. This is surprising, as the K^- particles are expected to be the "real", "produced" particles, whereas the K^+ yield is expected to contain also associated production which is not expected to be a hard process. The physical expectation would be that the K^-/π^- is described better by a perturbative QCD based model than the K^+/π^+ ratio.

7.5 Baryon/Meson Ratios

The p/π^+, $\bar{p}/\pi^-$ ratios are shown in Figure 49. Similar quantities at $\sqrt{s_{NN}} = 200\,\mathrm{GeV}$ are also shown for comparison. The ratio of net-proton yield relative to the average $\pi^\pm$ yield (defined by $\frac{2(p-\bar{p})}{\pi^+ + \pi^-}$) is also shown.

The extracted data allow the following immediate observations. The p/π^+ and $\bar{p}/\pi^-$ ratios differ from each other at SPS energy, as the $p, \bar{p}$ yield is highly asymmetric, whereas at RHIC energy, the ratios are much more similar due to the approximate $p, \bar{p}$ symmetry. This is a result of higher $p, \bar{p}$ production with increased energy, and the decreased net-baryon rapidity density around midrapidity with increased collision energy (as was outlined in Figure 3). The p/π^+ ratios are largely different for proton-proton, proton(deuteron)-nucleus and nucleus-nucleus (centrality dependently), both at SPS and RHIC energies, and their evolution with the reaction types is rather different. The $\bar{p}/\pi^-$ ratios are largely different at SPS and at RHIC, which is due to the increased amount of $\bar{p}$ production at higher energies. The reaction type (and centrality) dependence of $\bar{p}/\pi^-$ ratio is much weaker at SPS energies than at RHIC. The production of net-protons $(p - \bar{p})$ is also calculated. The net ("inherited") proton to charged pion ratio shows an interesting feature: the shape and centrality evolution of these ratios are quite similar at the two extreme energies, up to a normalization factor. This is better seen in Figure 50, where the energy evolution of the p/π^+, $\bar{p}/\pi^-$ and $\frac{2(p-\bar{p})}{\pi^+ + \pi^-}$ ratios are shown via double ratios. It is seen, that the double ratios of p/π^+, $\bar{p}/\pi^-$ are not constant in p_T, and they are reaction type and centrality dependent. The $\frac{2(p-\bar{p})}{\pi^+ + \pi^-}$ double ratio is approximately constant in p_T, therefore the net-proton to pion ratio only depends on the collision energy through a normalization factor. The normalization factor should be directly influenced by the ratio of the net-baryon and the pion rapidity

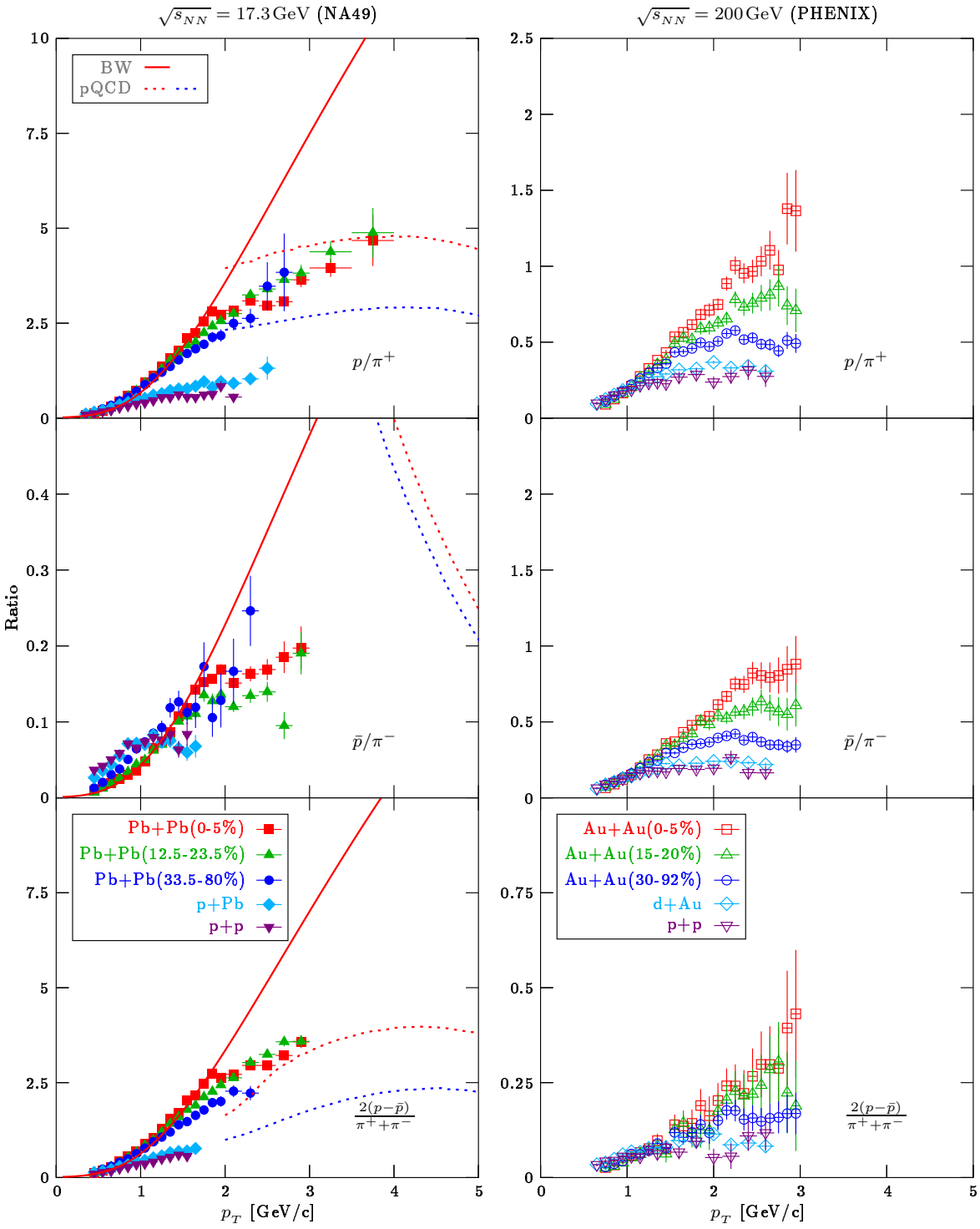

Figure 49: Proton/pion ratios at $y = 0$ in $\sqrt{s_{NN}} = 17.3\,\text{GeV}$ Pb+Pb, p+Pb and p+p reactions. Similar data for $\sqrt{s_{NN}} = 200\,\text{GeV}$ reactions are also shown. BW: blast-wave parametrization. pQCD: perturbative QCD calculation.

density around midrapidity. This factorization would also explain the observed very weak centrality dependence of the $\frac{2(p-\bar{p})}{\pi^+ + \pi^-}$ double ratio in nucleus-nucleus collisions, as the rapidity density ratio at midrapidity of net-protons to pions in nucleus-nucleus reactions is not expected to have very strong centrality dependence (not considering ultraperipheral events), whereas in proton(deuteron)-nucleus and proton-proton collisions, the net-proton rapidity density is largely different than that of nucleus-nucleus.

The extracted ratios, again, are seen to be consistent to the blast-wave parameterization at $p_T \leq 1.5\,\mathrm{GeV/c}$, and the parameterization largely overpredicts the data at higher transverse momenta, showing that the collective behavior picture is not consistent to the data there.

The perturbative QCD calculation seems to be consistent with the p/π^+ ratio, both in the central and in the peripheral case, however it largely overpredicts the $\bar{p}/\pi^-$ data for the peripheral case. This is surprising, as the $\bar{p}$ particles are expected to be the purely "real", "produced" particles, whereas the p yield is mainly driven by the net-baryons, where the net-baryon production is not necessarily expected to be hard process. The physical expectation would be that the $\bar{p}/\pi^-$ is described better by a perturbative QCD based model than the p/π^+ ratio.

7.6 Nuclear Modification Factors

As outlined in Section 1.3, the in-medium modification of the single particle spectra of a given reaction, relative to a reference reaction, may be measured by the nuclear modification factor, defined as the scaled particle yield ratio of the two inclusive reaction type. If the considered reaction is $A + B \to t + X$ inclusive t production, and the reference reaction is $C + D \to t + X$ (t being a particle type and X being an unconstrained ensemble of produced particles), then the nuclear modification factor is

$$R_{A+B/C+D}(t) := \frac{N_{C+D}}{N_{A+B}} \cdot \frac{\text{Invariant yield}(A + B \to t + X)}{\text{Invariant yield}(C + D \to t + X)}.$$

Here N_{A+B} and N_{C+D} denote scaling factors, the ratio of which is used to scale up the reference yield $C+D \to t+X$ to $A+B \to t+X$ yield, assuming that the A+B reaction is a simple superposition of many elementary C+D reactions. Typically, A+B is chosen to be a nucleus-nucleus or proton-nucleus collision (possibly with constrained centrality), and C+D is e.g. a same energy proton-proton reference reaction. The choice of the scaling factors N_{A+B} and N_{C+D} strongly depends on the assumed particle production

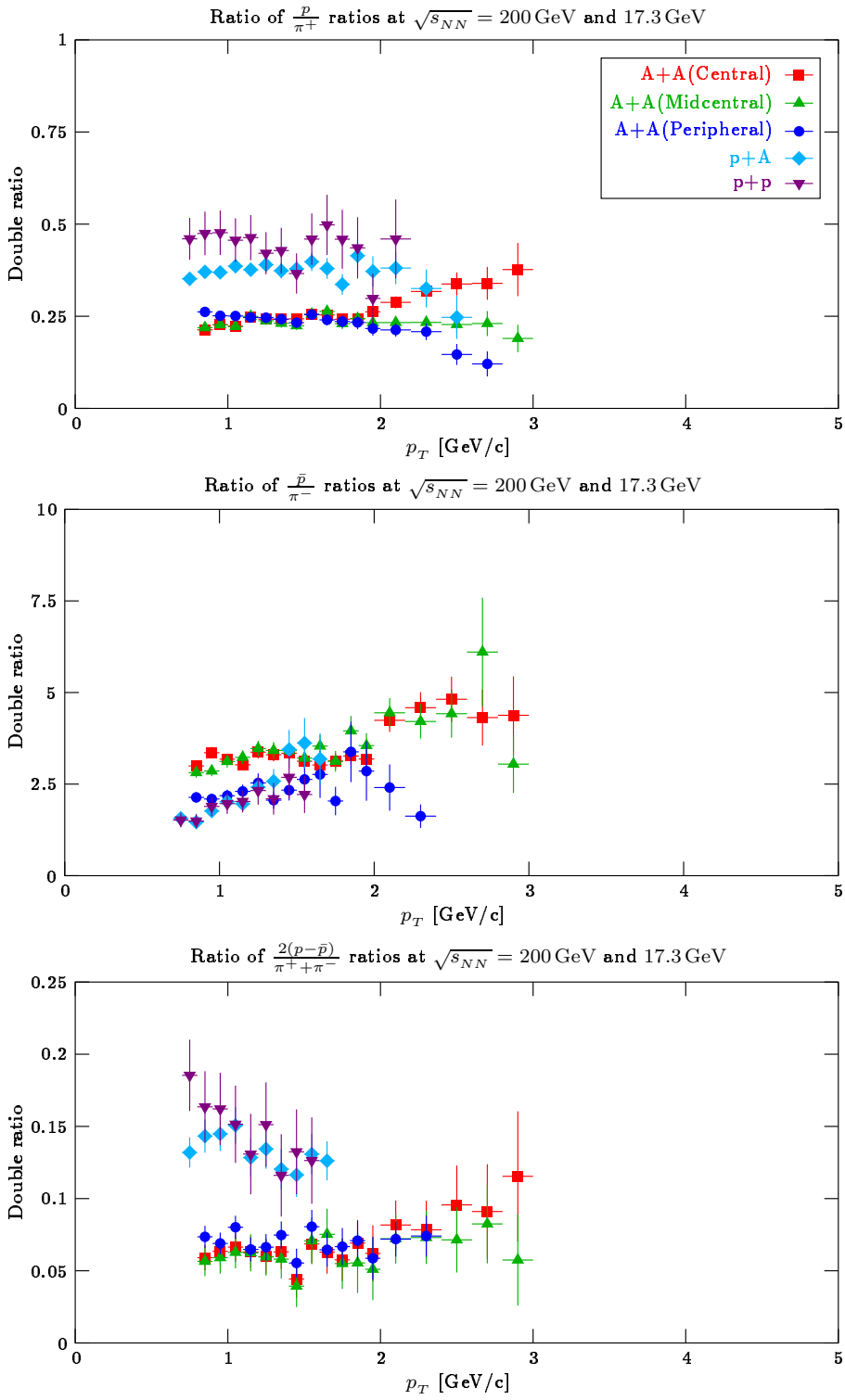

Figure 50: Ratio of proton/pion, anti-proton/pion and net-proton/pion ratios at $\sqrt{s_{NN}} = 200\,\text{GeV}$ and $\sqrt{s_{NN}} = 17.3\,\text{GeV}$ collision energy.

mechanism. A perturbative QCD based particle production mechanism would suggest scaling with the number of binary nucleon-nucleon collisions (calculable from geometric Monte Carlo models), as in a partonic picture, the particles are produced by the binary parton-parton reactions, the number of which being a constant multiple of the number of nucleon-nucleon binary collisions, where the unknown constant multiplier cancels in the $\langle N_{BC} \rangle (C + D) / \langle N_{BC} \rangle (A + B)$ ratio of the number of binary nucleon-nucleon collisions. The basic idea of using the nuclear modification factor for testing in-medium modification is that if the assumed particle production scheme holds, and there is an in-medium modification effect, the nuclear modification factor shall be different from unity.

There are certain difficulties in working with nuclear modification factors. These are mainly posed by the lack of knowledge on the relevant elementary particle production mechanism, which should provide the appropriate scaling factor. As discussed, a partonic picture would suggest binary collision scaling. However, a typical soft production scheme would suggest different scaling. Consider for example, that the particle production is governed by a nuclear resonance decay picture. In this case, the incoming nucleons are excited in the first collision (becoming so called 'wounded nucleons'), propagate through the medium, and subsequently decay. In this case, the scaling factor should be the number of wounded nucleons.[25] To avoid a strong bias, introduced by the discussed model dependence, both extreme scaling scenarios, the binary collision scaling and the wounded nucleon scaling, are considered. The corresponding modification factors shall be discriminated by the superscripts ^{BC} and ^{W}, respectively.

The nuclear modification factors of proton(deuteron)-nucleus and nucleus-nucleus reactions relative to proton-proton are shown in Figure 51 and Figure 52, with binary collision and with wounded nucleon scaling, respectively. The p+W/p+p data from [20], measured at $s_{NN} = 19.4\,\mathrm{GeV}$, are also shown for consistency check.

Assuming binary scaling (Figure 51), the proton(deuteron)-nucleus curve starts from below one, and exceeds unity above about $p_T = 1.5\,\mathrm{GeV/c}$, meaning a particle yield excess at high p_T, at both energies. The nucleus-nucleus curve, however, stays below unity at RHIC energies for $\pi^{\pm}, K^{\pm}$ particles, and start to even decrease above about $p_T = 1.5\,\mathrm{GeV/c}$ ('high p_T particle suppression'). The $p, \bar{p}$ curves do not show a suppression at RHIC energy at high p_T, but they stay below the proton(deuteron)-

[25] The wounded nucleon scaling successfully describes multiplicity distributions and particle spectra in d+Au collisions, as discussed in [27, 28]. It is widely believed, that at low p_T, the particle spectra scale with the number of wounded nucleons. This picture is also supported by the observed wounded nucleon scaling of the total multiplicities.

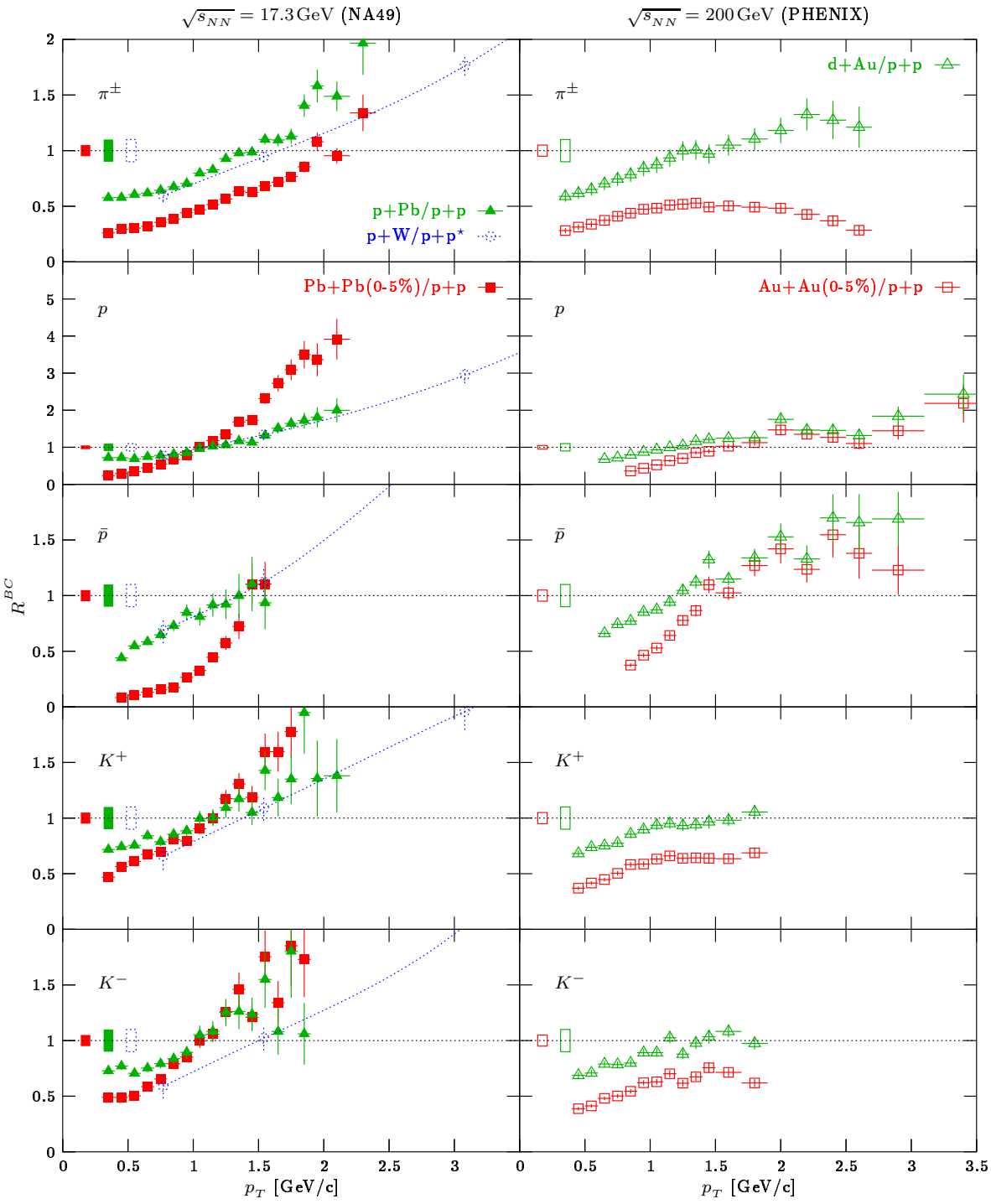

Figure 51: Pb+Pb(0-5%)/p+p and p+Pb/p+p nuclear modification factors at $y = 0$ in $\sqrt{s_{NN}} = 17.3\,\mathrm{GeV}$ collisions, with binary collision scaling. Similar data for $\sqrt{s_{NN}} = 200\,\mathrm{GeV}$ reactions are also shown. *: p+W/p+p data at $s_{NN} = 19.4\,\mathrm{GeV}$ from [20]. (Errorbars around unity indicate normalization errors.)

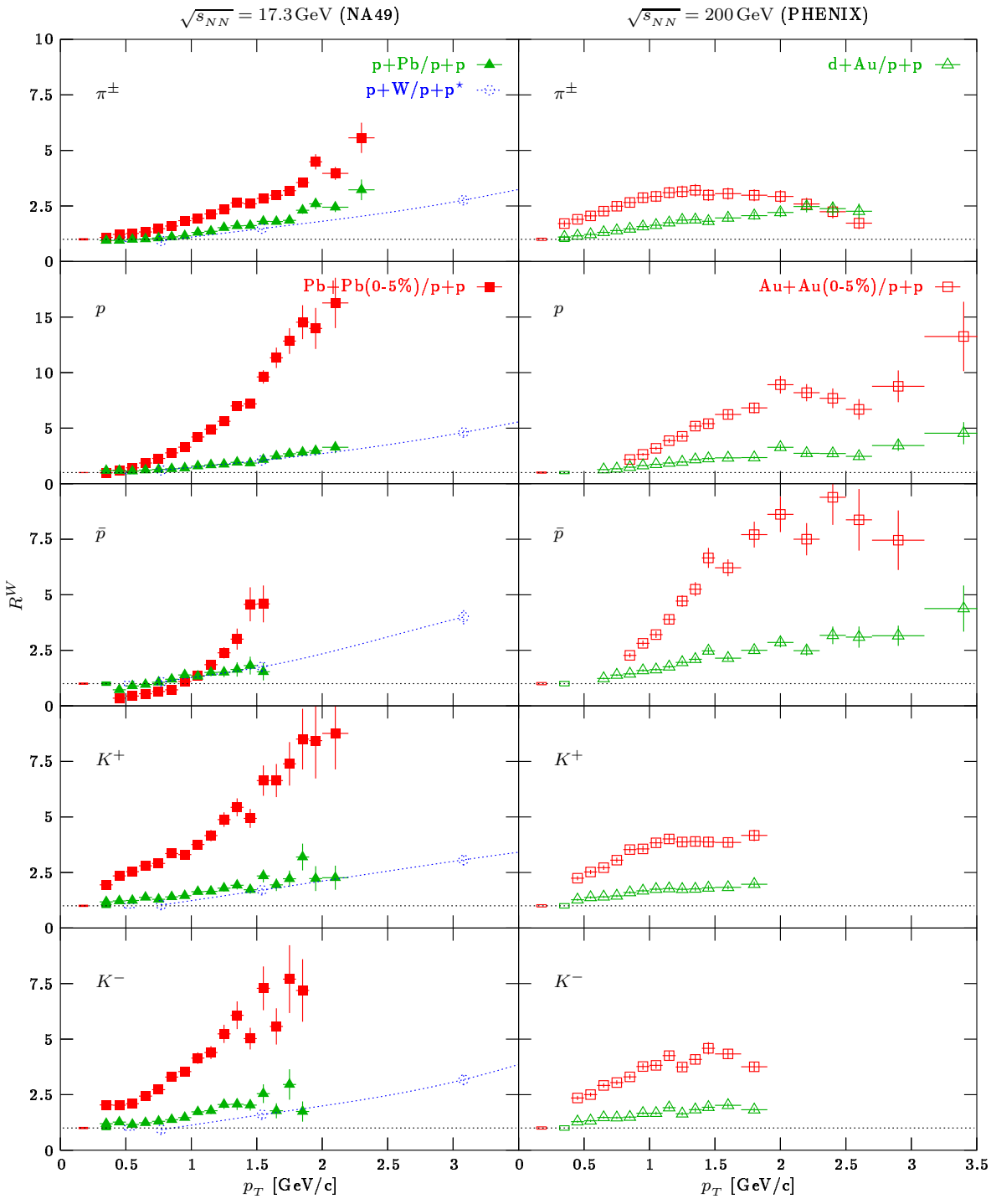

Figure 52: Pb+Pb(0-5%)/p+p and p+Pb/p+p nuclear modification factors at $y = 0$ in $\sqrt{s_{NN}} = 17.3\,\mathrm{GeV}$ collisions, with wounded nucleon scaling. Similar data for $\sqrt{s_{NN}} = 200\,\mathrm{GeV}$ reactions are also shown. *: p+W/p+p data at $s_{NN} = 19.4\,\mathrm{GeV}$ from [20]. (Errorbars around unity indicate normalization errors.)

nucleus curves. The p_T evolution of the corresponding SPS energy curves are largely different. Neither curve shows a suppression at high p_T: there is a strong excess in each particle channel. The nucleus-nucleus curves are bound by the proton-nucleus meson curves ($\pi^{\pm}, K^{\pm}$), whereas the $p, \bar{p}$ curves of the nucleus-nucleus reaction shows an excess over proton-nucleus at high p_T. The consistency to the similar energy ($s_{_{NN}} = 19.4\,\mathrm{GeV}$) p+W/p+p measurement of [20] is good, however there is a clear difference for the $\pi^{\pm}, K^{\pm}$ particles. This is explained by the strong energy dependence of the particle production in p+p at the low collision energies is in question (see also [45], or [46] Figure 4), due to the closeness of the momentum space boundary.

In the wounded nucleon scaling picture (Figure 52), the nucleus-nucleus particle yields are in excess over the proton(deuteron)-nucleus, for all produced particles, on the whole p_T region, for both extreme collision energies.

The particle excess of proton(deuteron)-nucleus relative to scaled proton-proton reactions is often referred to as the 'Cronin effect'. Its qualitative explanation in a partonic picture is given by the initial multiple scattering of partons, transferring momentum from the longitudinal degrees of freedom to the transverse degrees of freedom. In a soft production picture (e.g. nuclear resonance scheme) the explanation would be similar: the momentum of the wounded nucleon is modulated by the further collisions in the medium, which would also transfer momentum from the longitudinal degrees of freedom to the transverse degrees of freedom. Both processes should also be present in nucleus-nucleus collisions, therefore when seeking for signatures of high p_T particle suppression, the suppression of nucleus-nucleus yields should be taken relative to the proton(deuteron)-nucleus yields. The nuclear modification factors with proton(deuteron)-nucleus reference spectrum are shown in Figure 53.

The nuclear modification factors, with proton(deuteron)-nucleus reference spectrum, show the following properties. When assuming binary collision scaling (Figure 53 left column), the meson ratios both at SPS and at RHIC are very similar at low p_T. The $\pi^{\pm}$ modification curve also stays below one at SPS energy, however, the RHIC curve shows far larger suppression. The p and $\bar{p}$ RHIC curves show a saturation to unity from below, whereas the SPS $p, \bar{p}$ curves go above one. When assuming wounded nucleon scaling (Figure 53 right column), the remarkable relations between the modification curves at the two energies are: the p modification at SPS energy shows an excess over RHIC modification, which can be explained by the much higher net-baryon rapidity density at SPS, and the $K^{\pm}$ modification curves at SPS also bound the RHIC curves, showing a stronger strangeness enhancement with larger system size at SPS

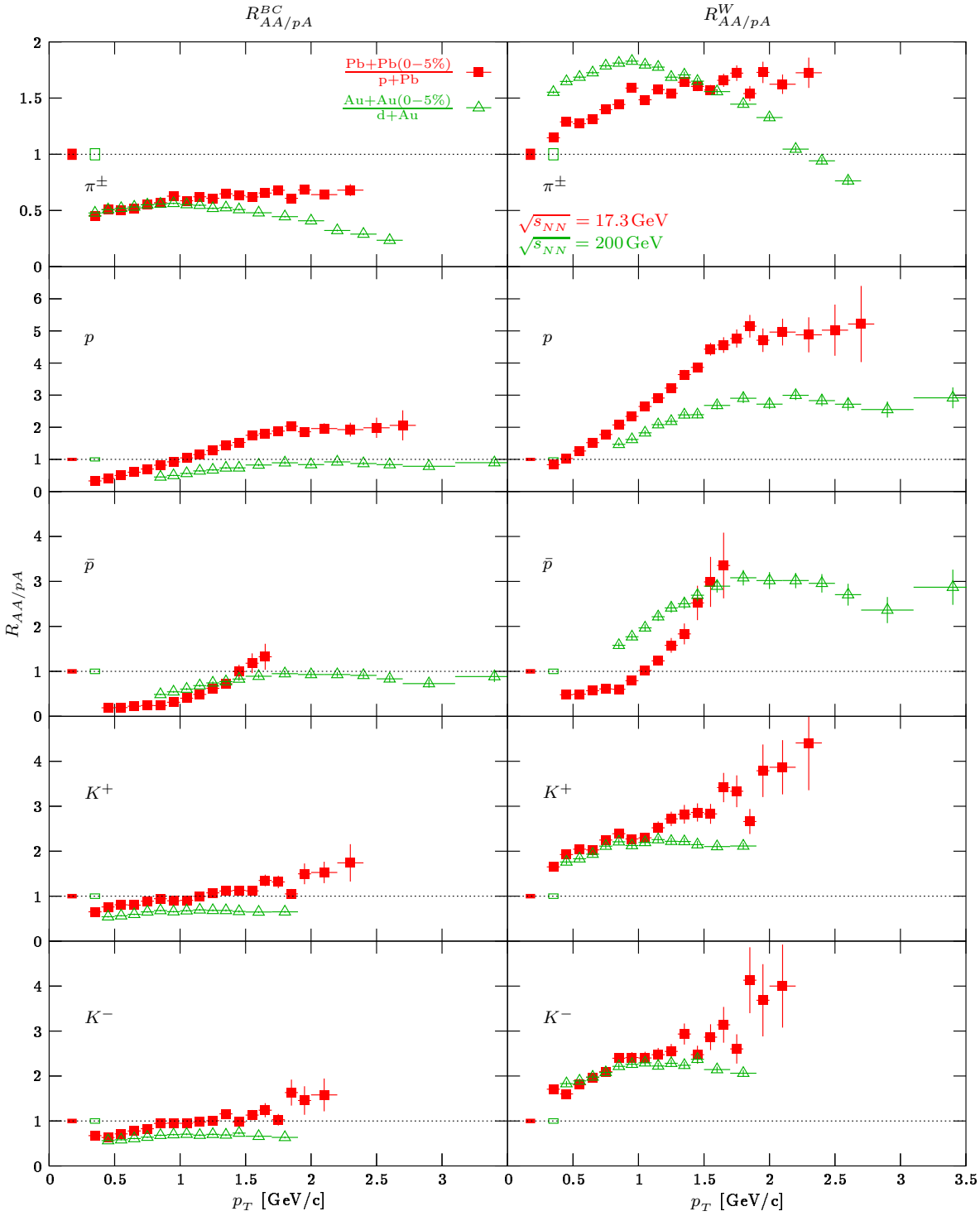

Figure 53: Pb+Pb(0-5%)/p+Pb nuclear modification factors at $y = 0$ in $\sqrt{s_{NN}} = 17.3\,\mathrm{GeV}$ collisions. Similar data for $\sqrt{s_{NN}} = 200\,\mathrm{GeV}$ reactions are also shown. (Errorbars around unity indicate normalization errors.)

energy than at RHIC. The large difference between the net-baryon rapidity density of the RHIC and SPS energy nucleus-nucleus and proton(deuteron)-nucleus reactions makes the comparison of the p curves very hard. Also the relevance of the asymmetry of the proton(deuteron)-nucleus reactions is hard to judge. Therefore, a similar quantity, the central to peripheral nuclear modification ratio, the R_{CP}, is also extracted from the data. In this case, peripheral nucleus-nucleus collisions are taken as reference data, which has the advantage, that peripheral nucleus-nucleus collisions are symmetric reactions, but in other means they are very similar to proton(deuteron)-nucleus collisions. The nuclear modification factors R_{CP} are shown in Figure 54.

The central to peripheral nuclear modification factors are observed to have the following energy dependence properties. When assuming binary collision scaling (Figure 54 left column), the modification curves at SPS and RHIC energy are surprisingly similar. The only visible difference is the behavior of the $\bar{p}$ curve, and that for $\pi^{\pm}$, the amount of suppression is much smaller at SPS. When using wounded nucleon scaling (Figure 54 right column), these spectacular similarities seem to be reduced, however the p modification curve at the two energies remains very similar. Summarizing the results on the energy dependence of the nuclear modification factors: provided that the particle spectra scale with the number of binary collisions, the A+A(Central)/p+A and the A+A(Central)/A+A(Peripheral) nuclear modification factors show a similar (particle type dependent) suppression pattern at SPS and at RHIC energies, however the amount of $\pi^{\pm}$ suppression at high p_T is significantly smaller at SPS. The asymptotic behavior of the modification factors are not clear due to the small statistics of the reference p+p, p+Pb or Pb+Pb(Peripheral) data at SPS. Also, the validity of binary collision scaling is not justified. The interest in the asymptotic behavior of the nuclear modification factors initiated further measurements: the most recent CERN experiment, the NA61 (a continuation of NA49), has begun its first data taking period, and shall continue to take data in the future. An important motivation for this new experiment was the extension of the p_T domain for modification factor measurements at SPS energy, and was partly initiated by the author [17, 18, 19, 46].

The comparison to the perturbative QCD based energy loss calculation shows a good agreement to the data, except for p and $\bar{p}$. The former may be explained by the high net-baryon density around midrapidity, the transfer of which is not necessarily described by perturbative QCD. The good agreement to the nuclear modification data is surprising, as the perturbative QCD based model seemed to fail in describing important features of the data, namely the production of K^- and $\bar{p}$ relative to π^-.

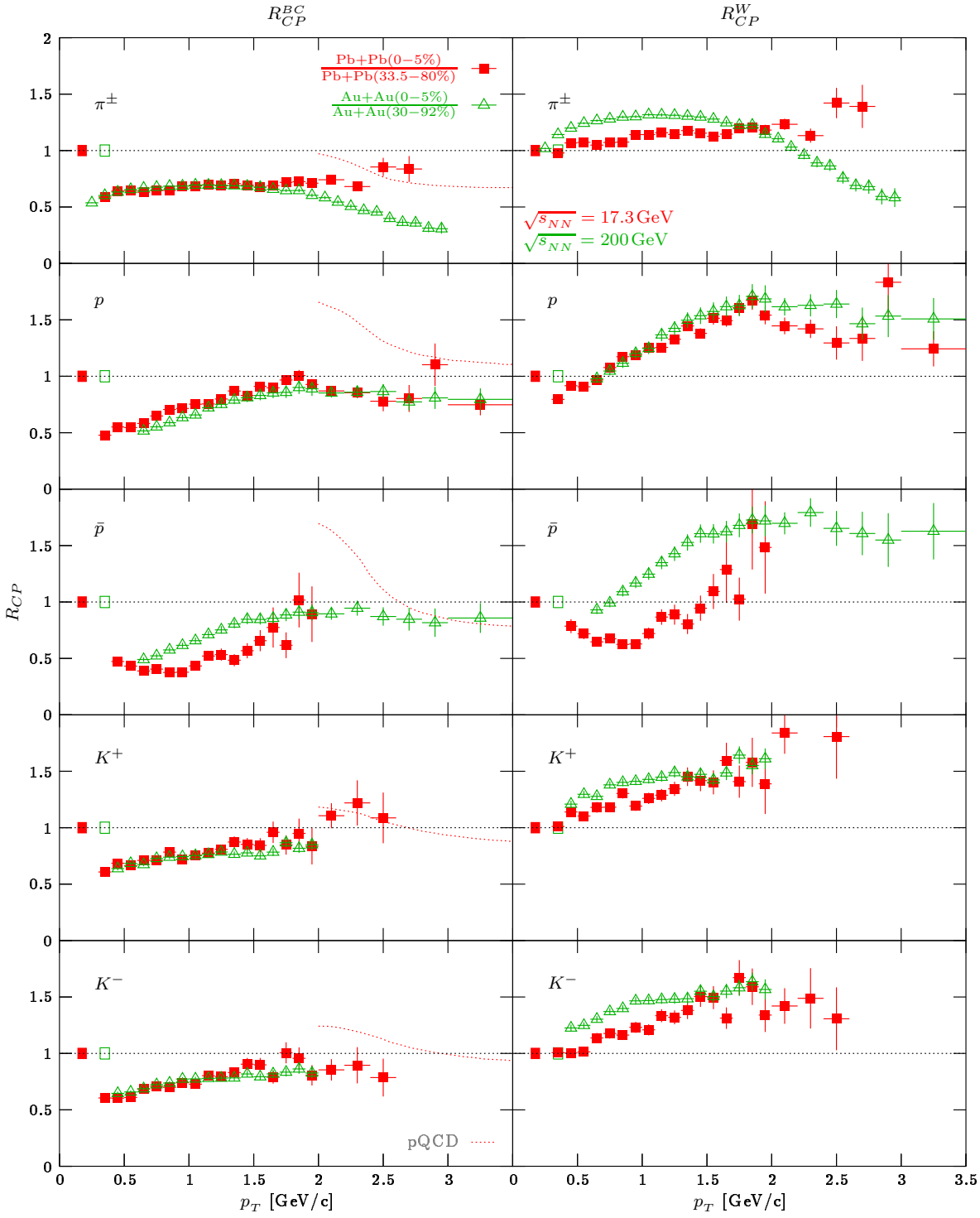

Figure 54: Pb+Pb(0-5%)/Pb+Pb(33.5-80%) nuclear modification factors at $y = 0$ in $\sqrt{s_{NN}} = 17.3\,\mathrm{GeV}$ collisions. Similar data for $\sqrt{s_{NN}} = 200\,\mathrm{GeV}$ reactions are also shown. pQCD: perturbative QCD calculation. (Errorbars around unity indicate normalization errors.)

An outlook to further high p_T measurements at SPS energy has been presented in [57], which could extend the studies also to the sub-inclusive level (correlation studies). The preliminary result, presented in [57] indicates qualitatively similarly structures to the observations in Figure 5.

Acknowledgments

I would like to express my gratitude to Dezső Varga and Ferenc Siklér for help in innumerable technical questions.

I would like to thank Daniel Barna for the universal data visualizer program package, the BLOP (`http://blopplot.sourceforge.net`): it was of great use during the analysis.

I would like to thank to the LHC Computing Grid crew at Budapest, in particular to Kálmán Kővári, Gergely Debreczeni, Szabolcs Hernáth, Edit Kárász and Max Berger, for the LCG infrastructure, the use of which was essential for this analysis.

I would like to thank to the full NA49 Collaboration, in particular to the 'young generation', Tim Schuster, Michael Mitrovski, Peter Dinkelaker, Benjamin Lungwitz, Claudia Höhne, Christoph Blume etc., for their help in solving many technical issues, and for having good discussions. I would also like to thank to the 'senior generation', Peter Seyboth (spokesman), Marek Gazdzicki, Herbert Ströbele, Helena Bialkowska etc., for the interesting discussions, and for the innumerable corrections of manuscripts.

I would also like to thank to György Vesztergombi, my supervisor, and to Zoltán Fodor for the opportunity of participating in this interesting experiment.

I would like to thank to Tamás Matolcsi for reading and correcting the manuscript of the article about the iterative unfolding method.

Last, but not least, I would like to thank to my family for their patience, encouragement and support.

Many other people, who may not be mentioned here, also deserve my acknowledgments for their help.

This work was supported by the Hungarian Scientific Research Fund (OTKA 68506). The work concerning the iterative unfolding method was also supported by the Hungarian Scientific Research Fund, but under a different contract (OTKA T048898). Special thanks to Ferenc Siklér for this support.

A Kinematic Variables and Particle Distributions

This section describes the used kinematic notations and conventions. In the followings, m shall denote particle mass, and c will be the speed of light. The coordinate axis directions shall be the following: z shall be the direction of the collision axis (beam axis, longitudinal direction), while x and y are perpendicular to z (transverse directions) and to each other. The orientation of the coordinate system is chosen to be positive. The outline of the coordinate direction choices is shown in Figure 55. The large arrows show the direction of the momenta of the colliding particles, and the marks L and T indicate the longitudinal or transverse character of the coordinate axes. The θ and φ symbols mean polar angles in the longitudinal and transverse plane, respectively (φ shall be also referred as azimuth).

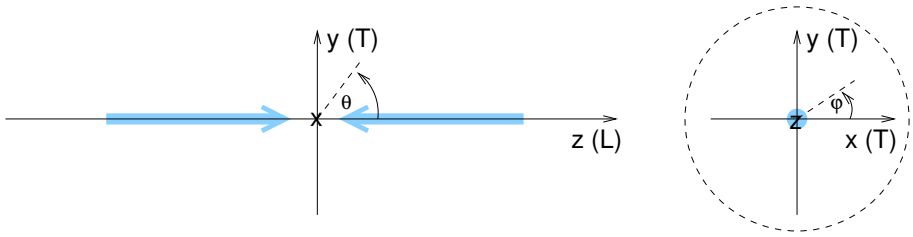

Figure 55: The schematic of the used coordinate axis convention.

If the coordinate components of a particle momentum $\vec{p}$ are (p_x, p_y, p_z), then the longitudinal momentum is defined to be $p_L = p_z$, the transverse momentum is defined to be $p_T = \sqrt{p_x^2 + p_y^2}$, and the momentum magnitude is $p = \sqrt{p_L^2 + p_T^2}$, while its energy is $E = \sqrt{m^2\mathrm{c}^4 + p^2\mathrm{c}^2}$. The quantity, called transverse energy, is defined as $E_T := \sqrt{m^2\mathrm{c}^4 + p_T^2\mathrm{c}^2}$ (sometimes, a similar quantity, called transverse mass, is used instead: $m_T := E_T/\mathrm{c}^2$). The rapidity of the particle in a direction $\vec{n}$ (being a unit vector) is defined to be $\omega_{\vec{n}} := \operatorname{atanh}\left(\frac{\vec{n}\cdot\vec{p}\,\mathrm{c}}{E}\right)$. If $\vec{n}$ corresponds to the unit vector in the z direction, then this quantity is called longitudinal rapidity (or simply rapidity), and is denoted by y. Useful formulae are $y = \operatorname{atanh}\left(\frac{p_L\mathrm{c}}{E}\right) = \frac{1}{2}\ln\left(\frac{E+p_L\mathrm{c}}{E-p_L\mathrm{c}}\right) = \ln\left(\frac{E+p_L\mathrm{c}}{E_T}\right)$, and $E = E_T\cosh y, \;\; p_L = E_T/\mathrm{c}\,\sinh y$. A Lorentz boost in the longitudinal direction by a rapidity value Δy leaves the coordinates of the transverse plane intact, and the transformation of the (longitudinal) rapidity coordinate is simply a translation by Δy. The y quantity in the $m = 0$ limit may be written as $\eta := y_{m=0} = \operatorname{atanh}\cos\theta = -\ln\tan\frac{\theta}{2}$, and is called pseudorapidity. It is seen that when $p \gg m\mathrm{c}$, $y \approx \eta$ follows, thus the particle rapidity in the large momentum limit only depends on the emission angle θ.

If the four momenta of the colliding particles are $(E_1, \vec{p}_1)$ and $(E_2, \vec{p}_2)$, then the collision energy in the center of mass system[26] corresponds to the Minkowski pseudolength of the summed four momenta of the system: $E_{\mathrm{cm}} = \sqrt{(E_1+E_2)^2 - (\vec{p}_1+\vec{p}_2)^2\mathrm{c}^2}$, which is also denoted by $\sqrt{s}$. If the colliding systems are composite, and the binding energy of the systems are much smaller than the collision energy, the collision energy of the constituent pairs is the good measure of the hardness of the reaction, instead of the collision energy of the composite systems. Such situations are high energy nuclear collisions, where the hardness of the reaction is characterized by the collision energy per colliding nucleon pairs: $\sqrt{s_{_{NN}}}$, where the two nucleus are considered as a collection of free nucleons, travelling with the same velocity.

A further commonly used longitudinal coordinate is the Feynman x variable, $x_{_F} = \frac{p_L}{p_{L\max}}$, where the momentum components are understood to be in the center of mass frame of the colliding particles. If the masses of the colliding particles are m_1 and m_2, respectively, then

$$p_{L\max} = \frac{1}{\mathrm{c}}\sqrt{\left(\frac{1}{2}\sqrt{s}\right)^2 - \frac{1}{2}(m_1^2+m_2^2)\mathrm{c}^4 + \left(\frac{(m_1^2-m_2^2)\mathrm{c}^4}{2\sqrt{s}}\right)^2}.$$

In case of high energy nuclear collisions, $m_1 \approx m_2$ is the nucleon mass $m_{_N}$, thus $p_{L\max} \approx \frac{1}{\mathrm{c}}\sqrt{\left(\frac{1}{2}\sqrt{s}\right)^2 - m_{_N}^2\mathrm{c}^4}$. When the nucleon-nucleon collision energy is much higher than the nucleon mass, i.e. $\sqrt{s_{_{NN}}} \gg m_{_N}\mathrm{c}^2$ holds, then $p_{L\max} \approx \frac{1}{2}\sqrt{s_{_{NN}}}/\mathrm{c}$ follows.

The single particle production momentum distributions are measured by the invariant differential cross-sections. The invariant differential cross-section is defined by the invariant differential particle yield multiplied by the total cross-section of the process. The total cross-section is a normalization factor, and is defined to be the useful beam cross-section in the infinite beam size limit, assuming spatially homogeneous, monoenergetic beam. The invariant differential particle yield is the momentum density function of the particle production (per event), with respect to the Lorentz invariant volume measure of the mass shell of the produced particle.[27] The Lorentz invariant volume measure of the mass shell is

$$\frac{1}{E/\mathrm{c}}\,\mathrm{d}^3p = p_{_T}\,\mathrm{d}y\,\mathrm{d}p_{_T}\,\mathrm{d}\varphi = E_{_T}/\mathrm{c}\,\mathrm{d}y\,\mathrm{d}E_{_T}/\mathrm{c}\,\mathrm{d}\varphi = \frac{p_{_T}p_{L\max}}{E/\mathrm{c}}\,\mathrm{d}x_{_F}\,\mathrm{d}p_{_T}\,\mathrm{d}\varphi,$$

[26] The center of mass frame is defined by the condition, that the sum of the spatial momentum of the colliding particles is zero.

[27] The word 'invariant' refers to the convention of differentiating with respect to the Lorentz invariant measure.

as viewed in different parameterizations of the momentum space. Thus, the invariant differential particle yield is

$$E/\mathrm{c}\,\frac{\mathrm{d}^3n}{\mathrm{d}^3p} = \frac{1}{p_{_T}}\frac{\mathrm{d}^3n}{\mathrm{d}y\,\mathrm{d}p_{_T}\,\mathrm{d}\varphi} = \frac{1}{E_{_T}/\mathrm{c}}\,\frac{\mathrm{d}^3n}{\mathrm{d}y\,\mathrm{d}E_{_T}/\mathrm{c}\,\mathrm{d}\varphi} = \frac{E/\mathrm{c}}{p_{_T}p_{L\max}}\,\frac{\mathrm{d}^3n}{\mathrm{d}x_{_F}\,\mathrm{d}p_{_T}\,\mathrm{d}\varphi},$$

as viewed in different parameterizations of the momentum space, n meaning the number of particles per event (of the type of interest). For an unpolarized beam, the single particle production is axially symmetric, thus the φ coordinate may be suppressed: the single particle distributions do not depend on that coordinate.

It is observed, that in nuclear reactions, the particle distributions

$$(y, p_{_T}) \mapsto \frac{1}{2\pi\cdot p_{_T}}\cdot\frac{\mathrm{d}^2n}{\mathrm{d}y\,\mathrm{d}p_{_T}}$$

are approximately flat in y at $y = 0$ in the center of mass system, i.e. at midrapidity.[28] Viewed from a frame, moving parallel to the beam axis with a rapidity value y_0, the particle distribution function is the same, but translated by y_0, i.e. midrapidity corresponds to $y = y_0$. Changing coordinates to $(\eta, p_{_T})$, this may be written as

$$(\eta, p_{_T}) \mapsto \frac{E_{_T}/\mathrm{c}\sqrt{1+\left(\frac{p_{_T}\sinh\eta}{E_{_T}/\mathrm{c}}\right)^2}}{p_{_T}\cosh\eta}\cdot\frac{1}{2\pi\cdot p_{_T}}\cdot\frac{\mathrm{d}^2n}{\mathrm{d}\eta\,\mathrm{d}p_{_T}},$$

where η and y now are understood in the moving frame. In the large momentum limit, η approximates y and the Jacobi determinant $\frac{p_{_T}\cosh\eta}{E_{_T}/\mathrm{c}\sqrt{1+\left(\frac{p_{_T}\sinh\eta}{E_{_T}/\mathrm{c}}\right)^2}}$ approximates 1, so it may be omitted. According to the previous statement: the distribution

$$(\eta, p_{_T}) \mapsto \frac{1}{2\pi\cdot p_{_T}}\cdot\frac{\mathrm{d}^2n}{\mathrm{d}\eta\,\mathrm{d}p_{_T}}$$

is flat in η around $\eta \approx y_0$. If the longitudinal coordinate is changed to the θ polar angle (also measured in the moving frame), the production momentum density becomes

$$(\theta, p_{_T}) \mapsto \frac{2\tan(\theta/2)}{1+\tan^2(\theta/2)}\cdot\frac{1}{2\pi\cdot p_{_T}}\cdot\frac{\mathrm{d}^2n}{\mathrm{d}\theta\,\mathrm{d}p_{_T}},$$

which (according to our previous observation) should be flat around midrapidity, i.e. around $\theta = 2\arctan\exp(-y_0)$. The Jacobi determinant $\frac{1+\tan^2(\theta/2)}{2\tan(\theta/2)}$ has a flat minimum

[28] The $y = 0$ coordinate slice in the center of mass system is often referred to as 'midrapidity'.

at $\theta = 90°$, and tends rapidly to infinity at $\theta = 0°, 180°$. Thus the particle number density

$$(\theta, p_T) \mapsto \frac{1}{2\pi \cdot p_T} \cdot \frac{\mathrm{d}^2 n}{\mathrm{d}\theta \, \mathrm{d}p_T}$$

is flat around $\theta = 2 \arctan \exp(-y_0)$ (corresponding to midrapidity), if $y_0 = 0$. However, if y_0 takes a large value, then the Jacobi determinant takes a large value and has a large derivative at $\theta = 2 \arctan \exp(-y_0)$, thus the particle number density in θ becomes large and rapidly varying with θ, for midrapidity particles. This implies that in collider experiments (which correspond to the $y_0 = 0$ case), the particle track density observed in the laboratory frame, is minimal and slowly varying with θ around midrapidity, while in fixed target setups (large y_0 value), the particle track density can be very high and rapidly varying with the θ angle, for midrapidity tracks. Due to this high particle track density in coordinate space around midrapidity, the track reconstruction in fixed target experiments has to deal with a much higher background, caused by the crossing tracks and by the high population of the detector volume.

B π^0 Spectra and a Robust Unfolding Method

Besides the measurement of charged particle spectra, the spectrum of neutral particles, especially of neutral mesons like π^0, are also of interest. However, in some experimental setups, like NA49, the detection of π^0 particles is not straightforward. The π^0 particles are most commonly detected via their decay channel $\pi^0 \rightarrow \gamma\gamma$ (98.798% branching ratio), or more rarely via the Dalitz decay channel $\pi^0 \rightarrow \gamma e^+e^-$ (1.198% branching ratio). In dedicated π^0 experiments, the particles are reconstructed by pairing the γ momenta[29] in all possible combinations in an event, and by calculating the mass of the two-γ system. The erroneously paired unrelated γ background is simulated via taking γ-s from separate events (event mixing technique), and this simulated background is then subtracted. There can be some circumstances, when this direct method is not usable. A possible reason can be limited γ detection acceptance or efficiency. The former simply arises from low geometrical coverage, while the latter may be a result of high population of the detector volume (e.g. in heavy-ion events), or can be a feature of the applied γ detection technique. If for any of the previous reasons, the γ detection probability is low, the π^0 detection probability will be even worse, as the detection of two valid γ signals is necessary. Therefore, experiments already in the 1970's became interested in the development of such methods, which could obtain the π^0 momentum distribution from the measured single γ momentum distribution, assuming that the main source of the γ particles are π^0 decays (in fact, this assumption is valid to a reasonable accuracy). Such a method was proposed in [33], which at the price of two approximations, provides a formula to obtain the π^0 spectrum from the γ spectrum. However, the nature of the two approximations is quite unclear, which makes this method quite ill defined. In fact, it shall be shown on realistic toy examples, that this method gives wrong answer: it does not correctly reconstruct the input π^0 spectrum from the generated γ spectrum.

In NA49, the γ detection can be performed by using $\gamma \rightarrow e^+e^-$ conversion in the target material, the probability of which turned out to be about 1% for the used Pb target. The γ-s are detected by pairing the e^+, e^- tracks with all possible combinations in an event, and the combinatorial background is subtracted by the event mixing technique as in the π^0 case. The π^0 particles can be reconstructed by pairing the γ candidates, and also subtracting the combinatorial background, obtained via event mixing. However, due to the low γ detection probability (below 1%), the π^0 detection

[29] The γ-s are usually detected by calorimeters.

probability becomes very low (below 0.01%), which reduces the statistics of detectable π^0 particles, as is shown in Figure 56. It is seen, that the available π^0 statistics, extracted by this direct method, is highly not enough to record a momentum distribution. To overcome this problem, a method which reconstructs the π^0 momentum distribution from the single γ momentum distribution would be of great use. As shall be shown, it turned out, that the method, proposed in [33] is not completely correct. Therefore, an other approach was developed by us, based on an iterative unfolding method, which also can be used quite generally in signal processing (the description of our method has been published in [41]). Although it turned out in the end, that even with this indirect method, the detectable π^0 statistics of NA49 would not be enough to go beyond $2\,\mathrm{GeV/c}$ in transverse momentum, the introduced method is interesting for future experiments, and can be of general interest in signal processing. A possible future application can be the CMS experiment, where the method can be applied in those regions of the momentum space, where the γ detection probability is not high enough to use the direct π^0 detection method.

To formulate our indirect method, first one has to recognize that the γ momentum density function $\vec{k} \mapsto \rho_\gamma(\vec{k})$ can be written as a folding of the initial π^0 momentum density function $\vec{p} \mapsto \rho_{\pi^0}(\vec{p})$ by a known conditional probability density function $(\vec{k}, \vec{p}) \mapsto \rho_{\pi^0 \to \gamma\gamma}(\vec{k}|\vec{p})$:

$$\rho_\gamma(\vec{k}) = \int \rho_{\pi^0 \to \gamma\gamma}(\vec{k}|\vec{p})\ \rho_{\pi^0}(\vec{p})\ \mathrm{d}^3p,$$

where the conditional probability density function $\rho_{\pi^0 \to \gamma\gamma}$ is known from kinematics. To obtain the initial probability density function ρ_{π^0}, one has to invert this integral operator. The inversion (i.e. unfolding) of such integral operators is of general interest in signal processing, however there is no known generally applicable method for such a problem. We proposed an iterative method, for which in some quite general cases, convergence to the initial probability density function could be proved. For detailed description of the developed unfolding method, we refer to [41], where also some quite general convergence criteria are shown.

The iteration scheme is defined as follows. Let A_ρ denote the folding operator by a conditional probability density function ρ, and f be the initial probability density function of interest, furthermore let $g := A_\rho f$ be the folded (i.e. measured) probability density function. The n-th order approximation of f is obtained by:

$$f_0 := g, \quad f_{n+1} := f_n + (f_0 - A_\rho f_n).$$

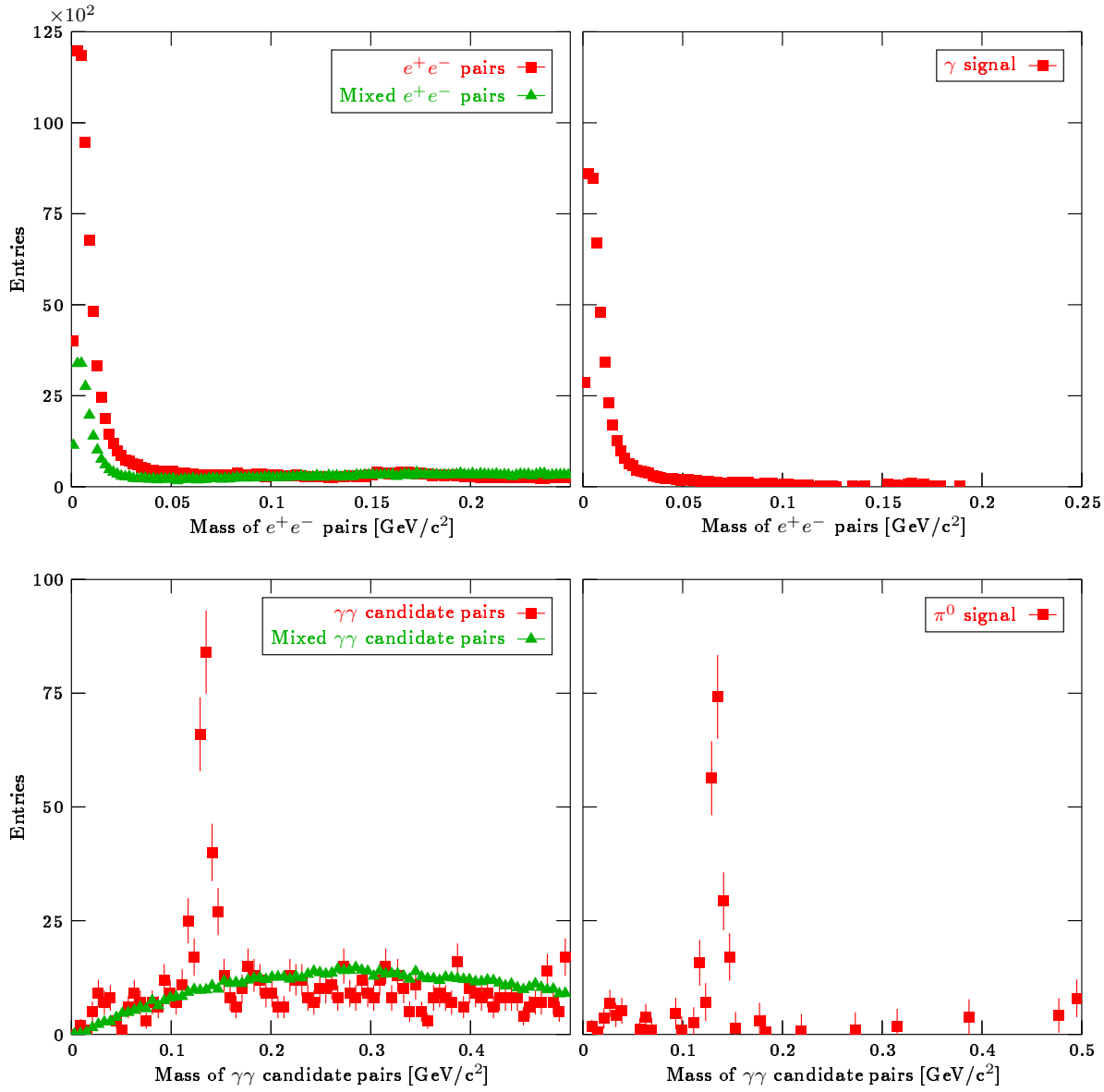

Figure 56: The mass spectrum of γ particles, reconstructed from e^+, e^- track pairs (upper panels), and of π^0 particles, reconstructed from $\gamma\gamma$ candidate pairs (lower panels), in p+Pb events.

One main result in the paper [41] is, that if the folding operator is a convolution, then this iteration always can be made convergent to the input probability density function f by folding g first with the reflected version of the convolution operator, and then by applying the iteration scheme for the obtained double convolution problem. A second main result is, that even if the folding operator is more general than a convolution, a quantity called Cauchy index can be used to test the convergence. This test shows that in the π^0 unfolding case, the proposed iterative scheme can be used to invert this

integral operator.

To show the performance of the method, a toy example π^0 unfolding problem is presented in Figure 57. The top left panel shows the input π^0 distribution together with the resulting γ distribution. In the top right panel, the input π^0 distribution is shown together with the unfolded π^0 distribution. Good agreement can be seen. In the middle left and right panels, the input π^0 distribution, the resulting γ distribution, and the unfolded π^0 distribution is shown at the $\eta = 0$ and $\eta = 0.4$ slice. In the bottom panels, input π^0 distribution, the resulting γ distribution, and the unfolded π^0 distribution by the method proposed in [33] is shown at the $\eta = 0$ and $\eta = 0.4$ slice. It is seen that the method described in [33] does not reconstruct the correct input distribution, whereas the iterative unfolding method provides the right answer.

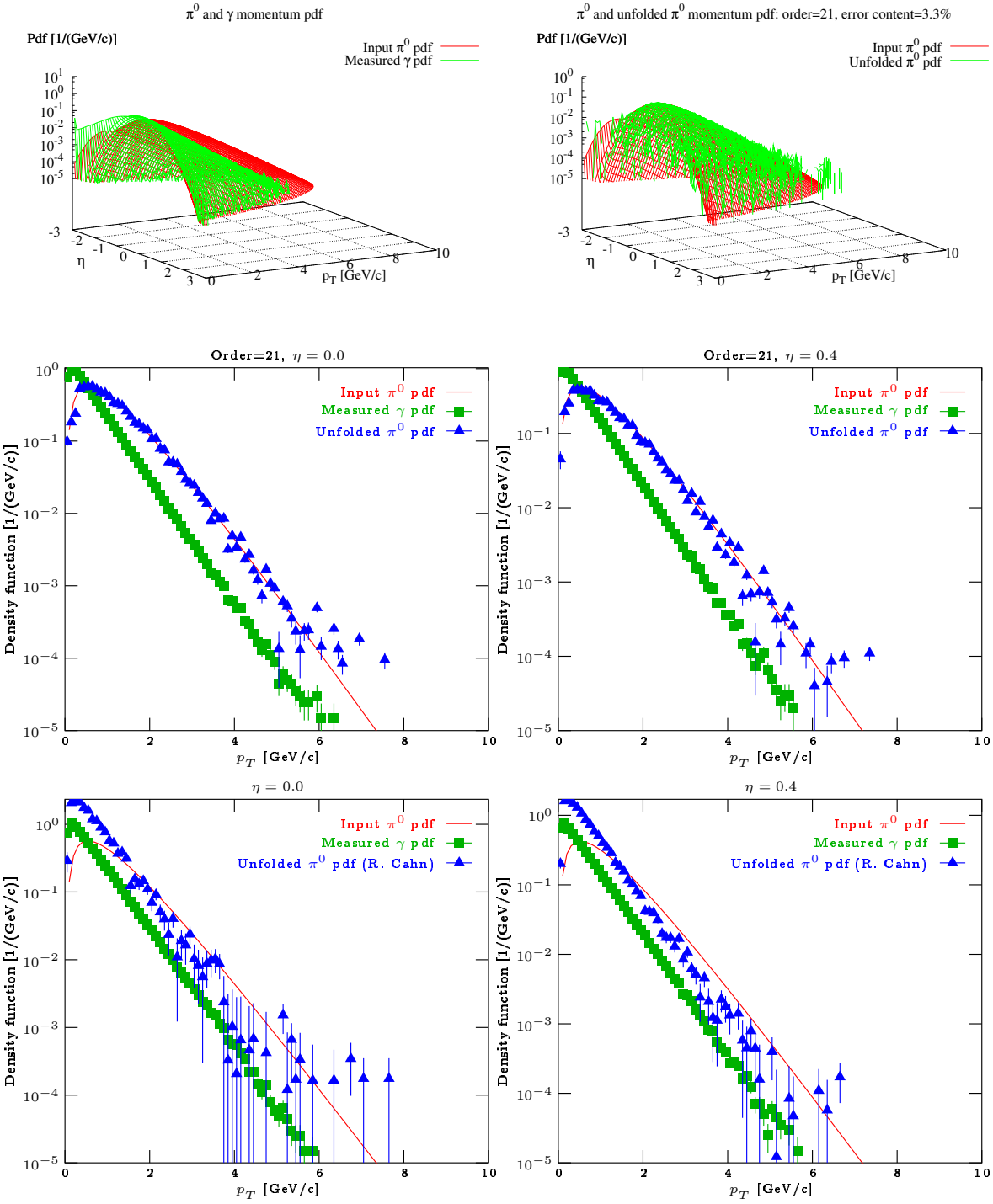

Figure 57: A toy example for testing the iterative unfolding method, proposed in [41], for the $\pi^0 \to \gamma\gamma$ problem. The bottom panels show the performance of the $\pi^0 \to \gamma\gamma$ unfolding method proposed in [33] (R. Cahn).

C Data Tables

Centrality	$\langle N_W \rangle$	$\langle N_P \rangle$	$\langle N_{BC} \rangle$	$\langle b \rangle$ [fm]
$0-5\%$	357 ± 1	385 ± 1	742 ± 3	2.309 ± 0.030
$5-12.5\%$	288 ± 2	343 ± 2	565 ± 5	4.460 ± 0.060
$12.5-23.5\%$	211 ± 3	280 ± 3	379 ± 8	6.444 ± 0.100
$23.5-33.5\%$	146 ± 4	215 ± 5	234 ± 9	8.139 ± 0.100
$33.5-43.5\%$	$87 \pm 7^\star$	$146 \pm 10^\star$	$120 \pm 13^\star$	$9.871 \pm 0.244^\star$
$43.5\%-80\%$	$40 \pm 4^\star$	$76 \pm 5^\star$	$46 \pm 5^\star$	$11.897 \pm 0.535^\star$
$33.5-80\%$	$56 \pm 7^\star$	$99 \pm 10^\star$	$70 \pm 13^\star$	$11.223 \pm 0.244^\star$

Centrality	$\sigma(N_W)$	$\sigma(N_P)$	$\sigma(N_{BC})$	$\sigma(b)$[fm]
$0-5\%$	22 ± 1	12 ± 1	68 ± 1	0.908 ± 0.010
$5-12.5\%$	28 ± 1	20 ± 1	78 ± 1	0.808 ± 0.005
$12.5-23.5\%$	30 ± 1	27 ± 1	75 ± 1	0.825 ± 0.005
$23.5-33.5\%$	25 ± 1	27 ± 1	57 ± 1	0.765 ± 0.005
$33.5-43.5\%$	$18 \pm 2^\star$	$23 \pm 2^\star$	$35 \pm 2^\star$	$0.693 \pm 0.030^\star$
$43.5\%-80\%$	$15 \pm 1^\star$	$24 \pm 2^\star$	$23 \pm 2^\star$	$0.981 \pm 0.040^\star$
$33.5-80\%$	$16 \pm 2^\star$	$24 \pm 2^\star$	$27 \pm 2^\star$	$0.896 \pm 0.040^\star$

Table 7: Average values and standard deviations of various collision parameters as a function of centrality in Pb+Pb collisions at $\sqrt{s_{NN}} = 17.3\,\mathrm{GeV}$. *: These values are semi-empiric averages, calculated on the full minimum-bias dataset, as discussed in the end of Section 3.1.2.

Centrality	$\langle N_W \rangle$	$\langle N_{BC} \rangle$
Full dataset	$5.58 \pm 1^\star$	$4.58 \pm 1^\star$

Table 8: Average values of various collision parameters in p+Pb reactions at $\sqrt{s_{NN}} = 17.3\,\mathrm{GeV}$. *: These values are semi-empiric averages, calculated on the full dataset, as discussed in Section 3.2.2.

p_T [GeV/c]	$\frac{1}{2\pi \cdot p_T} \cdot \frac{\mathrm{d}^2 n}{\mathrm{d}y\,\mathrm{d}p_T}\Big\|_{y=0}$ [1/(GeV/c)^2]					
	π^+	π^-	p	$\bar{p}$	K^+	K^-
0.05 ± 0.05	—	—	—	—	—	—
0.15 ± 0.05	—	—	—	—	—	—
0.25 ± 0.05	—	—	—	—	—	—
0.35 ± 0.05	$(1.071 \pm 0.018) \cdot 10^{+2}$	$(1.059 \pm 0.021) \cdot 10^{+2}$	$(8.569 \pm 0.138) \cdot 10^{+0}$	—	$(1.792 \pm 0.047) \cdot 10^{+1}$	$(1.174 \pm 0.036) \cdot 10^{+1}$
0.45 ± 0.05	$(6.426 \pm 0.138) \cdot 10^{+1}$	$(6.332 \pm 0.148) \cdot 10^{+1}$	$(8.271 \pm 0.140) \cdot 10^{+0}$	$(0.616 \pm 0.014) \cdot 10^{+0}$	$(1.415 \pm 0.042) \cdot 10^{+1}$	$(8.484 \pm 0.246) \cdot 10^{+0}$
0.55 ± 0.05	$(3.842 \pm 0.083) \cdot 10^{+1}$	$(3.445 \pm 0.059) \cdot 10^{+1}$	$(7.374 \pm 0.115) \cdot 10^{+0}$	$(0.503 \pm 0.011) \cdot 10^{+0}$	$(9.965 \pm 0.251) \cdot 10^{+0}$	$(5.665 \pm 0.140) \cdot 10^{+0}$
0.65 ± 0.05	$(2.148 \pm 0.039) \cdot 10^{+1}$	$(2.105 \pm 0.037) \cdot 10^{+1}$	$(6.416 \pm 0.094) \cdot 10^{+0}$	$(0.413 \pm 0.009) \cdot 10^{+0}$	$(7.394 \pm 0.209) \cdot 10^{+0}$	$(4.103 \pm 0.106) \cdot 10^{+0}$
0.75 ± 0.05	$(1.319 \pm 0.022) \cdot 10^{+1}$	$(1.286 \pm 0.020) \cdot 10^{+1}$	$(5.777 \pm 0.087) \cdot 10^{+0}$	$(0.318 \pm 0.008) \cdot 10^{+0}$	$(5.011 \pm 0.114) \cdot 10^{+0}$	$(2.936 \pm 0.076) \cdot 10^{+0}$
0.85 ± 0.05	$(8.115 \pm 0.122) \cdot 10^{+0}$	$(8.008 \pm 0.117) \cdot 10^{+0}$	$(4.766 \pm 0.071) \cdot 10^{+0}$	$(0.240 \pm 0.007) \cdot 10^{+0}$	$(3.569 \pm 0.079) \cdot 10^{+0}$	$(1.978 \pm 0.045) \cdot 10^{+0}$
0.95 ± 0.05	$(5.128 \pm 0.079) \cdot 10^{+0}$	$(5.188 \pm 0.085) \cdot 10^{+0}$	$(3.731 \pm 0.053) \cdot 10^{+0}$	$(0.186 \pm 0.005) \cdot 10^{+0}$	$(2.363 \pm 0.048) \cdot 10^{+0}$	$(1.369 \pm 0.032) \cdot 10^{+0}$
1.05 ± 0.05	$(3.169 \pm 0.043) \cdot 10^{+0}$	$(3.254 \pm 0.054) \cdot 10^{+0}$	$(3.000 \pm 0.042) \cdot 10^{+0}$	$(0.154 \pm 0.004) \cdot 10^{+0}$	$(1.626 \pm 0.034) \cdot 10^{+0}$	$(0.897 \pm 0.019) \cdot 10^{+0}$
1.15 ± 0.05	$(2.054 \pm 0.034) \cdot 10^{+0}$	$(2.040 \pm 0.033) \cdot 10^{+0}$	$(2.287 \pm 0.031) \cdot 10^{+0}$	$(0.134 \pm 0.004) \cdot 10^{+0}$	$(1.099 \pm 0.026) \cdot 10^{+0}$	$(0.610 \pm 0.014) \cdot 10^{+0}$
1.25 ± 0.05	$(1.298 \pm 0.019) \cdot 10^{+0}$	$(1.296 \pm 0.020) \cdot 10^{+0}$	$(1.752 \pm 0.022) \cdot 10^{+0}$	$(0.969 \pm 0.026) \cdot 10^{-1}$	$(0.784 \pm 0.019) \cdot 10^{+0}$	$(0.415 \pm 0.009) \cdot 10^{+0}$
1.35 ± 0.05	$(0.879 \pm 0.014) \cdot 10^{+0}$	$(0.829 \pm 0.013) \cdot 10^{+0}$	$(1.387 \pm 0.025) \cdot 10^{+0}$	$(0.713 \pm 0.023) \cdot 10^{-1}$	$(0.557 \pm 0.015) \cdot 10^{+0}$	$(0.291 \pm 0.007) \cdot 10^{+0}$
1.45 ± 0.05	$(0.549 \pm 0.008) \cdot 10^{+0}$	$(0.525 \pm 0.007) \cdot 10^{+0}$	$(0.975 \pm 0.015) \cdot 10^{+0}$	$(0.562 \pm 0.018) \cdot 10^{-1}$	$(0.367 \pm 0.009) \cdot 10^{+0}$	$(0.190 \pm 0.004) \cdot 10^{+0}$
1.55 ± 0.05	$(0.352 \pm 0.005) \cdot 10^{+0}$	$(0.340 \pm 0.004) \cdot 10^{+0}$	$(0.742 \pm 0.010) \cdot 10^{+0}$	$(0.402 \pm 0.015) \cdot 10^{-1}$	$(0.260 \pm 0.007) \cdot 10^{+0}$	$(0.125 \pm 0.003) \cdot 10^{+0}$
1.65 ± 0.05	$(0.235 \pm 0.004) \cdot 10^{+0}$	$(0.221 \pm 0.003) \cdot 10^{+0}$	$(0.523 \pm 0.008) \cdot 10^{+0}$	$(0.316 \pm 0.012) \cdot 10^{-1}$	$(0.195 \pm 0.005) \cdot 10^{+0}$	$(0.807 \pm 0.017) \cdot 10^{-1}$
1.75 ± 0.05	$(0.157 \pm 0.003) \cdot 10^{+0}$	$(0.147 \pm 0.002) \cdot 10^{+0}$	$(0.400 \pm 0.007) \cdot 10^{+0}$	$(0.225 \pm 0.009) \cdot 10^{-1}$	$(0.137 \pm 0.003) \cdot 10^{+0}$	$(0.557 \pm 0.014) \cdot 10^{-1}$
1.85 ± 0.05	$(0.102 \pm 0.002) \cdot 10^{+0}$	$(0.956 \pm 0.016) \cdot 10^{-1}$	$(0.285 \pm 0.005) \cdot 10^{+0}$	$(0.150 \pm 0.006) \cdot 10^{-1}$	$(0.951 \pm 0.023) \cdot 10^{-1}$	$(0.393 \pm 0.011) \cdot 10^{-1}$
1.95 ± 0.05	$(0.675 \pm 0.012) \cdot 10^{-1}$	$(0.639 \pm 0.010) \cdot 10^{-1}$	$(0.183 \pm 0.003) \cdot 10^{+0}$	$(0.108 \pm 0.005) \cdot 10^{-1}$	$(0.666 \pm 0.018) \cdot 10^{-1}$	$(0.257 \pm 0.008) \cdot 10^{-1}$
2.10 ± 0.10	$(0.361 \pm 0.006) \cdot 10^{-1}$	$(0.353 \pm 0.005) \cdot 10^{-1}$	$(0.102 \pm 0.002) \cdot 10^{+0}$	$(0.534 \pm 0.024) \cdot 10^{-2}$	$(0.380 \pm 0.009) \cdot 10^{-1}$	$(0.145 \pm 0.004) \cdot 10^{-1}$
2.30 ± 0.10	$(0.162 \pm 0.003) \cdot 10^{-1}$	$(0.159 \pm 0.003) \cdot 10^{-1}$	$(0.500 \pm 0.009) \cdot 10^{-1}$	$(0.260 \pm 0.015) \cdot 10^{-2}$	$(0.183 \pm 0.006) \cdot 10^{-1}$	$(0.588 \pm 0.027) \cdot 10^{-2}$
2.50 ± 0.10	$(0.784 \pm 0.018) \cdot 10^{-2}$	$(0.707 \pm 0.016) \cdot 10^{-2}$	$(0.232 \pm 0.005) \cdot 10^{-1}$	$(0.119 \pm 0.009) \cdot 10^{-2}$	$(0.866 \pm 0.030) \cdot 10^{-2}$	$(0.302 \pm 0.017) \cdot 10^{-2}$
2.70 ± 0.10	$(0.372 \pm 0.012) \cdot 10^{-2}$	$(0.302 \pm 0.010) \cdot 10^{-2}$	$(0.114 \pm 0.003) \cdot 10^{-1}$	$(0.560 \pm 0.061) \cdot 10^{-3}$	$(0.398 \pm 0.020) \cdot 10^{-2}$	$(0.133 \pm 0.011) \cdot 10^{-2}$
2.90 ± 0.10	$(0.162 \pm 0.007) \cdot 10^{-2}$	$(0.151 \pm 0.007) \cdot 10^{-2}$	$(0.588 \pm 0.018) \cdot 10^{-2}$	$(0.298 \pm 0.041) \cdot 10^{-3}$	$(0.185 \pm 0.013) \cdot 10^{-2}$	$(0.679 \pm 0.069) \cdot 10^{-3}$
3.25 ± 0.25	$(0.461 \pm 0.023) \cdot 10^{-3}$	$(0.413 \pm 0.020) \cdot 10^{-3}$	$(0.182 \pm 0.006) \cdot 10^{-2}$	$(0.573 \pm 0.135) \cdot 10^{-4}$	$(0.588 \pm 0.045) \cdot 10^{-3}$	$(0.236 \pm 0.020) \cdot 10^{-3}$
3.75 ± 0.25	$(0.641 \pm 0.079) \cdot 10^{-4}$	$(0.102 \pm 0.009) \cdot 10^{-3}$	$(0.300 \pm 0.022) \cdot 10^{-3}$	—	$(0.915 \pm 0.166) \cdot 10^{-4}$	$(0.309 \pm 0.075) \cdot 10^{-4}$
4.25 ± 0.25	—	$(0.271 \pm 0.042) \cdot 10^{-4}$	$(0.622 \pm 0.097) \cdot 10^{-4}$	—	—	—
4.75 ± 0.25	—	—	—	—	—	—

Table 9: The table of $\pi^{\pm}$, $p, \bar{p}$, $K^{\pm}$ invariant yields at $y = 0$ for Pb+Pb(0-5%) – central – reactions at $\sqrt{s_{NN}} = 17.3\,\mathrm{GeV}$.

p_T [GeV/c]	$\frac{1}{2\pi \cdot p_T} \cdot \frac{\mathrm{d}^2 n}{\mathrm{d}y\,\mathrm{d}p_T}\Big\|_{y=0}$ [1/(GeV/c)^2]					
	π^+	π^-	p	$\bar{p}$	K^+	K^-
0.05 ± 0.05	—	—	—	—	—	—
0.15 ± 0.05	—	—	—	—	—	—
0.25 ± 0.05	—	—	—	—	—	—
0.35 ± 0.05	$(5.920 \pm 0.100) \cdot 10^{+1}$	$(6.863 \pm 0.134) \cdot 10^{+1}$	$(4.926 \pm 0.080) \cdot 10^{+0}$	—	$(1.002 \pm 0.026) \cdot 10^{+1}$	$(7.222 \pm 0.221) \cdot 10^{+0}$
0.45 ± 0.05	$(3.456 \pm 0.074) \cdot 10^{+1}$	$(3.753 \pm 0.088) \cdot 10^{+1}$	$(4.621 \pm 0.078) \cdot 10^{+0}$	$(0.264 \pm 0.007) \cdot 10^{+0}$	$(8.361 \pm 0.246) \cdot 10^{+0}$	$(5.039 \pm 0.146) \cdot 10^{+0}$
0.55 ± 0.05	$(2.027 \pm 0.044) \cdot 10^{+1}$	$(2.022 \pm 0.035) \cdot 10^{+1}$	$(4.157 \pm 0.065) \cdot 10^{+0}$	$(0.250 \pm 0.006) \cdot 10^{+0}$	$(5.766 \pm 0.145) \cdot 10^{+0}$	$(3.210 \pm 0.079) \cdot 10^{+0}$
0.65 ± 0.05	$(1.177 \pm 0.022) \cdot 10^{+1}$	$(1.210 \pm 0.021) \cdot 10^{+1}$	$(3.590 \pm 0.053) \cdot 10^{+0}$	$(0.229 \pm 0.007) \cdot 10^{+0}$	$(4.197 \pm 0.118) \cdot 10^{+0}$	$(2.229 \pm 0.058) \cdot 10^{+0}$
0.75 ± 0.05	$(7.201 \pm 0.119) \cdot 10^{+0}$	$(7.286 \pm 0.113) \cdot 10^{+0}$	$(3.095 \pm 0.047) \cdot 10^{+0}$	$(0.189 \pm 0.006) \cdot 10^{+0}$	$(2.763 \pm 0.063) \cdot 10^{+0}$	$(1.625 \pm 0.042) \cdot 10^{+0}$
0.85 ± 0.05	$(4.417 \pm 0.067) \cdot 10^{+0}$	$(4.512 \pm 0.066) \cdot 10^{+0}$	$(2.526 \pm 0.038) \cdot 10^{+0}$	$(0.154 \pm 0.005) \cdot 10^{+0}$	$(1.948 \pm 0.043) \cdot 10^{+0}$	$(1.079 \pm 0.024) \cdot 10^{+0}$
0.95 ± 0.05	$(2.758 \pm 0.042) \cdot 10^{+0}$	$(2.862 \pm 0.047) \cdot 10^{+0}$	$(1.978 \pm 0.028) \cdot 10^{+0}$	$(0.126 \pm 0.004) \cdot 10^{+0}$	$(1.288 \pm 0.027) \cdot 10^{+0}$	$(0.746 \pm 0.017) \cdot 10^{+0}$
1.05 ± 0.05	$(1.691 \pm 0.023) \cdot 10^{+0}$	$(1.800 \pm 0.030) \cdot 10^{+0}$	$(1.555 \pm 0.022) \cdot 10^{+0}$	$(0.896 \pm 0.029) \cdot 10^{-1}$	$(0.882 \pm 0.018) \cdot 10^{+0}$	$(0.483 \pm 0.010) \cdot 10^{+0}$
1.15 ± 0.05	$(1.104 \pm 0.018) \cdot 10^{+0}$	$(1.137 \pm 0.018) \cdot 10^{+0}$	$(1.173 \pm 0.016) \cdot 10^{+0}$	$(0.709 \pm 0.025) \cdot 10^{-1}$	$(0.631 \pm 0.015) \cdot 10^{+0}$	$(0.329 \pm 0.007) \cdot 10^{+0}$
1.25 ± 0.05	$(0.700 \pm 0.010) \cdot 10^{+0}$	$(0.730 \pm 0.011) \cdot 10^{+0}$	$(0.907 \pm 0.012) \cdot 10^{+0}$	$(0.512 \pm 0.020) \cdot 10^{-1}$	$(0.456 \pm 0.010) \cdot 10^{+0}$	$(0.220 \pm 0.005) \cdot 10^{+0}$
1.35 ± 0.05	$(0.459 \pm 0.008) \cdot 10^{+0}$	$(0.474 \pm 0.007) \cdot 10^{+0}$	$(0.700 \pm 0.012) \cdot 10^{+0}$	$(0.382 \pm 0.017) \cdot 10^{-1}$	$(0.262 \pm 0.006) \cdot 10^{+0}$	$(0.153 \pm 0.004) \cdot 10^{+0}$
1.45 ± 0.05	$(0.295 \pm 0.004) \cdot 10^{+0}$	$(0.302 \pm 0.004) \cdot 10^{+0}$	$(0.507 \pm 0.007) \cdot 10^{+0}$	$(0.304 \pm 0.013) \cdot 10^{-1}$	$(0.197 \pm 0.004) \cdot 10^{+0}$	$(0.101 \pm 0.002) \cdot 10^{+0}$
1.55 ± 0.05	$(0.190 \pm 0.003) \cdot 10^{+0}$	$(0.195 \pm 0.003) \cdot 10^{+0}$	$(0.365 \pm 0.005) \cdot 10^{+0}$	$(0.209 \pm 0.011) \cdot 10^{-1}$	$(0.145 \pm 0.003) \cdot 10^{+0}$	$(0.650 \pm 0.014) \cdot 10^{-1}$
1.65 ± 0.05	$(0.129 \pm 0.002) \cdot 10^{+0}$	$(0.128 \pm 0.002) \cdot 10^{+0}$	$(0.259 \pm 0.004) \cdot 10^{+0}$	$(0.142 \pm 0.009) \cdot 10^{-1}$	$(0.924 \pm 0.022) \cdot 10^{-1}$	$(0.432 \pm 0.009) \cdot 10^{-1}$
1.75 ± 0.05	$(0.850 \pm 0.014) \cdot 10^{-1}$	$(0.843 \pm 0.014) \cdot 10^{-1}$	$(0.191 \pm 0.003) \cdot 10^{+0}$	$(0.114 \pm 0.007) \cdot 10^{-1}$	$(0.656 \pm 0.015) \cdot 10^{-1}$	$(0.307 \pm 0.006) \cdot 10^{-1}$
1.85 ± 0.05	$(0.547 \pm 0.009) \cdot 10^{-1}$	$(0.560 \pm 0.010) \cdot 10^{-1}$	$(0.132 \pm 0.002) \cdot 10^{+0}$	$(0.714 \pm 0.054) \cdot 10^{-2}$	$(0.463 \pm 0.011) \cdot 10^{-1}$	$(0.210 \pm 0.006) \cdot 10^{-1}$
1.95 ± 0.05	$(0.374 \pm 0.007) \cdot 10^{-1}$	$(0.370 \pm 0.006) \cdot 10^{-1}$	$(0.956 \pm 0.015) \cdot 10^{-1}$	$(0.503 \pm 0.026) \cdot 10^{-2}$	$(0.315 \pm 0.008) \cdot 10^{-1}$	$(0.135 \pm 0.004) \cdot 10^{-1}$
2.10 ± 0.10	$(0.207 \pm 0.003) \cdot 10^{-1}$	$(0.208 \pm 0.003) \cdot 10^{-1}$	$(0.571 \pm 0.007) \cdot 10^{-1}$	$(0.250 \pm 0.014) \cdot 10^{-2}$	$(0.195 \pm 0.004) \cdot 10^{-1}$	$(0.787 \pm 0.018) \cdot 10^{-2}$
2.30 ± 0.10	$(0.880 \pm 0.016) \cdot 10^{-2}$	$(0.923 \pm 0.017) \cdot 10^{-2}$	$(0.286 \pm 0.004) \cdot 10^{-1}$	$(0.124 \pm 0.009) \cdot 10^{-2}$	$(0.909 \pm 0.024) \cdot 10^{-2}$	$(0.365 \pm 0.011) \cdot 10^{-2}$
2.50 ± 0.10	$(0.419 \pm 0.010) \cdot 10^{-2}$	$(0.424 \pm 0.010) \cdot 10^{-2}$	$(0.143 \pm 0.002) \cdot 10^{-1}$	$(0.591 \pm 0.054) \cdot 10^{-3}$	$(0.442 \pm 0.015) \cdot 10^{-2}$	$(0.181 \pm 0.007) \cdot 10^{-2}$
2.70 ± 0.10	$(0.191 \pm 0.007) \cdot 10^{-2}$	$(0.189 \pm 0.006) \cdot 10^{-2}$	$(0.697 \pm 0.015) \cdot 10^{-2}$	$(0.179 \pm 0.033) \cdot 10^{-3}$	$(0.222 \pm 0.010) \cdot 10^{-2}$	$(0.770 \pm 0.046) \cdot 10^{-3}$
2.90 ± 0.10	$(0.908 \pm 0.045) \cdot 10^{-3}$	$(0.927 \pm 0.040) \cdot 10^{-3}$	$(0.347 \pm 0.009) \cdot 10^{-2}$	$(0.176 \pm 0.025) \cdot 10^{-3}$	$(0.918 \pm 0.068) \cdot 10^{-3}$	$(0.277 \pm 0.029) \cdot 10^{-3}$
3.25 ± 0.25	$(0.245 \pm 0.014) \cdot 10^{-3}$	$(0.258 \pm 0.013) \cdot 10^{-3}$	$(0.107 \pm 0.003) \cdot 10^{-2}$	$(0.281 \pm 0.080) \cdot 10^{-4}$	$(0.307 \pm 0.022) \cdot 10^{-3}$	$(0.840 \pm 0.100) \cdot 10^{-4}$
3.75 ± 0.25	$(0.404 \pm 0.049) \cdot 10^{-4}$	$(0.419 \pm 0.046) \cdot 10^{-4}$	$(0.197 \pm 0.011) \cdot 10^{-3}$	—	$(0.359 \pm 0.080) \cdot 10^{-4}$	$(0.134 \pm 0.038) \cdot 10^{-4}$
4.25 ± 0.25	—	—	$(0.280 \pm 0.044) \cdot 10^{-4}$	—	—	—
4.75 ± 0.25	—	—	—	—	—	—

Table 10: The table of $\pi^{\pm}$, $p, \bar{p}$, $K^{\pm}$ invariant yields at $y = 0$ for Pb+Pb(12.5-23.5%) – mid-central – reactions at $\sqrt{s_{_{NN}}} = 17.3\,\mathrm{GeV}$.

p_T [GeV/c]	$\frac{1}{2\pi \cdot p_T} \cdot \frac{\mathrm{d}^2 n}{\mathrm{d}y\,\mathrm{d}p_T}\Big\|_{y=0}$ [1/(GeV/c)^2]					
	π^+	π^-	p	$\bar{p}$	K^+	K^-
0.05 ± 0.05	—	—	—	—	—	—
0.15 ± 0.05	—	—	—	—	—	—
0.25 ± 0.05	—	—	—	—	—	—
0.35 ± 0.05	$(1.683 \pm 0.020) \cdot 10^{+1}$	$(1.730 \pm 0.019) \cdot 10^{+1}$	$(1.690 \pm 0.033) \cdot 10^{+0}$	—	$(2.781 \pm 0.074) \cdot 10^{+0}$	$(1.829 \pm 0.046) \cdot 10^{+0}$
0.45 ± 0.05	$(9.267 \pm 0.129) \cdot 10^{+0}$	$(9.483 \pm 0.104) \cdot 10^{+0}$	$(1.416 \pm 0.026) \cdot 10^{+0}$	$(0.123 \pm 0.009) \cdot 10^{+0}$	$(1.948 \pm 0.047) \cdot 10^{+0}$	$(1.326 \pm 0.036) \cdot 10^{+0}$
0.55 ± 0.05	$(5.246 \pm 0.069) \cdot 10^{+0}$	$(5.406 \pm 0.071) \cdot 10^{+0}$	$(1.276 \pm 0.021) \cdot 10^{+0}$	$(0.110 \pm 0.007) \cdot 10^{+0}$	$(1.417 \pm 0.037) \cdot 10^{+0}$	$(0.877 \pm 0.023) \cdot 10^{+0}$
0.65 ± 0.05	$(3.106 \pm 0.041) \cdot 10^{+0}$	$(3.258 \pm 0.048) \cdot 10^{+0}$	$(1.040 \pm 0.016) \cdot 10^{+0}$	$(0.100 \pm 0.005) \cdot 10^{+0}$	$(0.983 \pm 0.028) \cdot 10^{+0}$	$(0.566 \pm 0.017) \cdot 10^{+0}$
0.75 ± 0.05	$(1.864 \pm 0.025) \cdot 10^{+0}$	$(1.948 \pm 0.028) \cdot 10^{+0}$	$(0.841 \pm 0.014) \cdot 10^{+0}$	$(0.740 \pm 0.040) \cdot 10^{-1}$	$(0.665 \pm 0.018) \cdot 10^{+0}$	$(0.391 \pm 0.011) \cdot 10^{+0}$
0.85 ± 0.05	$(1.160 \pm 0.018) \cdot 10^{+0}$	$(1.192 \pm 0.018) \cdot 10^{+0}$	$(0.637 \pm 0.010) \cdot 10^{+0}$	$(0.603 \pm 0.036) \cdot 10^{-1}$	$(0.430 \pm 0.011) \cdot 10^{+0}$	$(0.267 \pm 0.008) \cdot 10^{+0}$
0.95 ± 0.05	$(0.697 \pm 0.010) \cdot 10^{+0}$	$(0.721 \pm 0.011) \cdot 10^{+0}$	$(0.492 \pm 0.009) \cdot 10^{+0}$	$(0.465 \pm 0.028) \cdot 10^{-1}$	$(0.311 \pm 0.009) \cdot 10^{+0}$	$(0.174 \pm 0.006) \cdot 10^{+0}$
1.05 ± 0.05	$(0.426 \pm 0.008) \cdot 10^{+0}$	$(0.456 \pm 0.008) \cdot 10^{+0}$	$(0.376 \pm 0.007) \cdot 10^{+0}$	$(0.336 \pm 0.023) \cdot 10^{-1}$	$(0.202 \pm 0.007) \cdot 10^{+0}$	$(0.116 \pm 0.004) \cdot 10^{+0}$
1.15 ± 0.05	$(0.270 \pm 0.005) \cdot 10^{+0}$	$(0.284 \pm 0.005) \cdot 10^{+0}$	$(0.286 \pm 0.005) \cdot 10^{+0}$	$(0.242 \pm 0.018) \cdot 10^{-1}$	$(0.134 \pm 0.005) \cdot 10^{+0}$	$(0.717 \pm 0.026) \cdot 10^{-1}$
1.25 ± 0.05	$(0.171 \pm 0.003) \cdot 10^{+0}$	$(0.185 \pm 0.004) \cdot 10^{+0}$	$(0.207 \pm 0.004) \cdot 10^{+0}$	$(0.171 \pm 0.017) \cdot 10^{-1}$	$(0.915 \pm 0.037) \cdot 10^{-1}$	$(0.493 \pm 0.021) \cdot 10^{-1}$
1.35 ± 0.05	$(0.111 \pm 0.003) \cdot 10^{+0}$	$(0.117 \pm 0.003) \cdot 10^{+0}$	$(0.151 \pm 0.004) \cdot 10^{+0}$	$(0.139 \pm 0.015) \cdot 10^{-1}$	$(0.602 \pm 0.030) \cdot 10^{-1}$	$(0.330 \pm 0.016) \cdot 10^{-1}$
1.45 ± 0.05	$(0.722 \pm 0.018) \cdot 10^{-1}$	$(0.738 \pm 0.019) \cdot 10^{-1}$	$(0.111 \pm 0.003) \cdot 10^{+0}$	$(0.933 \pm 0.106) \cdot 10^{-2}$	$(0.406 \pm 0.025) \cdot 10^{-1}$	$(0.198 \pm 0.011) \cdot 10^{-1}$
1.55 ± 0.05	$(0.452 \pm 0.013) \cdot 10^{-1}$	$(0.513 \pm 0.014) \cdot 10^{-1}$	$(0.769 \pm 0.027) \cdot 10^{-1}$	$(0.577 \pm 0.079) \cdot 10^{-2}$	$(0.291 \pm 0.021) \cdot 10^{-1}$	$(0.131 \pm 0.008) \cdot 10^{-1}$
1.65 ± 0.05	$(0.301 \pm 0.011) \cdot 10^{-1}$	$(0.323 \pm 0.011) \cdot 10^{-1}$	$(0.550 \pm 0.018) \cdot 10^{-1}$	$(0.385 \pm 0.087) \cdot 10^{-2}$	$(0.192 \pm 0.018) \cdot 10^{-1}$	$(0.964 \pm 0.067) \cdot 10^{-2}$
1.75 ± 0.05	$(0.201 \pm 0.008) \cdot 10^{-1}$	$(0.199 \pm 0.008) \cdot 10^{-1}$	$(0.390 \pm 0.015) \cdot 10^{-1}$	$(0.344 \pm 0.062) \cdot 10^{-2}$	$(0.153 \pm 0.015) \cdot 10^{-1}$	$(0.523 \pm 0.047) \cdot 10^{-2}$
1.85 ± 0.05	$(0.125 \pm 0.006) \cdot 10^{-1}$	$(0.131 \pm 0.006) \cdot 10^{-1}$	$(0.267 \pm 0.013) \cdot 10^{-1}$	$(0.139 \pm 0.033) \cdot 10^{-2}$	$(0.945 \pm 0.128) \cdot 10^{-2}$	$(0.388 \pm 0.038) \cdot 10^{-2}$
1.95 ± 0.05	$(0.857 \pm 0.047) \cdot 10^{-2}$	$(0.888 \pm 0.047) \cdot 10^{-2}$	$(0.186 \pm 0.009) \cdot 10^{-1}$	$(0.114 \pm 0.031) \cdot 10^{-2}$	$(0.753 \pm 0.144) \cdot 10^{-2}$	$(0.301 \pm 0.032) \cdot 10^{-2}$
2.10 ± 0.10	$(0.445 \pm 0.025) \cdot 10^{-2}$	$(0.463 \pm 0.025) \cdot 10^{-2}$	$(0.111 \pm 0.005) \cdot 10^{-1}$	$(0.772 \pm 0.194) \cdot 10^{-3}$	$(0.324 \pm 0.032) \cdot 10^{-2}$	$(0.160 \pm 0.017) \cdot 10^{-2}$
2.30 ± 0.10	$(0.210 \pm 0.017) \cdot 10^{-2}$	$(0.235 \pm 0.017) \cdot 10^{-2}$	$(0.552 \pm 0.030) \cdot 10^{-2}$	$(0.577 \pm 0.100) \cdot 10^{-3}$	$(0.142 \pm 0.023) \cdot 10^{-2}$	$(0.620 \pm 0.107) \cdot 10^{-3}$
2.50 ± 0.10	$(0.809 \pm 0.116) \cdot 10^{-3}$	$(0.837 \pm 0.100) \cdot 10^{-3}$	$(0.281 \pm 0.032) \cdot 10^{-2}$	—	$(0.751 \pm 0.153) \cdot 10^{-3}$	$(0.362 \pm 0.075) \cdot 10^{-3}$
2.70 ± 0.10	$(0.349 \pm 0.077) \cdot 10^{-3}$	$(0.411 \pm 0.068) \cdot 10^{-3}$	$(0.134 \pm 0.020) \cdot 10^{-2}$	—	—	—
2.90 ± 0.10	—	—	$(0.503 \pm 0.084) \cdot 10^{-3}$	—	—	—
3.25 ± 0.25	—	—	$(0.230 \pm 0.028) \cdot 10^{-3}$	—	—	—
3.75 ± 0.25	—	—	—	—	—	—
4.25 ± 0.25	—	—	—	—	—	—
4.75 ± 0.25	—	—	—	—	—	—

Table 11: The table of $\pi^{\pm}$, $p, \bar{p}$, $K^{\pm}$ invariant yields at $y = 0$ for Pb+Pb(33.5-80%) – peripheral – reactions at $\sqrt{s_{NN}} = 17.3\,\mathrm{GeV}$.

p_T [GeV/c]	$\frac{1}{2\pi \cdot p_T} \cdot \frac{\mathrm{d}^2 n}{\mathrm{d}y\,\mathrm{d}p_T}\Big\|_{y=0}$ [1/(GeV/c)^2]					
	π^+	π^-	p	$\bar{p}$	K^+	K^-
0.05 ± 0.05	—	—	—	—	—	—
0.15 ± 0.05	—	—	—	—	—	—
0.25 ± 0.05	—	—	—	—	—	—
0.35 ± 0.05	$(1.479 \pm 0.022) \cdot 10^{+0}$	$(1.425 \pm 0.020) \cdot 10^{+0}$	$(0.161 \pm 0.002) \cdot 10^{+0}$	—	$(0.170 \pm 0.005) \cdot 10^{+0}$	$(0.108 \pm 0.003) \cdot 10^{+0}$
0.45 ± 0.05	$(0.793 \pm 0.013) \cdot 10^{+0}$	$(0.755 \pm 0.011) \cdot 10^{+0}$	$(0.126 \pm 0.002) \cdot 10^{+0}$	$(0.200 \pm 0.008) \cdot 10^{-1}$	$(0.115 \pm 0.003) \cdot 10^{+0}$	$(0.828 \pm 0.028) \cdot 10^{-1}$
0.55 ± 0.05	$(0.448 \pm 0.007) \cdot 10^{+0}$	$(0.447 \pm 0.007) \cdot 10^{+0}$	$(0.913 \pm 0.013) \cdot 10^{-1}$	$(0.160 \pm 0.006) \cdot 10^{-1}$	$(0.762 \pm 0.025) \cdot 10^{-1}$	$(0.491 \pm 0.016) \cdot 10^{-1}$
0.65 ± 0.05	$(0.249 \pm 0.004) \cdot 10^{+0}$	$(0.258 \pm 0.005) \cdot 10^{+0}$	$(0.660 \pm 0.010) \cdot 10^{-1}$	$(0.114 \pm 0.005) \cdot 10^{-1}$	$(0.570 \pm 0.020) \cdot 10^{-1}$	$(0.326 \pm 0.012) \cdot 10^{-1}$
0.75 ± 0.05	$(0.144 \pm 0.002) \cdot 10^{+0}$	$(0.147 \pm 0.003) \cdot 10^{+0}$	$(0.509 \pm 0.008) \cdot 10^{-1}$	$(0.816 \pm 0.039) \cdot 10^{-2}$	$(0.348 \pm 0.012) \cdot 10^{-1}$	$(0.219 \pm 0.008) \cdot 10^{-1}$
0.85 ± 0.05	$(0.873 \pm 0.017) \cdot 10^{-1}$	$(0.874 \pm 0.017) \cdot 10^{-1}$	$(0.359 \pm 0.006) \cdot 10^{-1}$	$(0.623 \pm 0.032) \cdot 10^{-2}$	$(0.234 \pm 0.008) \cdot 10^{-1}$	$(0.129 \pm 0.005) \cdot 10^{-1}$
0.95 ± 0.05	$(0.503 \pm 0.010) \cdot 10^{-1}$	$(0.512 \pm 0.010) \cdot 10^{-1}$	$(0.249 \pm 0.005) \cdot 10^{-1}$	$(0.368 \pm 0.022) \cdot 10^{-2}$	$(0.163 \pm 0.007) \cdot 10^{-1}$	$(0.888 \pm 0.039) \cdot 10^{-2}$
1.05 ± 0.05	$(0.339 \pm 0.007) \cdot 10^{-1}$	$(0.337 \pm 0.007) \cdot 10^{-1}$	$(0.177 \pm 0.004) \cdot 10^{-1}$	$(0.237 \pm 0.017) \cdot 10^{-2}$	$(0.111 \pm 0.005) \cdot 10^{-1}$	$(0.584 \pm 0.031) \cdot 10^{-2}$
1.15 ± 0.05	$(0.202 \pm 0.005) \cdot 10^{-1}$	$(0.204 \pm 0.005) \cdot 10^{-1}$	$(0.123 \pm 0.003) \cdot 10^{-1}$	$(0.169 \pm 0.014) \cdot 10^{-2}$	$(0.682 \pm 0.035) \cdot 10^{-2}$	$(0.385 \pm 0.022) \cdot 10^{-2}$
1.25 ± 0.05	$(0.132 \pm 0.003) \cdot 10^{-1}$	$(0.131 \pm 0.004) \cdot 10^{-1}$	$(0.850 \pm 0.024) \cdot 10^{-2}$	$(0.960 \pm 0.097) \cdot 10^{-3}$	$(0.451 \pm 0.024) \cdot 10^{-2}$	$(0.254 \pm 0.016) \cdot 10^{-2}$
1.35 ± 0.05	$(0.818 \pm 0.026) \cdot 10^{-2}$	$(0.808 \pm 0.024) \cdot 10^{-2}$	$(0.596 \pm 0.022) \cdot 10^{-2}$	$(0.608 \pm 0.075) \cdot 10^{-3}$	$(0.309 \pm 0.021) \cdot 10^{-2}$	$(0.155 \pm 0.012) \cdot 10^{-2}$
1.45 ± 0.05	$(0.514 \pm 0.018) \cdot 10^{-2}$	$(0.533 \pm 0.017) \cdot 10^{-2}$	$(0.394 \pm 0.014) \cdot 10^{-2}$	$(0.348 \pm 0.052) \cdot 10^{-3}$	$(0.200 \pm 0.013) \cdot 10^{-2}$	$(0.120 \pm 0.009) \cdot 10^{-2}$
1.55 ± 0.05	$(0.337 \pm 0.013) \cdot 10^{-2}$	$(0.351 \pm 0.014) \cdot 10^{-2}$	$(0.262 \pm 0.011) \cdot 10^{-2}$	$(0.210 \pm 0.038) \cdot 10^{-3}$	$(0.144 \pm 0.011) \cdot 10^{-2}$	$(0.683 \pm 0.067) \cdot 10^{-3}$
1.65 ± 0.05	$(0.213 \pm 0.010) \cdot 10^{-2}$	$(0.217 \pm 0.010) \cdot 10^{-2}$	$(0.179 \pm 0.009) \cdot 10^{-2}$	$(0.147 \pm 0.032) \cdot 10^{-3}$	$(0.891 \pm 0.082) \cdot 10^{-3}$	$(0.402 \pm 0.050) \cdot 10^{-3}$
1.75 ± 0.05	$(0.137 \pm 0.008) \cdot 10^{-2}$	$(0.139 \pm 0.007) \cdot 10^{-2}$	$(0.131 \pm 0.007) \cdot 10^{-2}$	—	$(0.644 \pm 0.067) \cdot 10^{-3}$	$(0.335 \pm 0.041) \cdot 10^{-3}$
1.85 ± 0.05	$(0.107 \pm 0.006) \cdot 10^{-2}$	$(0.932 \pm 0.057) \cdot 10^{-3}$	$(0.865 \pm 0.057) \cdot 10^{-3}$	—	$(0.559 \pm 0.057) \cdot 10^{-3}$	$(0.149 \pm 0.026) \cdot 10^{-3}$
1.95 ± 0.05	$(0.634 \pm 0.047) \cdot 10^{-3}$	$(0.555 \pm 0.043) \cdot 10^{-3}$	$(0.608 \pm 0.046) \cdot 10^{-3}$	—	$(0.275 \pm 0.042) \cdot 10^{-3}$	$(0.109 \pm 0.024) \cdot 10^{-3}$
2.10 ± 0.10	$(0.352 \pm 0.026) \cdot 10^{-3}$	$(0.336 \pm 0.025) \cdot 10^{-3}$	$(0.322 \pm 0.027) \cdot 10^{-3}$	—	$(0.154 \pm 0.024) \cdot 10^{-3}$	$(0.567 \pm 0.130) \cdot 10^{-4}$
2.30 ± 0.10	$(0.155 \pm 0.016) \cdot 10^{-3}$	$(0.136 \pm 0.015) \cdot 10^{-3}$	$(0.160 \pm 0.018) \cdot 10^{-3}$	—	$(0.649 \pm 0.153) \cdot 10^{-4}$	—
2.50 ± 0.10	$(0.549 \pm 0.093) \cdot 10^{-4}$	$(0.646 \pm 0.101) \cdot 10^{-4}$	$(0.722 \pm 0.114) \cdot 10^{-4}$	—	$(0.649 \pm 0.120) \cdot 10^{-4}$	—
2.70 ± 0.10	—	—	$(0.341 \pm 0.077) \cdot 10^{-4}$	—	—	—
2.90 ± 0.10	—	—	—	—	—	—
3.25 ± 0.25	—	—	—	—	—	—
3.75 ± 0.25	—	—	—	—	—	—
4.25 ± 0.25	—	—	—	—	—	—
4.75 ± 0.25	—	—	—	—	—	—

Table 12: The table of $\pi^{\pm}$, $p, \bar{p}$, $K^{\pm}$ invariant yields at $y = 0$ for p+Pb reactions at $\sqrt{s_{NN}} = 17.3\,\mathrm{GeV}$. (Full dataset with varied centrality trigger setting, as discussed in Section 3.2.2.)

p_T [GeV/c]	$\frac{1}{2\pi \cdot p_T} \cdot \frac{\mathrm{d}^2 n}{\mathrm{d}y\,\mathrm{d}p_T}\Big\|_{y=0}$ [1/(GeV/c)^2]					
	π^+	π^-	p	$\bar{p}$	K^+	K^-
0.05 ± 0.05	—	—	—	—	—	—
0.15 ± 0.05	—	—	—	—	—	—
0.25 ± 0.05	—	—	—	—	—	—
0.35 ± 0.05	$(0.579 \pm 0.009) \cdot 10^{+0}$	$(0.521 \pm 0.007) \cdot 10^{+0}$	$(0.487 \pm 0.008) \cdot 10^{-1}$	—	$(0.516 \pm 0.018) \cdot 10^{-1}$	$(0.323 \pm 0.010) \cdot 10^{-1}$
0.45 ± 0.05	$(0.314 \pm 0.005) \cdot 10^{+0}$	$(0.271 \pm 0.004) \cdot 10^{+0}$	$(0.382 \pm 0.006) \cdot 10^{-1}$	$(0.995 \pm 0.027) \cdot 10^{-2}$	$(0.338 \pm 0.011) \cdot 10^{-1}$	$(0.235 \pm 0.007) \cdot 10^{-1}$
0.55 ± 0.05	$(0.171 \pm 0.003) \cdot 10^{+0}$	$(0.152 \pm 0.002) \cdot 10^{+0}$	$(0.289 \pm 0.004) \cdot 10^{-1}$	$(0.637 \pm 0.019) \cdot 10^{-2}$	$(0.220 \pm 0.007) \cdot 10^{-1}$	$(0.152 \pm 0.005) \cdot 10^{-1}$
0.65 ± 0.05	$(0.951 \pm 0.015) \cdot 10^{-1}$	$(0.840 \pm 0.015) \cdot 10^{-1}$	$(0.193 \pm 0.003) \cdot 10^{-1}$	$(0.424 \pm 0.014) \cdot 10^{-2}$	$(0.148 \pm 0.005) \cdot 10^{-1}$	$(0.944 \pm 0.034) \cdot 10^{-2}$
0.75 ± 0.05	$(0.521 \pm 0.009) \cdot 10^{-1}$	$(0.467 \pm 0.008) \cdot 10^{-1}$	$(0.142 \pm 0.003) \cdot 10^{-1}$	$(0.275 \pm 0.011) \cdot 10^{-2}$	$(0.966 \pm 0.034) \cdot 10^{-2}$	$(0.604 \pm 0.023) \cdot 10^{-2}$
0.85 ± 0.05	$(0.304 \pm 0.006) \cdot 10^{-1}$	$(0.261 \pm 0.005) \cdot 10^{-1}$	$(0.962 \pm 0.019) \cdot 10^{-2}$	$(0.187 \pm 0.008) \cdot 10^{-2}$	$(0.596 \pm 0.022) \cdot 10^{-2}$	$(0.337 \pm 0.014) \cdot 10^{-2}$
0.95 ± 0.05	$(0.171 \pm 0.003) \cdot 10^{-1}$	$(0.144 \pm 0.003) \cdot 10^{-1}$	$(0.636 \pm 0.015) \cdot 10^{-2}$	$(0.948 \pm 0.060) \cdot 10^{-3}$	$(0.401 \pm 0.017) \cdot 10^{-2}$	$(0.217 \pm 0.010) \cdot 10^{-2}$
1.05 ± 0.05	$(0.987 \pm 0.022) \cdot 10^{-2}$	$(0.864 \pm 0.020) \cdot 10^{-2}$	$(0.400 \pm 0.011) \cdot 10^{-2}$	$(0.637 \pm 0.043) \cdot 10^{-3}$	$(0.242 \pm 0.012) \cdot 10^{-2}$	$(0.121 \pm 0.007) \cdot 10^{-2}$
1.15 ± 0.05	$(0.565 \pm 0.013) \cdot 10^{-2}$	$(0.506 \pm 0.012) \cdot 10^{-2}$	$(0.261 \pm 0.008) \cdot 10^{-2}$	$(0.404 \pm 0.032) \cdot 10^{-3}$	$(0.148 \pm 0.008) \cdot 10^{-2}$	$(0.777 \pm 0.048) \cdot 10^{-3}$
1.25 ± 0.05	$(0.320 \pm 0.008) \cdot 10^{-2}$	$(0.299 \pm 0.009) \cdot 10^{-2}$	$(0.175 \pm 0.006) \cdot 10^{-2}$	$(0.228 \pm 0.023) \cdot 10^{-3}$	$(0.900 \pm 0.057) \cdot 10^{-3}$	$(0.444 \pm 0.034) \cdot 10^{-3}$
1.35 ± 0.05	$(0.204 \pm 0.007) \cdot 10^{-2}$	$(0.159 \pm 0.006) \cdot 10^{-2}$	$(0.111 \pm 0.005) \cdot 10^{-2}$	$(0.133 \pm 0.021) \cdot 10^{-3}$	$(0.574 \pm 0.040) \cdot 10^{-3}$	$(0.268 \pm 0.027) \cdot 10^{-3}$
1.45 ± 0.05	$(0.123 \pm 0.005) \cdot 10^{-2}$	$(0.108 \pm 0.004) \cdot 10^{-2}$	$(0.761 \pm 0.039) \cdot 10^{-3}$	$(0.689 \pm 0.113) \cdot 10^{-4}$	$(0.417 \pm 0.035) \cdot 10^{-3}$	$(0.212 \pm 0.020) \cdot 10^{-3}$
1.55 ± 0.05	$(0.780 \pm 0.034) \cdot 10^{-3}$	$(0.586 \pm 0.029) \cdot 10^{-3}$	$(0.432 \pm 0.026) \cdot 10^{-3}$	$(0.490 \pm 0.087) \cdot 10^{-4}$	$(0.220 \pm 0.022) \cdot 10^{-3}$	$(0.963 \pm 0.128) \cdot 10^{-4}$
1.65 ± 0.05	$(0.471 \pm 0.026) \cdot 10^{-3}$	$(0.386 \pm 0.023) \cdot 10^{-3}$	$(0.259 \pm 0.021) \cdot 10^{-3}$	—	$(0.164 \pm 0.018) \cdot 10^{-3}$	$(0.811 \pm 0.117) \cdot 10^{-4}$
1.75 ± 0.05	$(0.283 \pm 0.019) \cdot 10^{-3}$	$(0.251 \pm 0.017) \cdot 10^{-3}$	$(0.174 \pm 0.015) \cdot 10^{-3}$	—	$(0.104 \pm 0.014) \cdot 10^{-3}$	$(0.405 \pm 0.080) \cdot 10^{-4}$
1.85 ± 0.05	$(0.174 \pm 0.013) \cdot 10^{-3}$	$(0.137 \pm 0.012) \cdot 10^{-3}$	$(0.110 \pm 0.011) \cdot 10^{-3}$	—	$(0.627 \pm 0.099) \cdot 10^{-4}$	$(0.307 \pm 0.059) \cdot 10^{-4}$
1.95 ± 0.05	$(0.878 \pm 0.091) \cdot 10^{-4}$	$(0.763 \pm 0.084) \cdot 10^{-4}$	$(0.734 \pm 0.096) \cdot 10^{-4}$	—	$(0.443 \pm 0.089) \cdot 10^{-4}$	—
2.10 ± 0.10	$(0.635 \pm 0.058) \cdot 10^{-4}$	$(0.373 \pm 0.044) \cdot 10^{-4}$	$(0.353 \pm 0.049) \cdot 10^{-4}$	—	$(0.243 \pm 0.045) \cdot 10^{-4}$	—
2.30 ± 0.10	$(0.167 \pm 0.028) \cdot 10^{-4}$	$(0.157 \pm 0.027) \cdot 10^{-4}$	—	—	—	—
2.50 ± 0.10	$(0.134 \pm 0.025) \cdot 10^{-4}$	—	—	—	—	—
2.70 ± 0.10	—	—	—	—	—	—
2.90 ± 0.10	—	—	—	—	—	—
3.25 ± 0.25	—	—	—	—	—	—
3.75 ± 0.25	—	—	—	—	—	—
4.25 ± 0.25	—	—	—	—	—	—
4.75 ± 0.25	—	—	—	—	—	—

Table 13: The table of $\pi^{\pm}$, $p, \bar{p}$, $K^{\pm}$ invariant yields at $y = 0$ for p+p reactions at $\sqrt{s_{NN}} = 17.3\,\mathrm{GeV}$.

D Glossary of Notations and Terms

$:=$ — Defining equality. E.g.: $x := y$ means that the quantity x is defined to be the expression y.

$=$ — Claiming equality. E.g.: $x = y$ means that the quantity x is equal to the expression y.

$\mapsto$ — Mapping. E.g.: $x \mapsto f(x)$ is a description of a function f.

χ_A — Characteristic function of a set A.

acceptance — The inverse image of the sensitive detector volume in the momentum space, by the equation of motion of produced particles.

bias — Distortions of measured quantities, introduced either by the measurement apparatus, or by the analysis procedures.

BNL — Brookhaven National Laboratory (a particle physics laboratory in the USA).

BRAHMS — An experiment at RHIC, mainly for measurement of forward production.

centrality — The fraction of total inelastic cross-section. This measures how head-on is a collision.

CERN — The largest European particle physics laboratory.

DAQ — Data acquisition system.

empty-target — Runs in fixed-target experiments, when the target is removed. Used for background determination.

inclusive — Particle spectra is called inclusive if the detection of a given particle type is required, but the other outcomes are considered as indifferent.

main-vertex — The reconstructed collision point.

minimum-bias — Dataset recorded with the least possible bias.

multiplicity — The number of produced particles.

NA49 — An experiment at the CERN SPS (North Area 49).

PHENIX — An experiment at RHIC.

PHOBOS — An experiment at RHIC.

points — An NA49 term for detected particle trajectory hits in the detector.

potpoints — An NA49 term for such particle hit points, which should be present if the given track corresponds to a real particle.

RHIC — A high energy particle accelerator at BNL.

right-side tracks — Such tracks in a fixed-target experiment, which do not cross the plane, defined by the beamline and the magnetic field direction.

run — A series of subsequent events, taken at a time. Events are usually recorded in runs.

SPS — An accelerator at CERN (Super Proton Synchrotron).

STAR — An experiment at RHIC.

VENUS — A high energy particle production model, which is widely used for Glauber calculations.

wrong-side tracks — Such tracks in a fixed-target experiment, which do cross the plane, defined by the beamline and the magnetic field direction.

List of Figures

1 The phase diagram of the QCD from lattice calculations (figure from [36]). 10

2 Spectator matter in nucleus-nucleus (left), and proton-nucleus (right) collisions. . . 12

3 Top panel: qualitative overview of Landau and Bjørken picture of particle production in nucleus-nucleus collisions. Bottom left panel: a compilation on the variation of the rapidity distribution of π^- particles in nucleus-nucleus collisions, with increasing collision energy per colliding nucleon pair (data from NA49 and BRAHMS, [26]). Bottom right panel: a compilation on the variation of the rapidity distribution of net-baryons in nucleus-nucleus collisions, with increasing collision energy per colliding nucleon pair (figure from [31]). 13

4 The central nucleon-nucleon and minimum-bias deuteron-nucleon nuclear modification factors (with binary collision scaling assumption), measured by the PHENIX experiment at $\sqrt{s_{NN}} = 200\,\mathrm{GeV}$ (figure from [3]). 16

5 The away-side jet suppression in central nucleus-nucleus collisions, measured by PHENIX at $\sqrt{s_{NN}} = 200\,\mathrm{GeV}$ (figure from [1]). 17

6 The architecture of the experiment CERN-NA49 (different beam definitions and target arrangements are also shown). 24

7 The schematic of the S3 Gas-Čerenkov interaction trigger for Pb beams. 27

8 The schematic of the VCAL, used for centrality determination in nucleus-nucleus collisions. 28

9 The schematic of the CD, used for centrality determination in proton-nucleus collisions. (Copper absorber foil between the target and the proportional tubes is not shown.) 29

10 The principle of TPC operation. The lines indicate the direction of the electric field, which is followed by the drifting electrons. 31

11 The schematic of the setup of the VTPCs. Note the N_2 gas envelope around the chamber. 33

12 Distribution of main-vertex longitudinal position in low multiplicity Pb+Pb events. 39

13 Correlation of VCAL energy and total multiplicity. 40

14 Time-dependence calibration of VCAL energy scale. 42

15 Time-dependence correction parameters of VCAL energy scale. 43

16 Subtraction of non-target contamination from the VCAL energy spectrum. 44

17 Measurement of trigger probability. 45

18 Measurement of VENUS total cross section. 49

19 Cross calibration of empiric and VENUS VCAL energy scale. 50

20 Centrality selection by VCAL energy together with the mean values of collision parameters. *: These values are semi-empiric averages, calculated on the full minimum-bias dataset. 50

21 Distribution of main-vertex longitudinal position in p+Pb events. 51

22 Distribution of main-vertex longitudinal position in p+p events. 52

23 Distribution of the CD response for p+Pb minimum-bias events. 53

24 Transverse momentum distribution – all tracks. 57

25 Point/potpoint distribution of $p_T \geq 2\,\mathrm{GeV/c}$ tracks. 57

26 B_x distribution of $p_T \geq 2\,\mathrm{GeV/c}$ tracks. 58

27 B_y distribution of $p_T \geq 2\,\mathrm{GeV/c}$ tracks. 58

28 Fraction of bad tracks (scaled boxes) as a function of momentum – no previous track selection. (Box size range: $0 \leq$fraction≤ 1.) 60

29 Fraction of bad tracks (scaled boxes), as a function of momentum – discontinuous tracks rejected. (Box size range: $0 \leq$fraction≤ 1.) Dotted line: momentum space cut. 62

30 ϕ distribution in the $2.6\,\mathrm{GeV/c} \leq p_T < 2.7\,\mathrm{GeV/c}$ slice – discontinuous tracks rejected. Dotted line: momentum space cut. (The avoiding of efficiency holes.) . . . 63

31 p_T distributions in $0 \leq y_{\pi^\pm} < 0.1$ slice, with different $|\phi|$ cuts – discontinuous tracks rejected. 65

32 Point/potpoint distributions in $0 \leq y_{\pi^\pm} < 0.1$ slice for $p_T \geq 2\,\mathrm{GeV/c}$, with different $|\phi|$ cuts – discontinuous tracks rejected. 65

33 Point/potpoint and fit impact parameter coordinate distributions in slice $0 \leq y_{\pi^\pm} < 0.1$ and domain $2\,\mathrm{GeV/c} \leq p_T < 5\,\mathrm{GeV/c}$ and $|\phi| \leq 10°$. Two quality cuts are compared: tracks without selection and the rejection of discontinuous tracks. . . . 66

34 The correlation of the momentum and the specific energy loss for different particle types, together with the most probable energy loss values. 69

35 Example plot for the $\left(\frac{1}{\sqrt{N}}, \ln\frac{p}{\mathrm{GeV/c}}\right)$ distribution. 72

36 Demonstration of the particle identification fits, $\pi^\pm$ mass hypothesis. 74

37 The systematic errors caused by the residual non-target contamination and the lost events on the track count level, in Pb+Pb$(33.5-80\%)$, with $\pi^\pm$ mass hypothesis. . 76

38 The systematic errors caused by the residual non-target contamination and the lost events on the track count level, in p+Pb (left) and p+p (right), with $\pi^{\pm}$ mass hypothesis. 77

39 Quality of the matching of the Monte Carlo tracks to the reconstructed tracks in Pb+Pb$(0-5\%)$, $\pi^{\pm}$ mass hypothesis. 79

40 Momentum reconstruction quality in Pb+Pb$(0-5\%)$, $\pi^{\pm}$ mass hypothesis. 80

41 Fraction of fake tracks in Pb+Pb (VENUS-4.12), $\pi^{\pm}$ mass hypothesis. 81

42 Feed-down contributions to the $\pi^{\pm}$ and $p, \bar{p}$ channels. ($K^{\pm}$ are omitted, as they have do not have significant feed-down contributions.) 84

43 Tracking inefficiency for $\pi^{\pm}$, $p, \bar{p}$ and $K^{\pm}$. (For $\pi^{\pm}$ and $K^{\pm}$ decay loss correction is also included.) 85

44 The acceptance correction curve for symmetric reactions, with $\pi^{\pm}$ mass hypothesis. 88

45 The fully corrected invariant yields at $y = 0$ of $\pi^{\pm}$, $p, \bar{p}$, $K^{\pm}$ particles in $\sqrt{s_{NN}} =$ 17.3 GeV Pb+Pb, p+Pb and p+p reactions. 91

46 Anti-particle/particle ratios at $y = 0$ in $\sqrt{s_{NN}} = 17.3\,\mathrm{GeV}$ Pb+Pb, p+Pb and p+p reactions. Similar data for $\sqrt{s_{NN}} = 200\,\mathrm{GeV}$ Au+Au, d+Au and p+p reactions are also shown. BW: blast-wave parameterization. pQCD: perturbative QCD calculation. 94

47 K^+/π^+, K^-/π^-, and $\frac{2(K^+-K^-)}{\pi^++\pi^-}$ ratios at $y = 0$ in $\sqrt{s_{NN}} = 17.3\,\mathrm{GeV}$ Pb+Pb, p+Pb and p+p reactions. Similar data for $\sqrt{s_{NN}} = 200\,\mathrm{GeV}$ reactions are also shown. BW: blast-wave parametrization. pQCD: perturbative QCD calculation. 98

48 Ratio of K^+/π^+ and K^-/π^- ratios at $\sqrt{s_{NN}} = 200\,\mathrm{GeV}$ and $\sqrt{s_{NN}} = 17.3\,\mathrm{GeV}$ collision energy. 99

49 Proton/pion ratios at $y = 0$ in $\sqrt{s_{NN}} = 17.3\,\mathrm{GeV}$ Pb+Pb, p+Pb and p+p reactions. Similar data for $\sqrt{s_{NN}} = 200\,\mathrm{GeV}$ reactions are also shown. BW: blast-wave parametrization. pQCD: perturbative QCD calculation. 101

50 Ratio of proton/pion, anti-proton/pion and net-proton/pion ratios at $\sqrt{s_{NN}} = 200\,\mathrm{GeV}$ and $\sqrt{s_{NN}} = 17.3\,\mathrm{GeV}$ collision energy. 103

51 Pb+Pb(0-5%)/p+p and p+Pb/p+p nuclear modification factors at $y = 0$ in $\sqrt{s_{NN}} =$ 17.3 GeV collisions, with binary collision scaling. Similar data for $\sqrt{s_{NN}} = 200\,\mathrm{GeV}$ reactions are also shown. *: p+W/p+p data at $s_{NN} = 19.4\,\mathrm{GeV}$ from [20]. (Error-bars around unity indicate normalization errors.) 105

52 Pb+Pb(0-5%)/p+p and p+Pb/p+p nuclear modification factors at $y = 0$ in $\sqrt{s_{NN}} = 17.3\,\mathrm{GeV}$ collisions, with wounded nucleon scaling. Similar data for $\sqrt{s_{NN}} = 200\,\mathrm{GeV}$ reactions are also shown. *: p+W/p+p data at $s_{NN} = 19.4\,\mathrm{GeV}$ from [20]. (Errorbars around unity indicate normalization errors.) 106

53 Pb+Pb(0-5%)/p+Pb nuclear modification factors at $y = 0$ in $\sqrt{s_{NN}} = 17.3\,\mathrm{GeV}$ collisions. Similar data for $\sqrt{s_{NN}} = 200\,\mathrm{GeV}$ reactions are also shown. (Errorbars around unity indicate normalization errors.) 108

54 Pb+Pb(0-5%)/Pb+Pb(33.5-80%) nuclear modification factors at $y = 0$ in $\sqrt{s_{NN}} = 17.3\,\mathrm{GeV}$ collisions. Similar data for $\sqrt{s_{NN}} = 200\,\mathrm{GeV}$ reactions are also shown. pQCD: perturbative QCD calculation. (Errorbars around unity indicate normalization errors.) 110

55 The schematic of the used coordinate axis convention. 115

56 The mass spectrum of γ particles, reconstructed from e^+, e^- track pairs (upper panels), and of π^0 particles, reconstructed from $\gamma\gamma$ candidate pairs (lower panels), in p+Pb events. 121

57 A toy example for testing the iterative unfolding method, proposed in [41], for the $\pi^0 \to \gamma\gamma$ problem. The bottom panels show the performance of the $\pi^0 \to \gamma\gamma$ unfolding method proposed in [33] (R. Cahn). 123

List of Tables

1 The used datasets. 37

2 Conversion between VCAL energy (run 1468) and event centrality. 46

3 Available Pb+Pb statistics in the used centrality bins. 51

4 Available p+Pb and p+p statistics. 53

5 The list relevant feed-down channels. 81

6 Systematic error sources for Pb+Pb particle production spectra. 88

7 Average values and standard deviations of various collision parameters as a function of centrality in Pb+Pb collisions at $\sqrt{s_{NN}} = 17.3\,\mathrm{GeV}$. *: These values are semi-empiric averages, calculated on the full minimum-bias dataset, as discussed in the end of Section 3.1.2. 125

8 Average values of various collision parameters in p+Pb reactions at $\sqrt{s_{NN}} = 17.3\,\mathrm{GeV}$. *: These values are semi-empiric averages, calculated on the full dataset, as discussed in Section 3.2.2. 125

9 The table of $\pi^{\pm}$, $p, \bar{p}$, $K^{\pm}$ invariant yields at $y = 0$ for Pb+Pb(0-5%) – central – reactions at $\sqrt{s_{NN}} = 17.3\,\mathrm{GeV}$. 126

10 The table of $\pi^{\pm}$, $p, \bar{p}$, $K^{\pm}$ invariant yields at $y = 0$ for Pb+Pb(12.5-23.5%) – mid-central – reactions at $\sqrt{s_{NN}} = 17.3\,\mathrm{GeV}$. 127

11 The table of $\pi^{\pm}$, $p, \bar{p}$, $K^{\pm}$ invariant yields at $y = 0$ for Pb+Pb(33.5-80%) – peripheral – reactions at $\sqrt{s_{NN}} = 17.3\,\mathrm{GeV}$. 128

12 The table of $\pi^{\pm}$, $p, \bar{p}$, $K^{\pm}$ invariant yields at $y = 0$ for p+Pb reactions at $\sqrt{s_{NN}} = 17.3\,\mathrm{GeV}$. (Full dataset with varied centrality trigger setting, as discussed in Section 3.2.2.) 129

13 The table of $\pi^{\pm}$, $p, \bar{p}$, $K^{\pm}$ invariant yields at $y = 0$ for p+p reactions at $\sqrt{s_{NN}} = 17.3\,\mathrm{GeV}$. 130

Bibliography

[1] A. Adare *et al.* (the PHENIX Collaboration): *Transverse Momentum and Centrality Dependence of Dihadron Correlations in Au+Au Collisions at sqrt(s_NN)=200 GeV: Jet-quenching and the Response of Partonic Matter*; Preprint (2007) [arXiv:nucl-ex/0705.3238].

[2] S. S. Adler *et al.* (the PHENIX Collaboration): *Suppressed π^0 Production at Large Transverse Momentum in Central Au+Au Collisions at $\sqrt{s_{NN}} = 200$ GeV*; Phys. Rev. Lett. **91** (2003) 072301.

[3] S. S. Adler *et al.* (the PHENIX Collaboration): *Absence of Suppression in Particle Production at Large Transverse Momentum in sqrt(s_NN) = 200 GeV d+Au Collisions*; Phys. Rev. Lett. **91** (2003) 072303.

[4] S. S. Adler *et al.* (the PHENIX Collaboration): *Identified Charged Particle Spectra and Yields in Au+Au Collisions at sqrt(s_NN) = 200 GeV*; Phys. Rev. **C69** (2004) 034909.

[5] S. S. Adler *et al.* (the PHENIX Collaboration): *Centrality Dependence of Direct Photon Production in $\sqrt{s_{NN}} = 200\,\mathrm{GeV}$ Au+Au Collisions*; Phys. Rev. Lett. **94** (2005) 232301.

[6] S. S. Adler *et al.* (the PHENIX Collaboration): *Nuclear Effects on Hadron Production in d+Au and p+p Collisions at sqrt(s_NN)=200 GeV*; Phys. Rev. **C74** (2006) 024904.

[7] S. Afanasiev *et al.* (the NA49 Collaboration): *Energy Dependence of Pion and Kaon Production in Central Pb+Pb Collisions*; Phys. Rev. **C66** (2002) 054902.

[8] S. Afanasiev *et al.* (the NA49 Collaboration): *The NA49 Large Acceptance Hadron Detector*; Nucl. Instr. Meth. **A430** (1999) 210.

[9] M. M. Aggarwal *et al.* (the WA98 Collaboration): *Transverse mass distributions of neutral pions from ^{208}Pb-induced reactions at 158·A GeV*; Eur. Phys. J. **C23** (2002) 225.

[10] W. W. M. Allison, J. H. Cobb: *Relativistic Charged Particle Identification by Energy Loss*; Ann. Rev. Nucl. Sci. **30** (1980) 253.

[11] C. Alt *et al.* (the NA49 Collaboration): *Inclusive Production of Charged Pions in p+p Collisions at* 158 GeV/c *Beam Momentum*; Eur. Phys. J. **C45** (2006) 343.

[12] C. Alt *et al.* (the NA49 Collaboration): *Inclusive Production of Charged Pions in p+C Collisions at* 158 GeV/c$\cdot A$ *Beam Momentum*; Eur. Phys. J. **C49** (2007) 897.

[13] C. Alt, ..., A. László *et al.* (the NA49 Collaboration): *Bose-Einstein Correlations of Pion Pairs in Central Pb+Pb Collisions at CERN SPS Energies*; Phys. Rev. **C** (2007) submitted [arXiv:nucl-ex/0709.4507].

[14] C. Alt, ..., A. László *et al.* (the NA49 Collaboration): *Pion and Kaon Production in Central Pb+Pb Collisions at 20A and 30A GeV: Evidence for the Onset of Deconfinement*; Phys. Rev. **C** (2007) submitted [arXiv:nucl-ex/0710.0118].

[15] C. Alt, ..., A. László *et al.* (the NA49 Collaboration): *High Transverse Momentum Hadron Spectra at* $\sqrt{s_{NN}} = 17.3$ GeV, *in Pb+Pb and p+p Collisions*; Phys. Rev. **C77** (2008) 034906.

[16] T. Anticic *et al.* (the NA49 Collaboration): *Energy and Centrality Dependence of Deuteron and Proton Production in Pb+Pb Collisions at Relativistic Energies*; Phys. Rev. **C69** (2004) 024902.

[17] N. Antoniou, ..., A. László *et al.* (the NA61 Collaboration): *Study of Hadron Production in Collisions of Protons and Nuclei at the CERN SPS*; NA49-future Letter of Intent (2006), Sections 2.2 and 4.2 [CERN-SPSC-2006-001, SPSC-I-235].

[18] N. Antoniou, ..., A. László *et al.* (the NA61 Collaboration): *Study of Hadron Production Hadron-Nucleus and Nucleus-Nucleus Collisions at the CERN SPS*; NA49-future Proposal (2006), Sections 2.2, 3.5.2 and 4.2 [CERN-SPSC-2006-034, SPSC-P-330].

[19] N. Antoniou, ..., A. László *et al.* (the NA61 Collaboration): *Additional Information Requested in the Proposal Review Process*; Addendum to the NA49-future Proposal (2007), Section 8 [CERN-SPSC-2007-004, SPSC-P-330].

[20] D. Antreasyan *et al.*: *Production of Hadrons at Large Transverse Momentum in 200-, 300-, and 400-GeV p-p and p-nucleus Collisions*; Phys. Rev. **D19** (1979) 764.

[21] H. Appelshäuser *et al.* (the NA49 Collaboration): *Spectator Nucleons in Pb+Pb Collisions at 158 A·GeV*; Eur. Phys. J. **A2** (1998) 383.

[22] J. Bächler *et al.* (the NA49 Collaboration): *Hadron Production in Nuclear Collisions from the NA49 Experiment at* $158\,\mathrm{GeV/c} \cdot A$; Nucl. Phys. **A661** (1999) 45c.

[23] S. Baker, R. D. Cousins: *Clarification of the Use of Chi-square and Likelihood Functions in Fits to Histograms*; Nucl. Instr. Meth. **A221** (1984) 437.

[24] S. A. Bass *et al.*: *Microscopic Models for Ultra-relativistic Heavy Ion Collisions*; Progr. Part. Nucl. Phys. **41** (1998) 225.

[25] S. A. Bass, M. Gyulassy, H. Stocker, W. Greiner: *Signatures of Quark Gluon Plasma Formation in High-energy Heavy Ion Collisions: a Critical Review*; J. Phys. **G25** (1999) r1.

[26] I. G. Bearden *et al.* (the BRAHMS Collaboration): *Charged Meson Rapidity Distributions in Central Au+Au Collisions at sqrt(s_{NN}) = 200 GeV*; *Phys. Rev. Lett.* **94** (2005) 162301.

[27] A. Bialas, M. Bleszynski, W. Czyz: *Multiplicity Distributions in Nucleus-Nucleus Collisions at High Energies*; Nucl. Phys. **B111** (1976) 461.

[28] A. Bialas, W. Czyz: *Wounded Nucleon Model and Deuteron–Gold Collisions at RHIC*; Acta Phys. Polon. **B36** (2005) 905.

[29] H. Bichsel: *Particle Identification in TPC*; University of Washington, Seattle (1994).

[30] T. S. Bíró, P. Lévai, J. Zimányi: *ALCOR: a Dynamic Model for Hadronization*; Phys. Lett. **B472** (1995) 6.

[31] C. Blume (for the NA49 collaboration): *Centrality and Energy Dependence of Proton, Light Fragment and Hyperon Production*; J. Phys. **G34** (2007) s951.

[32] C. Bovet *et al.*: *The CEDAR Counters for Particle Identification in the SPS Secondary Beams: a Description and an Operation Manual*; CERN Yellow Report (1982) 81-13.

[33] R. N. Cahn: *Inclusive Photon Distributions: Contributions from π^0's and Bremsstrahlung*; Phys. Rev. **D7** (1973) 247.

[34] Compilation on particle production parameters, measured at CERN-NA49 [http://na49info.web.cern.ch/na49info/na49/Archives/Data/NA49NumericalResults].

[35] G. E. Cooper: *Baryon Stopping and Hadronic Spectra at 158GeV/nucleon*; Ph.D. dissertation (2000).

[36] Z. Fodor, S. D. Katz: *Lattice Determination of the Critical Point of QCD at Finite T and Mu*; J. High Energy Phys. **0203** (2002) 014.

[37] M. Jacob, M. Slansky: *Nova Model of Inclusive Reactions*; Phys. Rev. **D5** (1972) 1847.

[38] A. László: *Building Calorimetric Detectors for CERN experiments*; Diploma Thesis (2004).

[39] A. László: *Time-dependence Calibration of the Veto Calorimeter*; NA49 Technical Note[30] (2006).

[40] A. László *et al.* (the NA49 Collaboration): *High p(T) Spectra of Identified Particles Produced in Pb Plus Pb Collisions at 158 GeV/nucleon Beam Energy*; Nucl. Phys. **A774** (2006) 473.

[41] A. László: *A Robust Iterative Unfolding Method for Signal Processing*; J. Phys. **A39** (2006) 13621.

[42] A. László: *Deconvolution of noisy data*; Talk given at the Zimányi Winter School (2006), RMKI, Budapest [http://www.rmki.kfki.hu/~laszloa/downloads/zws06.pdf].

[43] A. László: *Calculating Mean Values of Collision Parameters as a Function of Centrality*; NA49 Technical Note (2007).

[44] A. László: *High Transverse Momentum Identified Charged Particle Yields in* 158 GeV/*nucleon Pb+Pb Collisions*; NA49 Technical Note (2007).

[45] A. László *et al.* (the NA49 Collaboration): *New Results and Perspectives on* R_{AA} *Measurements Below* 20 GeV *CM-energy at Fixed Target Machines*; Int. J. Mod. Phys. **E16** (2007) 2516.

[30] The NA49 Technical Notes are stored in the EDMS repository system: [https://edms.cern.ch/cedar/plsql/cedarw.home?project=NA49].

[46] A. László (for the NA61 Collaboration): *NA61/SHINE at the CERN SPS*; Invited talk at Critical Point and Onset of Deconfinement (Darmstadt, 2007); Porceedings of Science **CPOD07** (2007) 054.

[47] D. Kharzeev: *Can Gluons Trace Baryon Number?*; Phys. lett. **B378** (1996) 238.

[48] C. de Marzo *et al.*: *A Segmented Photon - Hadron Calorimeter Using a Two Colored Wavelength Shifter Optical Readout System*; Nucl. Instr. Meth. **217** (1983) 405.

[49] W H. Press, B. P. Flannery, S. A. Teukolsky, W. T. Vetterling: *Numerical Recipes in C: the Art of Scientific Computing*; Cambridge University Press (1992).

[50] F. Retiere, M. A. Lisa: *Observable Implications of Geometrical and Dynamical Aspects of Freeze-out in Heavy Ion Collisions*; Phys. Rev. **C70** (2004) 044907.

[51] A. Rybicki: *Study of Particle Yields Using dE/dx Fits*; NA49 Technical Note (1999).

[52] M. Rybczynski: *Non-uniformity of the Veto Calorimeter*; NA49 Technical Note (2005).

[53] M. Rybczynski: *Interactions of the Projectile Spectators with the Material of the Detector*; NA49 Technical Note (2005).

[54] T. Schuster, A. László *et al.* (the NA49 Collaboration): *High p(T) Spectra of Identified Particles Produced in Pb+Pb Collisions at 158 A GeV Beam Energy*; J. Phys. **G32** (2006) s479.

[55] F. Siklér: *Slow Particles from Hadron-Nucleus Collisions at the CERN-NA49 Experiment*; NA49 Technical Note (2004).

[56] F. Siklér: *Centrality Control of Hadron Nucleus Interactions by Detection of Slow Nucleons*; Preprint (2003) [arXiv:hep-ph/0304065].

[57] M. Szuba: *Azimuthal Correlations at High p_T*; Talk given at the NA49 Collaboration Meeting (November 2007);
Two-particle Azimuthal Correlations of High-p_T Charged Hadrons at the CERN SPS; Parallel talk submitted to Quark Matter 2008.

[58] D. Varga: *Study of Inclusive and Correlated Particle Production in Elementary Hadronic Interactions*; Ph.D. dissertation (2003).

[59] G. I. Veres: *Baryon Momentum Transfer in Hadronic and Nuclear Collisions at the CERN NA49 Experiment*; Ph.D. dissertation (2001).

[60] G. I. Veres: *New Developments in Understanding and Correction of dE/dx*; NA49 Technical Note (2000).

[61] S. A. Voloshin: *Azimuthal and Rapidity Correlations of High p_t Particles in Pb+Pb Collisions at CERN SPS*; NA49 Technical Note (1999).

[62] X.-N. Wang, M. Gyulassy: *HIJING: a Monte-Carlo Model for Multiple Jet Production in p p, p A and A A Collisions*; Phys. Rev. **D44** (1991) 3501.

[63] X.-N. Wang: *High-p_T Hadron Spectra, Azimuthal Anisotropy and Back-to-Back Correlations in High-energy Heavy-ion Collisions*; Phys. Lett. **B595** (2004) 165.

[64] X.-N. Wang: Private communication on particle spectrum predictions in $\sqrt{s_{NN}} = 17.3\,\mathrm{GeV}$ Pb+Pb collisions, as a result of the perturbative QCD based calculations in [63].

[65] K. Werner: *Strings, Pomerons, and the VENUS Model of Hadronic Interactions at Ultrarelativistic Energies*; Phys. Rept. **232** (1993) 87.

Summary

In the dissertation, the *experimental* methods and results are discussed, concerning the evolution of the single particle spectra at high transverse momentum, when going from proton-proton through proton-nucleus to nucleus-nucleus collisions, at 17.3 GeV nucleon-nucleon collision energy. The presented results are based on the p+p, p+Pb and Pb+Pb data of the CERN-NA49 fixed target experiment at 158 GeV/c beam momentum per nucleon.

The production of the high transverse momentum particles is well characterized by their yields in nucleus-nucleus collisions, relative to elementary reactions scaled up on a geometrical basis (e.g. scaled p+p), which is called nuclear modification. The results of the experiments at the RHIC accelerator at Brookhaven show, that this modification at 200 GeV nucleon-nucleon collision energy is a suppression, which may be a signature of the quark-gluon plasma formation. To look for a possible phase transition using this effect, the energy dependence of the amount of suppression has to be studied. As presently only the NA49 experiment recorded appropriate data for this study at about a factor of 10 lower collision energy than at RHIC, the analysis of the existing NA49 data from this aspect is of natural choice.

A brief description of the setup and operation of the NA49 detector is given. An overview of the data reduction procedure is also presented. The main parts of the dissertation cover the details of the analysis procedures, which mostly concerns calibration, cut, and correction methods, many of which were developed by the *author*.

The results may be grouped into the following description.

- The fully corrected single particle transverse momentum spectra of $\pi^{\pm}$, $p, \bar{p}$, $K^{\pm}$ around midrapidity were obtained for p+p, p+Pb and Pb+Pb collisions, at 17.3 GeV nucleon-nucleon collision energy. The covered transverse momentum region extends to about 4.5 GeV/c.

- As an result of the π^0 analysis surveys, a robust iterative unfolding method, for general applications in signal processing, was developed. Examples for the performance of this method are given.

- By comparing to the published 200 GeV RHIC results, a complete energy scan of various quantities, derived from single particle spectra, are shown. The net-baryon/meson ratios show a factorization in energy and transverse momentum. They are well reproduced by the blast-wave model description. The derived nuclear modification factors show that the energy dependence of the high transverse momentum particle suppression is surprisingly small, although the amount of suppression is less than at 200 GeV for $\pi^{\pm}$. The data do not show a sudden disappearance of suppression with decreasing collision energy.

Összefoglaló

A dolgozat azon *kísérleti* módszereket és eredményeket tárgyalja, amelyek az egyrészecske-spektrumok nagy transzverz impulzusoknál való fejlődésével kapcsolatosak, ahogy egyre bonyolultabb rendszereket vizsgálunk kezdve az elemi proton-proton, majd proton-mag, illetve mag-mag ütközéseket tekintve, $17.3\,\mathrm{GeV}$ nukleon-nukleon ütközési energián. A bemutatott eredmények a fix-céltárgyas CERN-NA49 kísérlet $158\,\mathrm{GeV/c}$ nukleononkénti nyaláb impulzusnál felvett p+p, p+Pb és Pb+Pb adatain alapulnak.

A nagy transzverz impulzusú részecskék hozamát jól jellemzi, hogy miképpen alakul mag-mag ütközésekben, geometriai alapon felskálázott elemibb reakciókhoz (pl skálázott p+p) képest, melyet nukleáris modifikációnak nevezünk. A brookhaveni RHIC gyorsító eredményei azt mutatják, hogy $200\,\mathrm{GeV}$ nukleonpáronkénti ütközési energián, a modifikáció egy elnyomásként jelentkezik nagy transzverz impulzusnál, ami a kvark-gluon plazma kialakulásának egyik jelzője lehet. Ha e jelenség segítségével fázisátmenetet szeretnénk feltérképezni, akkor az elnyomódás mértékének energiafüggését kell meghatároznunk. Jelenleg egyedül az NA49 kísérlet rendelkezik a célnak megfelelő adatsorral, melyet kb 10-szer alacsonyabb ütközési energián rögzített. Ezért az NA49 adatok ilyen aspektusból való tanulmányozása természetes módon kínálja magát.

A dolgozat az NA49 kísérlet felépítésének, működésének és adatredukciós módszereinek áttekintése után részletesen tárgyalja a fizikai analízis kalibrációs, vágási, illetve korrekciós eljárásait, melyeket döntő részben a *szerző* dolgozott ki.

A dolgozat eredményei a következő pontokban foglalhatók össze.

- Meghatároztam a teljesen korrigált $\pi^{\pm}$, $p, \bar{p}$, $K^{\pm}$ egyrészecske transzverz impulzus spektrumokat nulla rapiditás körül, p+p, p+Pb és Pb+Pb ütközésekben, $17.3\,\mathrm{GeV}$ nukleon-nukleon ütközési energián. A lefedett transzverz impulzus tartomány kiterjed egészen $4.5\,\mathrm{GeV/c}$-ig.

- A π^0 részecskehozam vizsgálata során kifejlesztésre került egy a jelfeldolgozásban általánosan alkalmazható iteratív spektrum-visszafejtési módszer. Hatékonysága bemutatásra kerül.

- A $200\,\mathrm{GeV}$-es RHIC eredményekkel végzett összehasonlítás egy teljes energiafüggési képet nyújt a spektrumokból nyerhető mennyiségekre vonatkozóan. A nettó-barion/mezon arányok egy energia - transzverz impulzus faktorizációt mutatnak. Ezen arányokat a lökéshullám-leírás jól visszaadja. A spektrumokból nyert nukleáris modifikációs faktorok meglepő módon nem mutatnak erős energiafüggést, bár a $\pi^{\pm}$ elnyomás mértéke határozottan kisebb a $200\,\mathrm{GeV}$ energián mértnél. Az adatok azonban nem utalnak a nagy transzverz impulzusú részecskeelnyomás csökkenő ütközési energiával való hirtelen megszűnésére.